University of Pennsylvania
ScholarlyCommons

Publicly Accessible Penn Dissertations

2016

First-Principles Studies Of Solar Cell Materials: Absorption, Carrier Lifetime And Non-Linear Optical Effect

Fan Zheng
University of Pennsylvania, zhengfan@sas.upenn.edu

Follow this and additional works at: https://repository.upenn.edu/edissertations

 Part of the Chemistry Commons, Mechanics of Materials Commons, and the Physics Commons

Recommended Citation
Zheng, Fan, "First-Principles Studies Of Solar Cell Materials: Absorption, Carrier Lifetime And Non-Linear Optical Effect" (2016). *Publicly Accessible Penn Dissertations*. 2668.
https://repository.upenn.edu/edissertations/2668

This paper is posted at ScholarlyCommons. https://repository.upenn.edu/edissertations/2668
For more information, please contact repository@pobox.upenn.edu.

First-Principles Studies Of Solar Cell Materials: Absorption, Carrier Lifetime And Non-Linear Optical Effect

Abstract
The next generation solar cell materials have attracted tremendous research to improve their performance. In these materials, chalcogenides materials, inorganic perovskite and newly developed organometal halide perovskite have demonstrated their potential usage as solar cells owing to their exceptional properties to absorb the light and transform the light energy to current. Hence, understanding and improving these properties can promote further material design strategies for higher performance but lower the cost. Density functional theory is a widely used accurate calculation method to compute various physical properties of a material in an efficient way. In this thesis, we mainly use the density functional theory method to explore the light-matter interaction and its effect to the material's application as a solar cell. Alkali-metal chalcogenides have been found to exhibit appropriate band gaps for solar cells. We find that the volume compression can substantially enhance the optical dielectric function and the absorption coefficient intrinsically. The density function calculation and the tight-binding model show that this structure-property relation is mainly owing to the wavefunction phase change by compression, where the one-dimensional atomic chains play a significant role to relate the optical absorption and the structural change. But the high absorption does not guarantee high power conversion efficiency. This is because the excited carrier need to diffuse to the electrodes before they recombine. Organometal halide perovskites are found to have very large diffusion length and the long carrier lifetime. But the mechanism for such phenomena is still unknown. Here, by studying the structural change to the band structure and spin using CH3NH3PbI3 as an example, we find that the strong Rashba effect contributes to the long carrier lifetime by creating spin-forbidden electronic transitions, which slows down the radiative recombination and enhance the carrier lifetime. Furthermore, to study the spatial disorder effect to the electronic structure, we develop a large-scale tight-binding model which can highlight the structural disorder but still compute the band structure efficiency for very large systems. We find that the spatial disorder can create localized changes. These charge localization are spatially separated for valence band minimum and conduction band maximum. Therefore, their recombination will be further slowed down due to such spatial separation. In addition to these solar cell mechanism, we also studied the non-linear optical effect (bulk photovoltaic effect) in inorganic semiconductors. In this thesis, I use the example of CH3NH3PbI3 to illustrate its bulk photovoltaic effect responses. It is found that this material can generate more than three times large photo-current than the prototypical material BiFeO3, although its polarization is only less than one tenth of BiFeO3. We think this is due to its delocalized electronic structure of the band edges. The effect of Cl to the bulk photovoltaic response is also studied, we find that the apical substitution of I to Cl can enhance the response owing to the larger polarization. The bulk photovoltaic response of other materials such as LiAsSe2, BiFeO3 are compared, and we generalize the strategies to design new materials with better performance.

Degree Type
Dissertation

Degree Name
Doctor of Philosophy (PhD)

This dissertation is available at ScholarlyCommons: https://repository.upenn.edu/edissertations/2668

Graduate Group
Chemistry

First Advisor
Andrew M. Rappe

Subject Categories
Chemistry | Mechanics of Materials | Physics

This dissertation is available at ScholarlyCommons: https://repository.upenn.edu/edissertations/2668

FIRST-PRINCIPLES STUDIES OF SOLAR CELL MATERIALS: ABSORPTION, CARRIER LIFETIME AND NON-LINEAR OPTICAL EFFECT

Fan Zheng

A DISSERTATION

in

Chemistry

Presented to the Faculties of the University of Pennsylvania in Partial Fulfillment of the Requirements for the Degree of Doctor of Philosophy

2016

Supervisor of Dissertation	Graduate Group Chairperson
Andrew M. Rappe	Gary A. Molander
Professor of Chemistry and Materials Science and Engineering	Hirschmann-Makineni Professor of Chemistry

Dissertation Committee

Joseph E. Subotnik	Professor of Chemistry
Eugene Mele	Professor of Physics
Marsha I. Lester	Edmund J. Kahn Distinguished Professor

To my mother and my father,

for their love

Acknowledgements

First, I would like to thank my advisor and my mentor, Andrew M. Rappe. With the help of the numerous insightful discussions with him, I learn to solve scientific problem, lead the research and collaborate with other people. During these six years, Andrew taught me science, and the way to perform science research with high standard. In addition to knowledge, Andrew show me how to collaborate with other people and how to mentor people. I think his kindness and enthusiasm shape me as a scientist and a person.

I would also like to thank my committee members: Prof. Joseph E. Subotnik, Prof. Eugene Mele and Prof. Marsha I. Lester. I also want to express my deep gratitude to Prof. Robin Hochstrasser. The insightful and patient discussion, and their challenging questions always drive me to move forward.

I would like to thank all my collaborators for the stimulating discussions and the patience working with me: Prof. Junlin Wang, Prof. Louis Brus, Prof. John Perdew, Prof. Ilya Grinberg, Prof. Shijing Gong, Dr. Jianmin Tao, Dr. Steve Young, Dr. Shi Liu, Dr. Fenggong Wang, Dr. Liang Z. Tan, Dr. Hiroyuki Takenaka, Dr. Youngkuk Kim, Dr. John Brehm, Dr. Diomedes Saldana Greco, Dr. Lu You, Dr. Omer Yaffe, Dr. Yinsheng Guo, Nathan Koocher, Radhe Agarwal, Ziyu Ye, and Saif Ullah.

I want to have the special thanks to Rappe group members. I really enjoy the time in this group. I want to thank Dr. Gaoyang Gou, Dr. Lai Jiang, Dr. Miguel Angel Mendez Polanco, Dr. Seungchul Kim, Dr. Chan-woo Lee, Dr. Julian Gebhardt, Yubo Qi, Jing Yang,

Tian Qiu, Rob Wexler. Particularly, I want to thank Dr. Steve Young for his patience of teaching me Linux and running my first calculation.

Finally, I want to thank my family. No need to say too much for this.

ABSTRACT

FIRST-PRINCIPLES STUDIES OF SOLAR CELL MATERIALS: ABSORPTION, CARRIER LIFETIME AND NON-LINEAR OPTICAL EFFECT

Fan Zheng

Andrew M. Rappe

The next generation solar cell materials have attracted tremendous research to improve their performance. In these materials, chalcogenides materials, inorganic perovskite and newly developed organometal halide perovskite have demonstrated their potential usage as solar cells owing to their exceptional properties to absorb the light and transform the light energy to current. Hence, understanding and improving these properties can promote further material design strategies for higher performance but lower the cost. Density functional theory is a widely used accurate calculation method to compute various physical properties of a material in an efficient way. In this thesis, we mainly use the density functional theory method to explore the light-matter interaction and its effect to the material's application as a solar cell. Alkali-metal chalcogenides have been found to exhibit appropriate band gaps for solar cells. We find that the volume compression can substantially enhance the optical dielectric function and the absorption coefficient intrinsically. The density function calculation and the tight-binding model show that this structure-property relation is mainly owing to the wavefunction phase change by compression, where the one-dimensional atomic chains play a significant role to relate the optical absorption and the structural change. But the high absorption does not guarantee high power conversion efficiency. This is because the excited carrier need to diffuse to the electrodes before they recombine. Organometal halide perovskites are found to have very large diffusion length and the long carrier lifetime. But the mechanism for such phenomena is still unknown. Here, by studying the structural change to the band structure and spin using $CH_3NH_3PbI_3$ as an example, we find that the strong

Rashba effect contributes to the long carrier lifetime by creating spin-forbidden electronic transitions, which slows down the radiative recombination and enhance the carrier lifetime. Furthermore, to study the spatial disorder effect to the electronic structure, we develop a large-scale tight-binding model which can highlight the structural disorder but still compute the band structure efficiency for very large systems. We find that the spatial disorder can create localized changes. These charge localization are spatially separated for valence band minimum and conduction band maximum. Therefore, their recombination will be further slowed down due to such spatial separation. In addition to these solar cell mechanism, we also studied the non-linear optical effect (bulk photovoltaic effect) in inorganic semiconductors. In this thesis, I use the example of $CH_3NH_3PbI_3$ to illustrate its bulk photovoltaic effect responses. It is found that this material can generate more than three times large photo-current than the prototypical material $BiFeO_3$, although its polarization is only less than one tenth of $BiFeO_3$. We think this is due to its delocalized electronic structure of the band edges. The effect of Cl to the bulk photovoltaic response is also studied, we find that the apical substitution of I to Cl can enhance the response owing to the larger polarization. The bulk photovoltaic response of other materials such as $LiAsSe_2$, $BiFeO_3$ are compared, and we generalize the strategies to design new materials with better performance.

Contents

List of Tables

List of Figures

Chapter 1

Introduction

Solar energy is an alternative energy sources in addition to the fossil fuels. It is limitless, clean, safe, renewable and generates less CO_2. Photovoltaic (PV) effect, by converting the sunlight to the electricity, is one of the most important ways of solar energy application. From the time when people first observed the PV effect in the conductive solution in 1839 to current that more than 5×10^7 square meter PV solar panels are built to generate up to 8379 MWatt in United States [7], the ability to synthesize high efficiency solar cell has grow rapidly. With the more advanced techniques used in the solar cell industry, the price of the solar cell has dropped significantly. In 1977 after the invention of the PV solar cell, the price is as high as $76.67/Watt. However, this price has dropped to $0.74/Watt in 2013 owing to the massive production and usage [8]. Although the PV solar cell is increasingly important and rapidly expanding over the conventional energy generation ways, the total electricity from the PV solar cell is still limited to 0.6% in 2015, which is far less than other energy generations such as natural gas (29%), oil (36.2%) and coal (16.1%) [7]. Even compared to other renewable energy sources as wind (1.9%) and hydroelectric (2.4%), the PV solar cell application is relatively low. The solar cell energy technique is still new. Hence, understanding the PV effect and designing the new materials with cheaper price but high frequency, are needed to advance the PV solar technique.

There are many factors to describe the performance of the PV solar cells. Shown in Fig. 1.1 is a typical measured I-V curve. As denoted in the Figure, the most important parameters are short-circuit current ($I_{\rm sc}$), open-circuit voltage ($V_{\rm oc}$), filling parameter (FF). Finally, the resulting power conversion efficiency (PCE) will be expressed as PCE = $I_{\rm sc}V_{\rm oc}FF/P_{\rm in}$ with $P_{\rm in}$ as the incoming light power.

The most most common commercial solar cell is the silicon p-n junction type solar cell invented in 1954. In this system, the different doped p- or n-type silicon semiconductors will form an internal electric field built across the interface owing to the uneven distributed electron (and holes) when the two materials are attached. This internal electric

field can further promote the excited electron and hole separation after their generating by the light. These separated carriers (electrons and holes) can diffuse to the electrodes, and then flow to the load to make power. However, this type of PV solar cell suffers from the Shockley–Queisser limit, which is 34% for ideal p-n junction solar cell due to the carrier recombination, sunlight spectrum losses, *et al*. Furthermore, the band gap of this solar cell is limited by the band gap the silicon, i.e. it can only increase to around 1.3 eV, which further limits its usage. Therefore, we want to explore and design new materials for the potential solar cell applications.

There are several aspects that are important to design new materials for the solar cell:

- *Appropriate band gap.* The energies of the sunlight is not evenly distributed for all the frequencies. The frequency range with the most concentrated energy is mainly in the visible light range from 400 nm to 750 nm, corresponding 1.1 ∼3.1 eV. This requires the band gap of the material for the light absorption should be at least less than 3 eV. Lower band gap materials can further maximize its power conversion ability. People have done tremendous work to reduce the band gap such as doping and solid solution [9, 10, 11, 12, 13, 14, 15, 16]. Furthermore, structure change such as transforming from rhombohedral to tetragonal reduces the band gap of the perovskites. [17] Introducing domain and domain wall can also decrease the band gap and make it applicable to the solar cells [18].

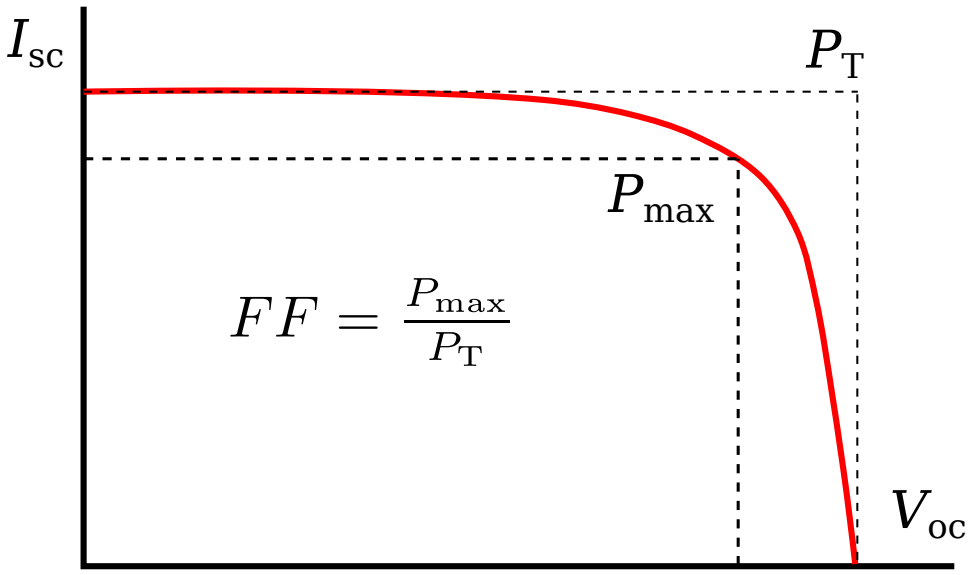

Figure 1.1: A typical I-V curve for the working solar cell.

- *High absorption.* Absorption spectrum describes how much light can be absorbed under the illumination, i.e. how much light can be used to excited electrons and holes. The materials with very high absorption are expected owing to their potential abilities to convert more sunlight. Many semiconductors such as InP, GaAs, GaP, CdS, CdSe, ZnSe *et al.* Shown in Fig. 1.2 is the absorption spectrum for some of the solar cell semiconductors, displaying relatively high absorption coefficient. Many work has been done to enhance the absorption of the material, from internal or external aspects. The most commonly used is the surface plasmon induced by metallic nanoparticles to increase the optical absorption in semiconductors [19, 20, 21, 22, 23].

- *Long diffusion length.* When the excited carriers (electrons and holes) are separated, they diffuse to the boundary of the sample to transform into the electrode. It is quite possible that these carriers can recombine and emit photons. In more complicated situations, the recombination will not generate photons, instead, the non-radiative recombination will happen, transforming the energy of the light to heat. Thus, raising the carrier diffusion length is significant to increase the PCE. The diffusion length is related to the product of the carrier lifetime and the mobility. The former is proportional to its effective mass (relevant to the band dispersion), which is the property of the material itself. The latter (i.e. carrier lifetime) is related to many aspects. But defects and electron-phonon coupling are generally the most relevant factors. High defect density and strong electron-phonon coupling will significantly reduce the carrier lifetime. In addition, in materials with indirect band gap, the conduction band minimum (CBM) and valence band maximum (VBM) are not located at the same $\mathbf{k}$ point, and their recombination will be forbidden in principle unless with the help of the phonons. Therefore, materials with indirect band gap tend to have long carrier lifetime, such as silicon.

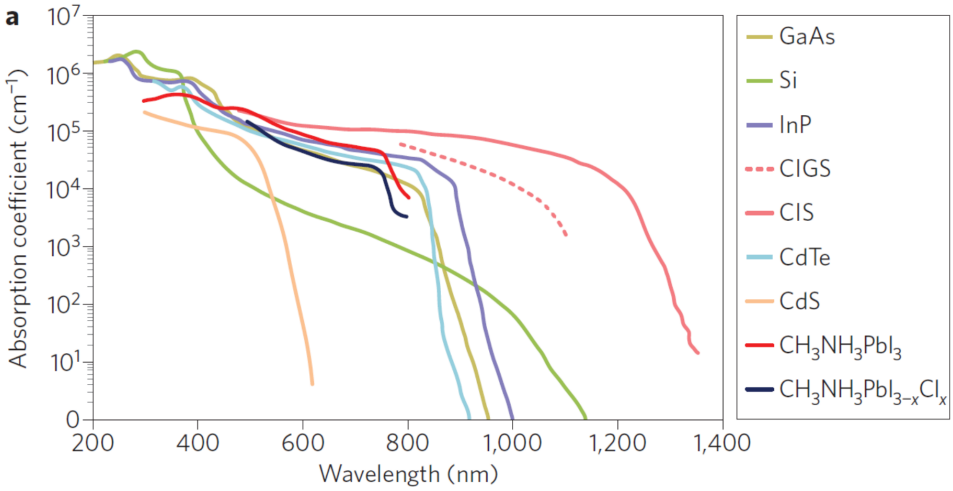

Figure 1.2: The absorption spectrum of various semiconductors.(reproduced from Ref. [4])

Density functional theory (DFT) demonstrates to be an efficient yet accurate way to compute physical properties of the materials. With the recent development of the accurate functionals, DFT has become a standard method to compute the materials' geometric and electronic structures. Although this method is a ground state theory, we can still use DFT to describe excited-state related properties. In this thesis, I will discuss the first-principles calculations for the potential solar cell materials. This thesis will emphasize: i) use first-principles method (mainly DFT) to understand physical properties of the materials, ii) use first-principles method to explain the experimental observed phenomena, iii) use first-principles method to design new materials for the solar cell applications.

With the above mentioned focuses, in Chapter 3, based on first-principles calculations, we predict a substantial increase in the optical dielectric function of $LiAsSe_2$ under pressure. We find that the optical dielectric constant is enhanced threefold under compression along all three axes by 3%. This enhancement is mainly due to the dimerization strength reduction of the one-dimensional (1D) As–Se chains in $LiAsSe_2$, which significantly alters the wavefunction phase mismatch between two neighboring chains and changes the transition intensity. By developing a tight-binding model of the interacting 1D chains, the essential features of the low-energy electronic structure of $LiAsSe_2$ are captured. Our findings are important for understanding the fundamental physics of $LiAsSe_2$ and provide a feasible way to enhance the material optical response that can be applied to light harvesting for energy applications.

In Chapter 4, we move to another type of materials called organometal halide perovskite. Organometal halide perovskites are promising solar-cell materials for next-generation photovoltaic applications. The long carrier lifetime and diffusion length of these materials make them very attractive for use in light absorbers and carrier transporters. While these aspects of organometal halide perovskites have attracted the most attention, the consequences of the Rashba effect, driven by strong spin-orbit coupling, on the photovoltaic properties

of these materials are largely unexplored. In this work, taking the electronic structure of $CH_3NH_3PbI_3$ (methylammonium lead iodide) as an example, we propose an intrinsic mechanism for enhanced carrier lifetime in 3D Rashba materials. Based on first-principles calculations and a Rashba spin-orbit model, we demonstrate that the recombination rate is reduced due to the spin-forbidden transition. These results are important for understanding the fundamental physics of organometal halide perovskites and for optimizing and designing the materials with better performance. The proposed mechanism including spin degrees of freedom offers a new paradigm of using 3D Rashba materials for photovoltaic applications. Furthermore, with our recently developed new method to solve large-scale tight-binding Hamiltonian, we find that the conduction band minimum and valence band maximum of the trajectory from the classical molecular dynamics simulation are spatially separated, which creates slower recombination compared to the high symmetric structure. This mechanism could also contribute to the long carrier lifetime.

In Chapter 5, we compute the shift current, a dominant mechanism of bulk photovoltaic effect (BPVE) for ferroelectric photovoltaics, in $CH_3NH_3PbI_3$ and $CH_3NH_3PbI_{3-x}Cl_x$ from first principles. We find that these materials give approximately three times larger shift current PV response to near-IR and visible light than the prototypical ferroelectric photovoltaic $BiFeO_3$. The molecular orientations of $CH_3NH_3^+$ can strongly affect the corresponding PbI_3 inorganic frame so as to alter the magnitude of the shift current response. Specifically, configurations with dipole moments aligned in parallel distort the inorganic PbI_3 frame more significantly than configurations with near net zero dipole, yielding a larger shift current response. Furthermore, we explore the effect of Cl substitution on shift current, and find that Cl substitution at the equatorial site induces a larger response than does substitution at the apical site. In addition, we review the bulk photovoltaic effect in $BiFeO_3$ and $LiAsSe_2$ and make comparisons. Based on the comparison, we find that the delocalied orbital character can enhance the shift current. With this, we propose three types of materials which

may have large shift current and BPVE.

In Chapter 6, the whole thesis is summarized with future directions.

Chapter 2

Methods

2.1 Density Functional Theory

Hamiltonian. The Hamiltonian of the system can be represented as [24]:

$$\begin{aligned} H_{\text{tot}} &= H_{\text{nulkin}} + H_{\text{elekin}} + H_{\text{nul-ele}} + H_{\text{ele-ele}} + H_{\text{nul-nul}} \\ &= \sum_i \frac{\mathbf{p}_i^2}{2m} + \sum_I \frac{\mathbf{P}_I^2}{2M_I} - \sum_I \sum_i \frac{z_I e^2}{|\mathbf{r}_i - \mathbf{R}_I|} + \frac{1}{2} \sum_{i \neq j} \frac{e^2}{|\mathbf{r}_i - \mathbf{r}_j|} + \frac{1}{2} \sum_{I \neq J} \frac{z_I z_J e^2}{|\mathbf{R}_i - \mathbf{R}_j|} \end{aligned}$$

This Hamiltonian describes the kinetic energy of electrons, kinetic energy of ions, electron-nucleus interaction, electron-electron and nucleus-nucleus interactions, respectively, where i,j, $\mathbf{p}$, and $\mathbf{r}$ are for electrons, and I,J, $\mathbf{P}$, and $\mathbf{R}$ are for nucleus. With the Born-Oppenheimer approximation, the Hamiltonian can be further split into electronic part H_e and the nucleus part H_N. For example, the electronic part can be expressed as:

$$H_e = H_{\text{elekin}} + H_{\text{nul-ele}} + H_{\text{ele-ele}}$$

Density function theory (DFT) is designed to solve the electronic Schrodinger equation efficiently yet accurately.

The idea of the DFT is that for a system with N electrons, without writing the wavefunction with 3N degree of freedom such as $\phi(\mathbf{r}_1, \mathbf{r}_2, ..., \mathbf{r}_N)$, the ground state charge density $n(\mathbf{r})$ is used as the most basic quantity throughout this theory. This charge density is unique for the ground state, hence, the process of solving the ground state is to minimize the total energy of the Hamiltonian by varying the charge density.

Kohn-Sham equaton. By choosing the orthonormal orbitals as the basis, the charge density can be decomposed into $n(\mathbf{r}) = \sum_i \phi_i^*(\mathbf{r})\phi_i(\mathbf{r})$. $H_{\text{ele-ele}}$ as the Hartree (or Coulomb) energy can be expressed as:

$$H_{\text{Hartree}} = E_{\text{H}}[n] = \frac{1}{2}\int n(\mathbf{r})\frac{e^2}{|\mathbf{r}-\mathbf{r}'|}n(\mathbf{r}')d\mathbf{r}d\mathbf{r}'$$

and the kinetic energy of a system of non-interacting electrons with the same density can be represented as:

$$H_{\text{ele,non-inter}} = T_0[n] = \sum_i \langle\phi_i(\mathbf{r}| - \frac{\hbar^2\nabla^2}{2m}|\phi_i(\mathbf{r}\rangle$$

Thus, the total energy (electronic part) will be:

$$E[n; v_{\text{ext}}] = T_0[n] + E_{\text{H}}[n] + \int v_{\text{ext}}(\mathbf{r})n(\mathbf{r})d\mathbf{r} + E_{\text{xc}}[n]$$

where $v_{\text{ext}}(\mathbf{r})$ is the external potential acting to the electrons from the nucleus. The exchange-correlation (EX) functional ($E_{\text{xc}}[n]$) is defined as:

$$E_{\text{xc}}[n] = T[n] - T_0[n] + E_{ee}[n] - E_{\text{H}}[n]$$

which is to describe the general difference between non-interacting electron gas and the real system. There is no exact form for the EX functionals. Different kinds of EX functionals have been proposed [25]. The bottom of this ladder is the local density approximation (LDA) with only local density used for the functional, and the generalized gradient approximation (GGA) with the local density and the density gradient ingredients. Although they are simple, they actually provide accurate results for many materials, which may be

owing to the error cancellation. Above this level is called meta-GGA functional, where the density Laplacian is introduce, greatly improving the atomization energy for molecules and surface energy for solids [26]. More accurate functional is to include the exact exchange (exchange term from Hartree-Fock), which gives very accurate prediction, but it is also expensive. With the expression for the Hartree energy and the specific form of the EX functional, the variation of the density can be solve analytically ($V = \delta E/\delta n(\mathbf{r})$). The Kohn-Sham equation can be solved as:

$$\left[-\frac{\hbar^2\nabla^2}{2m} + v_{\text{ext}}(\mathbf{r}) + V_{\text{coul}}(\mathbf{r}) + V_{\text{XC}}(\mathbf{r})\right]\phi_i(\mathbf{r}) = \epsilon_i\phi_i(\mathbf{r})$$

where $V_{\text{coul}}(\mathbf{r})$ and $V_{\text{XC}}(\mathbf{r})$ are functional derivatives of Hartree and EX energy, respectively. By diagonalizing the Hamiltonian, the Kohn-Sham orbital energy (ϵ_i) and eigenvector (ϕ_i) can be solved. The total energy calculated from DFT is not the sum of Kohn-Sham orbital energies, instead, it is expressed as:

$$E_{\text{Tot}} = \sum_i \epsilon_i - E_{\text{H}}[n] + E_{\text{XC}}[n] - \int V_{\text{XC}}(\mathbf{r})n(\mathbf{r})d\mathbf{r}$$

2.2 Linear Response and Density Functional Perturbation

Linear response in Kohn-Sham equation. With the perturbation of the external potential (δV_0), the density ($n(\mathbf{r})$ responses to such potential change as: $\delta n(\mathbf{r}) = \int \chi(\mathbf{r}, \mathbf{r}')\delta V_0(\mathbf{r}')d\mathbf{r}'$. χ is the density response to the potential perturbation (polarizability) [27]. Thus, the total potential change (with the screening of the charge density change) is:

$$\begin{aligned}\delta V(\mathbf{r}) &= \delta V_0(\mathbf{r}) + e^2 \int \frac{\delta n(\mathbf{r}')}{|\mathbf{r}-\mathbf{r}'|} d\mathbf{r}' \\ &= \int \left(\delta(\mathbf{r}-\mathbf{r}') + e^2 \int \frac{\chi(\mathbf{r}'',\mathbf{r}')}{|\mathbf{r}-\mathbf{r}'|} \right) \delta V_0(\mathbf{r}') d\mathbf{r}' \\ &\equiv \int \epsilon(\mathbf{r},\mathbf{r}') \delta V_0(\mathbf{r}') d\mathbf{r}'\end{aligned}$$

where $\epsilon \equiv \delta(\mathbf{r}-\mathbf{r}') + e^2 \int \frac{\chi(\mathbf{r}'',\mathbf{r}')}{|\mathbf{r}-\mathbf{r}'|} d\mathbf{r}''$

For Kohn-Sham equation, $\delta n(\mathbf{r}) = \int \chi(\mathbf{r},\mathbf{r}') \delta V_{\mathrm{KS}}(\mathbf{r}') d\mathbf{r}'$, where $\delta V_{\mathrm{KS}} = \delta V_0 + \delta V_{\mathrm{H}} + \delta V_{\mathrm{XC}}$. In order to evaluate the charge denisty derivative, the 1st-order KS orbital perturbation can be expressed as:

$$\delta\psi_i(\mathbf{r}) = \sum_{j \neq i} \psi_j(\mathbf{r}) \frac{\langle \psi_j | \, \delta V_{\mathrm{KS}} \, | \psi_i \rangle}{\epsilon_i - \epsilon_j}$$

so $\delta n(\mathbf{r}) = \sum_i f_i \delta\psi_i^* \psi_i + c.c.$, where f_i is the occupation number, and δn can be further expressed as:

$$\delta n(\mathbf{r}) = 4\Re \sum_{ij, i \neq j} \frac{f_i - f_j}{\epsilon_i - \epsilon_j} \psi_i^* \psi_j \, \langle \psi_j | \, \delta V_{\mathrm{KS}} \, | \psi_i \rangle$$

With this, when the V_{KS} is *local*, the independent-particle (KS picture) polarizability is solved as:

$$\chi_0(\mathbf{r},\mathbf{r}') = 4\Re \sum_{c,v} \frac{\psi_v^*(\mathbf{r}) \psi_c(\mathbf{r}) \psi_c^*(\mathbf{r}') \psi_v(\mathbf{r}')}{\epsilon_v - \epsilon_c}$$

But what we need is χ instead of χ_0, i.e. the response to the external potential is needed. Remember $\delta n = \chi \delta V_0 = \chi_0 \delta V_{\rm KS}$, with little algebra, the χ can be expressed as:

$$\chi = (\chi_0^{-1} - v_c - f_{\rm xc})^{-1}$$

where v_c and $f_{\rm xc}$ are the functional derivatives of Hartree and EX potentials, respectively. In the plane-wave code, χ_0 and χ are solved in the momentum space, i.e. written with the plane-wave basis set. These quantities will be used in the following perturbation calculations.

Phonon and electron-phonon coupling. From the Hellman-Feynman theorem,

$$\frac{\partial \epsilon}{\partial \lambda_i} = \int n_\lambda(\mathbf{r}) \frac{\partial V_\lambda(\mathbf{r})}{\partial \lambda_i} d\mathbf{r}$$

where λ is a variable to control perturbation [28]. By expanding the potential as $V = V_0 + \sum_i \lambda_i \frac{\partial V_\lambda}{\partial \lambda_i} + \dots$ and charge density $n = n_0 + \sum_i \lambda_i \frac{\partial n_\lambda}{\partial \lambda_i} + \dots$, the above equation can be further expanded as (to the 1st order):

$$\begin{aligned}\frac{\partial \epsilon}{\partial \lambda_i} = & \int n_0 \frac{\partial V_\lambda(\mathbf{r})}{\partial \lambda_i} d\mathbf{r} \\ & + \sum_j \lambda_j \int \frac{\partial n_\lambda(\mathbf{r})}{\partial \lambda_j} \frac{\partial V_\lambda(\mathbf{r})}{\partial \lambda_i} d\mathbf{r} \\ & + n_0 \sum_j \lambda_j \int \frac{\partial V_\lambda^2(\mathbf{r})}{\partial \lambda_i \partial \lambda_j} d\mathbf{r}\end{aligned}$$

The above deferential of λ are evaluated when $\lambda = 0$. By integrate the above equation, it gives:

$$\epsilon = \epsilon_0 + \sum_i \lambda_i \int n_0(\mathbf{r}) \frac{\partial V_\lambda(\mathbf{r})}{\partial \lambda_i} d\mathbf{r} + \frac{1}{2} \sum_{i,j} \lambda_i \lambda_j \int \left[\frac{\partial n_\lambda(\mathbf{r})}{\partial \lambda_j} \frac{\partial V_\lambda(\mathbf{r})}{\partial \lambda_i} + n_0 \frac{\partial V_\lambda^2(\mathbf{r})}{\partial \lambda_j \partial \lambda_j} \right] d\mathbf{r}$$

Now, if we treat λ as the ion displacement $u_{\alpha,i}(\mathbf{R})$ (α is the components of the distortion x, y and z; i is the position of the atoms; $\mathbf{R}$ is the lattice vectors), the force constant matrix can be written as:

$$\begin{aligned} C_{\alpha i,\beta j}(\mathbf{R}-\mathbf{R}') &= \frac{\partial \epsilon^2}{\partial u_{\alpha,i}(\mathbf{R}) \partial u_{\beta,j}(\mathbf{R}')} \\ &= C^{\text{ionic}}_{\alpha i,\beta j}(\mathbf{R}-\mathbf{R}') + C^{\text{elec}}_{\alpha i,\beta j}(\mathbf{R}-\mathbf{R}') \end{aligned}$$

The ionic contribution can evaluated by performing derivative Ewald summation. The electronic part will be:

$$C_{\alpha i,\beta j}(\mathbf{R}-\mathbf{R}') = \int \frac{\partial n(\mathbf{r})}{\partial u_{\alpha,i}(\mathbf{R})} \frac{\partial V(\mathbf{r})}{\partial u_{\beta,j}(\mathbf{R}')} + n_0(\mathbf{r}) \frac{\partial V^2(\mathbf{r})}{\partial u_{\alpha,i}(\mathbf{R}) \partial u_{\beta,j}(\mathbf{R}')} d\mathbf{r}$$

In the plane-wave code, the force constant is evaluated in the momentum space as $C(\mathbf{q})$. $C_{\alpha i,\beta j}(\mathbf{R}-\mathbf{R}') = \frac{1}{N} \sum_{\mathbf{q}} \mathrm{e}^{i\mathbf{q}\cdot(\mathbf{R}-\mathbf{R}')} \tilde{C}_{\alpha i,\beta j}(\mathbf{q})$. The detailed form for the force constant is expressed as:

$$C_{\alpha i,\beta j}(\mathbf{q}) = \int \left[\frac{\partial n(\mathbf{r})}{\partial u_{\alpha i \mathbf{q}}} \right] \frac{\partial V(\mathbf{r})}{\partial u_{\beta j \mathbf{q}}} d\mathbf{r} + \int n_0(\mathbf{r}) \frac{\partial V^2(\mathbf{r})}{\partial u_{\alpha i,\mathbf{q}=0} \partial u_{\beta j \mathbf{q}=0}} d\mathbf{r}$$

with $u_{\alpha,i}(\mathbf{R}) = u_{\alpha i\mathbf{q}} \mathrm{e}^{i\mathbf{q}\cdot\mathbf{R}}$. Finally, the *dynamic matrix* D can be solved as:

$$\tilde{D}_{\alpha i,\beta j}(\mathbf{q}) = \frac{\tilde{C}_{\alpha i,\beta j}(\mathbf{q})}{\sqrt{M_i M_j}}$$

The phonon eigenvectors and eigenvalues are solved by diagonalizing the dynamic matrix. Here, the density response ($\frac{\partial n}{\partial u}$) will be solved based on the linear response as mentioned before.

Electron-phonon coupling. The most important quantity of describing the electron-phonon coupling is the electron-phonon coupling matrix element g. This matrix element can be written as:

$$g_{\mathbf{q},\nu}(\mathbf{k}, i, j) = \left(\frac{\hbar}{2M\omega_{\mathbf{q}\nu}}\right)^{\frac{1}{2}} \langle\psi_{i,\mathbf{k}}| \frac{\partial V_{\mathrm{KS}}}{\partial u_{\mathbf{q}\nu}} |\psi_{j,\mathbf{k}+\mathbf{q}}\rangle$$

where $\mathbf{q}$ and $\mathbf{k}$ are the wavevectors for phonons and electrons. ν is the mode index. ψ is the electronic wavefunction and u is the phonon eigenmode.

2.3 Light-matter Interaction

Interaction picture and evolution operator. Following are the important definations and properties of the interaction picture and the evolution operator.

The evolution operator U is defined as:

$$|\psi(t)\rangle_I = U_I(t) |\psi(t=0)\rangle_I$$

Here, recall that $|\psi(t=0)\rangle_I = |\psi(t=0)\rangle$. The subscript I indicates the interaction picture is used.

For the interaction picture and Schrodinger picture transformation, it follows:

$$
\begin{aligned}
|\psi(t)\rangle_I &= \mathrm{e}^{i/\hbar H_0 t} |\psi(t=0)\rangle \\
\mathcal{O}(t)_I &= \mathrm{e}^{i/\hbar H_0 t} \mathcal{O}(t) \mathrm{e}^{-i/\hbar H_0 t} \\
U_I(t) &= \mathrm{e}^{i/\hbar H_0 t} U(t)
\end{aligned}
$$

where H_0 is the Hamiltonian without time dependence. $\mathcal{O}$ is a general operator.

When adding the time-dependent perturbation $V(t)$, the interaction picture for the Schodinger equatoin turns out to be:

$$
i\hbar \frac{\partial U_I(t)}{\partial t} = V_I(t) U_I(t)
$$

By solving this differential equation, the evolution operator is:

$$
U_I(t) = 1 - \frac{i}{\hbar} \int_0^t V_I(t') U_I(t') dt'
$$

With such expansion, we have

$$
\begin{aligned}
&\text{First order} : U_I(t)^{(1)} = 1 - \frac{i}{\hbar} \int_0^t V_I(t') dt' \\
&\text{Second order} : U_I(t)^{(2)} = 1 - \frac{i}{\hbar} \int_0^t V_I(t') dt' - \frac{1}{\hbar^2} \int_0^t dt' \int_0^{t'} dt'' V_I(t') V_I(t'')
\end{aligned}
$$

Assuming the system is at the ground state $|n\rangle$ when $t = 0$, we can derive the wavefunction of $t = t$ for any order using the above time evolution operator. As an example, here, the perturbation Hamiltonian is written as $V(t) = \frac{e}{m}\mathbf{A}(t) \cdot \mathbf{p} = \frac{e}{m}\mathbf{A_0}\cos(\omega t) \cdot \mathbf{p}$, which is the light-matter coupling with the light frequency ω and the vector field $\mathbf{A}$ coupled with the momentum $\mathbf{p}$ of the material. The dipole approximation (long wavelength approximation) is used due to the large wavelength of the photon compared to the lattice vectors.

First-order response. The first-order perturbed crystal polarization due to light illumination can be derived by solving the responses χ with $P(\omega) = \chi(\omega)E(\omega)$ ($\mathbf{E}$ is the electric field of the light). Using the above evolution operator, the first-order perturbed wavefunction is:

$$|\psi(t)^{(1)}\rangle_I = \left[1 - \frac{i}{\hbar}\int_0^t V_I(t')dt'\right]|\psi(0)\rangle_I$$

If we rewrite the perturbation term, $V(t) = \frac{e}{2m}\mathbf{A_0}(\mathrm{e}^{\omega t} + \mathrm{e}^{-\omega t})\mathrm{e}^{\eta t} \cdot \mathbf{P}$, where η ($0 < \eta \ll 1$) is to assume that the ground state condition is set to $-\infty$ instead of $t = 0$ for simplicity.

By recasting the perturbation into the wavefunction evolution, if we only expand the $\mathrm{e}^{\omega t}$ term, we have:

$$|\psi(t)^{(1)}\rangle_I = |n\rangle + \frac{ie}{\hbar m}\int_{-\infty}^t \mathrm{e}^{\frac{i}{\hbar}H_0 t'}\mathrm{e}^{i\omega t'}\mathbf{A_0} \cdot \mathbf{p}\mathrm{e}^{-\frac{i}{\hbar}H_0 t'}|n\rangle$$

By inserting the expansion $1 = \sum_{n'}|n'\rangle\langle n'|$, the above equation will be:

$$|\psi(t)^{(1)}\rangle_I = |n\rangle + \frac{ie}{\hbar m}\mathbf{A_0} \cdot \sum_{n'}|n'\rangle\langle n'|\mathbf{p}|n\rangle\frac{\mathrm{e}^{i(\omega_n - \omega_{n'} + \omega)t + \eta t}}{i(\omega_n - \omega_{n'} + \omega) + \eta}$$

Now we can derive the total polarization of the crystal by evaluating $\mathbf{P}(t) = \langle\psi(t)|\,\mathbf{r}\,|\psi(t)\rangle$, where $\mathbf{r}$ is the position operator. Thus, the first-order total polarization is:

$$\begin{aligned}
\bar{\mathbf{P}}^{(1)} &= \langle\psi(t)_I^{(1)}|\,\mathbf{r}_I\,|\psi(t)^{(1)}\rangle_I \\
&= \langle n|\,\mathbf{r}\,|n\rangle \\
&+ \frac{ie}{\hbar m}\mathbf{A_0}\sum_{n'}\langle n|\,\mathbf{r}_I\,|n'\rangle\,\langle n'|\,\mathbf{p}\,|n\rangle\,\frac{\mathrm{e}^{i(\omega_n-\omega_{n'}+\omega)t+\eta t}}{i(\omega_n-\omega_{n'}+\omega)+\eta} \\
&- \frac{ie}{\hbar m}\mathbf{A_0}\sum_{n'}\langle n|\,\mathbf{p}\,|n'\rangle\,\langle n'|\,\mathbf{r}_I\,|n\rangle\,\frac{\mathrm{e}^{-i(\omega_n-\omega_{n'}+\omega)t+\eta t}}{-i(\omega_n-\omega_{n'}+\omega)+\eta}
\end{aligned}$$

The position operator can be further replaced with momentum operator by using the Heisenberg equation of motion:

$$\langle n|\,\mathbf{r}\,|n'\rangle = \frac{i}{m_e}\frac{\langle n|\,\mathbf{p}\,|n'\rangle}{\omega_n-\omega_{n'}},\ \text{when } n\neq n'$$

Therefore, the polarization will be:

$$\begin{aligned}
\bar{\mathbf{P}}^{(1)} &= \bar{\mathbf{P}_0} \\
&- \frac{e}{\hbar m^2}\mathbf{A}\sum_{n'}|\langle n|\,\mathbf{p}\,|n'\rangle|^2\,\frac{\mathrm{e}^{i\omega t+\eta t}}{i(\omega_{n'}-\omega_n+\omega)+\eta}\frac{1}{\omega_n-\omega_{n'}} \\
&+ \frac{e}{\hbar m^2}\mathbf{A}\sum_{n'}|\langle n|\,\mathbf{p}\,|n'\rangle|^2\,\frac{\mathrm{e}^{-i\omega t+\eta t}}{i(\omega_{n'}-\omega_n+\omega)-\eta}\frac{1}{\omega_n-\omega_{n'}}
\end{aligned}$$

where $\bar{\mathbf{P}_0}$ is the permanent polarization of the material. Since we want to solve the polarization in momentum space, a Fourier transform is performed as $\mathbf{P}(\omega) = \int_{-\infty}^{t}\mathrm{e}^{i\omega t-\eta t}\mathbf{P}(t)$. So the induced polarization will be:

$$\bar{\mathbf{P}}^{(1)} = \frac{ec}{i\omega\hbar m^2}\mathbf{E}\sum_{n'}\left|\langle n|\,\mathbf{p}\,|n'\rangle\right|^2\frac{1}{i(\omega_{n'}-\omega_n+\omega)-\eta}\frac{1}{\omega_n-\omega_{n'}}$$

recalling the relation $\mathbf{E}(\omega) = i\omega\mathbf{A}(\omega)/c$. Thus, polarization response χ to the light electric field $\mathbf{E}$ can be expressed as:

$$\begin{aligned}\chi(\omega) &= \frac{ec}{\omega\hbar m^2}\sum_{n'}\left|\langle n|\,\mathbf{p}\,|n'\rangle\right|^2\frac{1}{-(\omega_{n'}-\omega_n+\omega)-i\eta}\frac{1}{\omega_n-\omega_{n'}}\\ &= -\frac{ec}{\omega\hbar m^2}\sum_{n'}\left|\langle n|\,\mathbf{p}\,|n'\rangle\right|^2\frac{1}{\omega_n-\omega_{n'}}\left(\pi\delta(\omega_{n'}-\omega_n+\omega)+i\mathcal{P}\frac{1}{\omega_{n'}-\omega_n}\right)\end{aligned}$$

The above formula can be split into two parts: the real part and the imaginary part. The imaginary part describes the real transitions owing to the delta function, requiring the energy of the photon to be the same to the bands' energies difference. It can be approved that the real part and imaginary part satisfy the Kronig-Kramer's relation analytically and numerically.

Here, we only expand the contribution from the $\mathrm{e}^{i\omega t}$. The $\mathrm{e}^{-i\omega t}$ will give similar results. Moreover, the electronic occupation of the states are implicit. This is because we assume that $|n\rangle$ is the valence state and $|n'\rangle$ are the conduction state. For the above derivation, the density matrix technique (Liouville picture) can also be used, and it should give the same results.

The susceptibility is the response of the polarization to the light perturbation. From this response, the absorption coefficient, refractive index, optical dielectric, and loss functions can be derived as they all belong to the first-order (linear response) properties of materials.

Second-order response and shift current. The perturbed wavefunction can be further expanded to the second order under the light illumination.

$$|\psi(t)\rangle = |\psi(0)\rangle + |\psi(t)^{(1)}\rangle + |\psi(t)^{(2)}\rangle + \dots$$

From the above example of the first-order expansion, $|\psi(t)\rangle^{(1)}$ will contain the term $\mathrm{e}^{i\omega t}$, i.e. oscillate with the same frequency as light. For the second-order term, we can imagine that the light perturbation operator will apply to the wavefunction twice, which can create $\mathrm{e}^{2i\omega t}$ term, $\mathrm{e}^{-2i\omega t}$ term, and zero frequency term ($\mathrm{e}^{i\omega t - i\omega t}$). The first two conditions actually is the basis for the second-harmonic generation by oscillating with twice the frequency of the light. The last condition without any oscillation may act as the carrier state to generate DC current which is the shift current. For example, if the expectation value of the momentum is evaluated for the current up to the second order, it will be:

$$\begin{aligned}\mathbf{J} &= \langle\psi(t)|\,\mathbf{p}\,|\psi(t)\rangle \\ &= \langle\psi(0)|\,\mathbf{p}\,|\psi(t)^{(2)}\rangle + \langle\psi(t)^{(2)}|\,\mathbf{p}\,|\psi(0)\rangle + \langle\psi(t)^{(1)}|\,\mathbf{p}\,|\psi(t)^{(1)}\rangle\end{aligned}$$

where all the terms can provide the none oscillating contribution to the total current. Here, I will not show the derivation of the shift current. People can find the details in Ref. [29, 30].

The short-circuit shift current response σ is a rank three tensor, and it can be computed

using perturbation theory, yielding the formula in the *thin* sample limit as

$$
\begin{aligned}
J_q &= \sigma_{rsq} E_r E_s \\
\sigma_{rsq}(\omega) &= \pi e \left(\frac{e}{m\hbar\omega}\right)^2 \sum_{n',n''} \int d\mathbf{k} \left(f[n''\mathbf{k}] - f[n'\mathbf{k}]\right) \\
&\quad \times \langle n'\mathbf{k}| \hat{P}_r |n''\mathbf{k}\rangle \langle n''\mathbf{k}| \hat{P}_s |n'\mathbf{k}\rangle \\
&\quad \times \left(-\frac{\partial \phi_{n'n''}(\mathbf{k},\mathbf{k})}{\partial k_q} - [\chi_{n''q}(\mathbf{k}) - \chi_{n'q}(\mathbf{k})]\right) \\
&\quad \times \delta\left(\omega_{n''}(\mathbf{k}) - \omega_{n'}(\mathbf{k}) \pm \omega\right)
\end{aligned}
$$

where n and $\mathbf{k}$ are, respectively, the band index and wave-vector, f is the occupation, $\hbar\omega_n$ is the energy of state n, $\phi_{n',n''}$ is the phase of the momentum matrix element between state n' and n'' and χ_n is the Berry connection for state n. If spin-orbit coupling is considered, each Bloch state has spinor form and the current response becomes a sum over spinor components. Here, the response σ can be written with respect to the intensity instead of the electric field for simplicity. In this case, the unit transformation $|\mathbf{E}|^2 = \frac{2n}{\epsilon_r \epsilon_0 c} I_0$ is needed, where n is the refractive index; ϵ_r and ϵ_0 are the relative and vacuum susceptibilities; I_0 is the incoming light intensity.

In a *thick* sample, considering the light absorption coefficient $\alpha_{rr}(\omega)$, the current response can be described by the Glass coefficient G [31]

$$
G_{rrq} = \frac{\sigma_{rrq}}{\alpha_{rr}}
$$

When measuring in-plane current, the current is dependent on the device architecture (Fig. 2.1).

- When the current direction in the cell is perpendicular to the light illuminatono direction. The total current $\mathbf{J}$ is $J_q(\omega) = G_{rrq} I_r w$, where I is the light intensity and w

is the sample width.

- When the current direction is parallel to the light illumination direction. The current will be $J_q(\omega) = \frac{G_{rrq} I_r}{D} A$, where D is the thickness of the sample, and A is the area of the electrode.

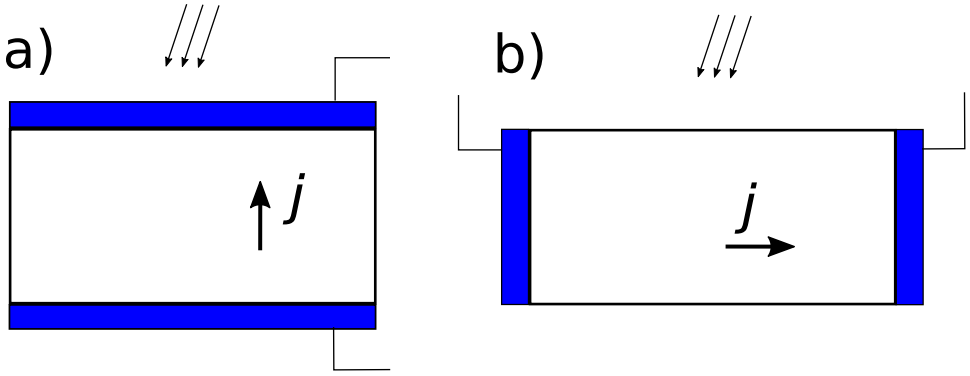

Figure 2.1: The two types of device architecture. The blue bar indicate the electrode position: a) current is parallel to the light illumination direction, b) current si perpendicular to the light illumination direction. Their charge current formula using Glass coefficient will be different.

Chapter 3

Substantial optical dielectric enhancement by volume compression in $LiAsSe_2$

[1]

[1] F. Zheng, J. A. Brehm, S. M. Young, Y. Kim and A. M. Rappe, *Phys. Rev. B*, **93**, 195210 (2016)

3.1 Introduction

The dielectric response, as a fundamental physical property of materials, describes how materials respond to an external electric field. In semiconductors, when the applied electric field frequency is in the range of visible light, the photon excitation of electronic inter-band transitions dominates the total dielectric response, which is described by the optical dielectric function. The optical dielectric function is strongly related to other optical properties of the material, including light absorption, refraction and non-linear optical responses. Therefore, the enhancement and tunability of the optical dielectric function of a material are significantly important in various areas, such as solar cell, optical devices and sensors. A great deal of research has been done to increase the material optical dielectric response. In particular, defects, material doping and surface plasmon induced by metallic nanoparticles have been widely used to increase the optical absorption in semiconductors [19, 20, 21, 22, 23]. Whereas most of the previous methods rely on the assistance of another material, the intrinsic bulk dielectric response enhancement of the light absorber is less studied.

Alkali-metal chalcogenides such as $KPSe_6$, $K_2P_2Se_6$, $LiAsSe_2$, $LiAsS_2$ and $NaAsSe_2$ have been synthesized, and their band gaps lie in the visible light region [32]. Since they have spontaneous polarization, these materials are potential candidates to show the bulk photovoltaic effect [33]. Moreover, strong optical second-harmonic generation susceptibility has been observed experimentally and theoretically [32, 34, 35]. However, the effect of structural distortion on their linear optical responses has not been studied[36], and the structure-property-optical performance relationship is still unclear. In this paper, by using a first-principles method, we show that the optical dielectric constant of $LiAsSe_2$ increases threefold by volume compression. More interestingly, As and Se atoms in $LiAsSe_2$ form weakly interacting quasi-one-dimensional atomic chains, of which the dimerization

strength can be tuned by volume compression. Atomic chains have attracted a great deal of interest, due to their one-dimensional nature giving rise to exotic phenomena such as conductivity [37, 38], metal-insulator transition [39], and topological phases [40, 41]. Herein, their important roles in light absorption are emphasized. As illustrated by a tight-binding model, the dimerization strength is strongly coupled to the relative phases of the gap state wavefunctions between the two neighboring chains. By reducing the wavefunction phase mismatch between the chains, the magnitude of transition intensity for the transitions near the band edges increase significantly, giving rise to substantial optical dielectric function enhancement.

3.2 Computational Method

Figures 3.1a and b show the experimental structure (ES) of $LiAsSe_2$ [32]. The polar phase of $LiAsSe_2$ has the Cc space group with the glide plane perpendicular to the lattice vector $\vec{b}$. The polarization induced by ionic displacement lies in the $\vec{a}$-$\vec{c}$ plane [33]. As shown, the As and Se atoms form distorted quasi-one-dimensional atomic chains along the $\vec{b}$ direction[42]. This chain and its neighboring chains form a two-dimensional chain plane (illustrated as the grey plane), and these chain planes are separated by Li-Se planes (light purple plane). In the ES, this As–Se chain dimerizes, creating alternating As–Se bonds with two different bond lengths.

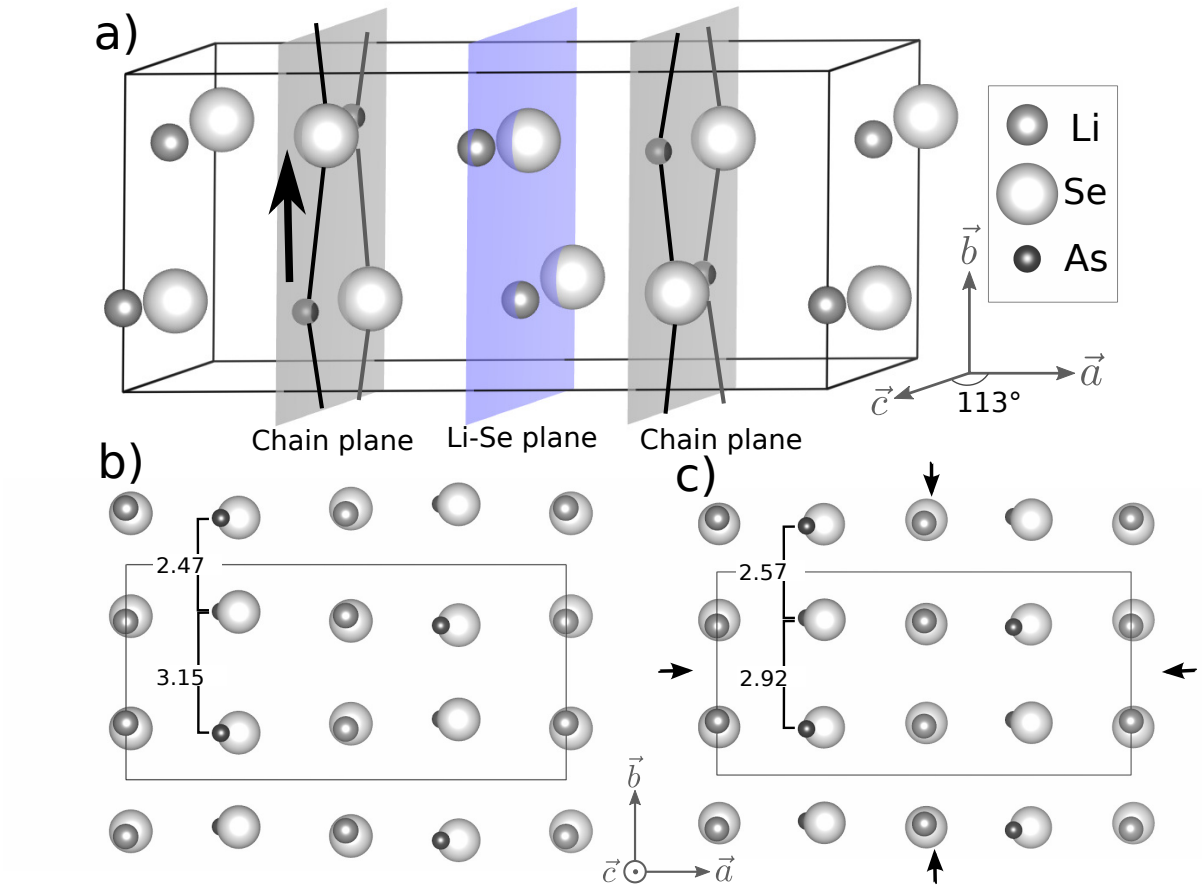

Figure 3.1: a) The unit cell of $LiAsSe_2$. The lines between As and Se atoms indicate the quasi-one-dimensional chains. The chain with its neighbor chains form a chain plane (grey color plane). These parallel chain planes are separated by the Li-Se plane (light purple plane) in the middle. b) Side view of the experimental structure (ES). c) Side view of the compressed structure (CS). The differences between the ES and the CS are mainly ion motions in the $\vec{b}$ direction. As illustrated by the bond lengths between two neighboring As–Se bonds, ES shows stronger dimerization strength along the chain than CS.

The plane-wave density functional theory (DFT) package QUANTUM-ESPRESSO was used to perform structural relaxations and electronic structure calculations, with the Perdew-Burke-Ernzerhof (PBE) generalized gradient approximation exchange-correlation functional [43]. Norm-conserving, designed non-local pseudopotentials were generated with the OPIUM package [44, 45]. A plane-wave cutoff energy of 50 Ry was sufficient to converge the total energy with the k-point sampling on a $4\times8\times8$ grid. The structure relaxed with the PBE functional underestimates the dimerization along the chain, and it does not match with the ES. By using the GGA + U method with effective Hubbard $U_{\text{eff}} = 7.5$ eV on the As 4 p orbitals, the relaxed structure matches the ES very well. Adding U on p orbitals to get the correct structure is not rare, as the large self-interaction error originating from s or p orbitals may partially be corrected by the DFT+U method [46, 47]. The DFT calculated band gap is 0.8 eV, which underestimates the experimentally measured 1.1 eV [32]. With the converged charge density, the wavefunctions used for the dielectric function calculations are obtained from non-self-consistent calculations performed on a denser k-point grid of $20\times36\times36$ and a sufficient number of empty bands (76 empty bands). By using the long wavelength approximation and the single particle approximation, the imaginary part of the optical dielectric function is calculated as Eq.(3.1),

$$\epsilon_{2,ii}(\omega) = \frac{\pi}{2\epsilon_0}\frac{e^2}{m^2\left(2\pi\right)^4\hbar\omega^2}\sum_{c,v}\int_{BZ} d\mathbf{k}\left|\langle c,\mathbf{k}|\, p_i\,|v,\mathbf{k}\rangle\right|^2\delta(\omega_{c,\mathbf{k}}-\omega_{v,\mathbf{k}}-\omega) \qquad (3.1)$$

where ω is the light frequency; i is the Cartesian coordinate; $\mathbf{k}$ is the Bloch wave vector; c, v denote the conduction and valence band with energy $\hbar\omega_{c/v}$. The real part of the dielectric function, ϵ_1, can be calculated from the Kramers-Kronig relation.

3.3 Results and Discussion

The compressed structure (CS), with much weaker dimerization strength of the atomic chains (Fig. 3.1c), is obtained by compressing all the lattice vectors by 3%, followed by the relaxation of the internal atomic positions[42]. This compression corresponds to approximately 27 kbar stress applied almost hydrostatically. The volume compression of $LiAsSe_2$ strongly enhances its optical dielectric response as shown in the calculated optical dielectric functions of the ES and CS (Fig. 3.2a). Furthermore, we find that the dielectric function changes continuously *vs*. applied compression. Other compression strengths are also tested as shown in the Appendix Figure.1.9. Figures 3.2b, c and d illustrate the calculated joint density of states (JDOS), refractive index and absorption spectrum along the $\vec{b}$ direction as a function of the photon energy for the ES and CS, respectively. Two other components of the optical dielectric function are also shown in the Appendix Fig.10, showing much less enhancement under compression. As shown from the spectrum, the CS shows much higher linear optical responses near the band gap than the ES. In particular, the optical dielectric constant of the CS increases to more than three times its original value (Fig. 3.2a). The imaginary part of the optical dielectric function, describing the real electronic inter-band transitions, also shows great enhancement under compression. As expressed in Equation (3.1), the imaginary part of the dielectric function is the product of JDOS $\sum_{c,v,\mathbf{k}} \delta(\omega_{c,\mathbf{k}} - \omega_{v,\mathbf{k}} - \omega)$ and the transition intensity $|\langle c, \mathbf{k}| \, p_i \, |v, \mathbf{k}\rangle|^2$. However, we find that the JDOS contribution to the enhancement is negligible. As shown in Fig. 3.2b, in the energy range $0 < \hbar\omega < 2$ eV where the imaginary part ϵ_2 shows substantial enhancement, the calculated JDOS for the ES and CS (shifted) have very similar magnitude. Here, we want to emphasize that owing to the different band gaps (0.2 eV) of the ES and CS, the JDOS of the CS is shifted by 0.2 eV in order to compare. Therefore, this dielectric function enhancement mainly comes from the increase of transition intensity by compression.

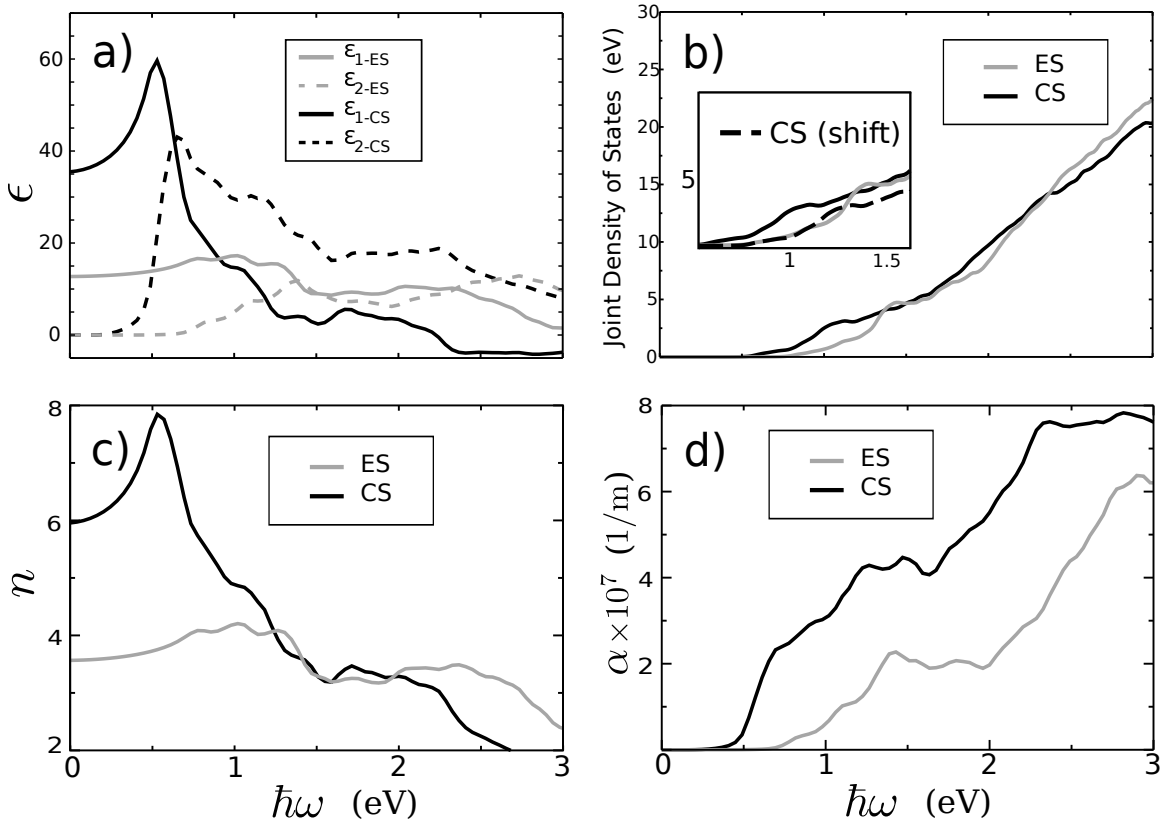

Figure 3.2: a) $LiAsSe_2$ optical dielectric (ϵ) function spectrum of the ES and CS as a function of photon energy along $\vec{b}$. ϵ_1 is the real part of the dielectric response spectrum, and ϵ_2 is the imaginary part. b) Joint density of states for the two structures. Owing to the different band gaps of the ES and CS (0.2 eV difference), the inset graph shows the shifted-CS (shifting the spectrum by 0.2 eV) and ES JDOS spectra in order to compare with the same band gaps. c) Refractive index (n) spectrum along $\vec{b}$. d) Absorption coefficient (α) spectrum $\vec{b}$.

To further resolve the origin of the dielectric enhancement by pressure, we present the distribution of the transition intensity as a function of $\mathbf{k}$ in momentum space. Figure 3.3 shows the transition intensity distributions in the Brillouin zone (BZ), with the transitions between the valence band maximum (VBM) to the conduction band minimum (CBM) within the the energy range of 0–2 eV, since these transitions are dominant in the dielectric function enhancement. As displayed in Figure 3.3, the k-resolved distributions show distinct patterns in addition to their overall differences in the corresponding dielectric constants. For the ES, most of the $\mathbf{k}$ points have similar yet low magnitude of transition intensities. However, for the CS, the k-resolved transition intensity shows significant changes, with the high magnitude $\mathbf{k}$ points mostly distributed on a thin plane perpendicular to the reciprocal lattice vector $\vec{k}_b$. The $\mathbf{k}$ points contributing the highest transition intensities are broadly located in the middle region in this plane. Along the $\vec{k}_a$ and $\vec{k}_c$ directions of this plane, the transition intensity changes slowly with respect to wavevectors, indicating the weak bonding character. This can be attributed to the weak As/Se–Se/Li inter-planar and As–Se inter-chain interactions. However, the magnitude of transition intensity shows rapid change along the $\vec{k}_b$ direction, as illustrated by the transition intensity profile along this direction (Fig. 3.7b). This strong k-dependent transition intensity distribution reveals the strong covalent bonds character along the chain direction. The highly inhomogeneous distribution of the transition intensity can be considered as an indication of the quasi one-dimensional nature of the system near the low-energy spectrum, stemming from the dimerization changes of the As and Se atoms. Furthermore, the structural inhomogeneity leads to anisotropic optical responses as shown by the other two components of the dielectric functions (Appendix Fig.10), where only the dielectric response along chain direction is enhanced significantly when applying compression. Therefore, investigating the electronic structure of the chains is essential to further understand the origin of the dielectric response enhancement.

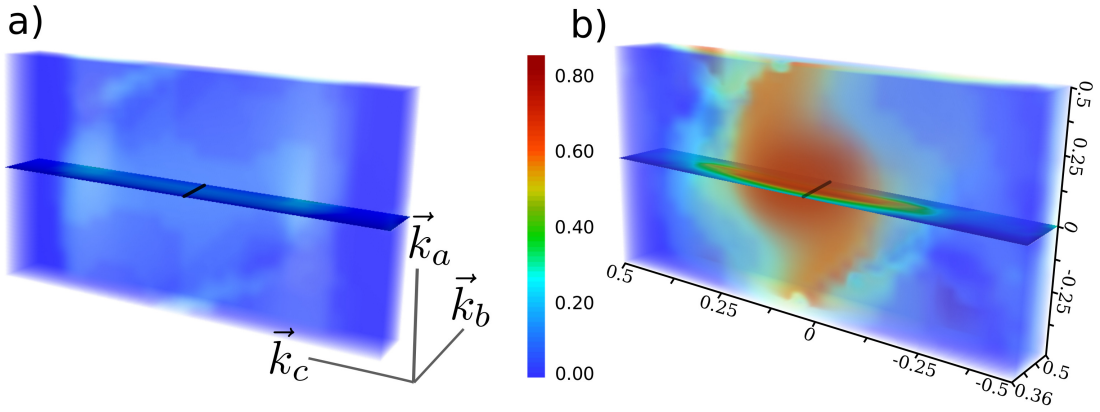

Figure 3.3: Distribution of $|\langle\psi_{v,\mathbf{k}}|\,\mathbf{p}\,|\psi_{c,\mathbf{k}}\rangle|^2/V$ (eV/Å^3) in the Brillouin zone (BZ) extracted from DFT calculation of $LiAsSe_2$ for a) the ES and b) CS. V is the volume of the unit cell. For simplicity, the primitive BZ is illustrated as an orthogonal box with reciprocal lattice vectors $\vec{k}_a$, $\vec{k}_b$, and $\vec{k}_c$ along the three edges of the box. The transitions with transition energy less than 2 eV are plotted, as this energy region shows the greatest dielectric function enhancement. The detailed transition intensity profiles along the black lines in the figures for the ES and CS are shown in Fig. 3.7b.

Figure 3.4 shows the DFT band structures plotted along Γ–Y. Under compression, most bands along the $\vec{k}_b$ direction show relatively small changes, except the bands near the band edges. The CS shows strong dispersion near its optical gap at $(0.0, 0.42, 0.0)$ (fractional coordinate), as its CBM shows a "dip" while the VBM shows a "bump". The ES has its band gap shifted towards the BZ boundary at $(0.0, 0.46, 0.0)$. Comparing to those of the CS, the bands of the ES near the band gap shows much less dispersion, and the dip and bump features become less obvious. Besides the band dispersion change, the band gap shows noticeable change from 0.80 eV (ES) to 0.62 eV (CS). More importantly, we find that the inter-band transition between the band edges in the CS provides the highest transition intensity magnitude, but this corresponding value in the ES is very low. In order to understand the bonding characters of these states which give the highest transition intensity, the charge density iso-surfaces of the VBM and CBM are plotted in Figure 3.4. Unexpectedly, both the ES and CS show quite similar charge density distributions, with non-bonding Se p orbital character as VBMs and non-bonding As p as CBMs, suggesting that the atomic orbital overlaps cannot explain such large dielectric enhancement by compression due to their similar charge densities. Rather, we find that the dimerization change induced by the compression can strongly alter the phase of wavefunctions so as to vary transition intensity magnitude significantly, as we will discuss below.

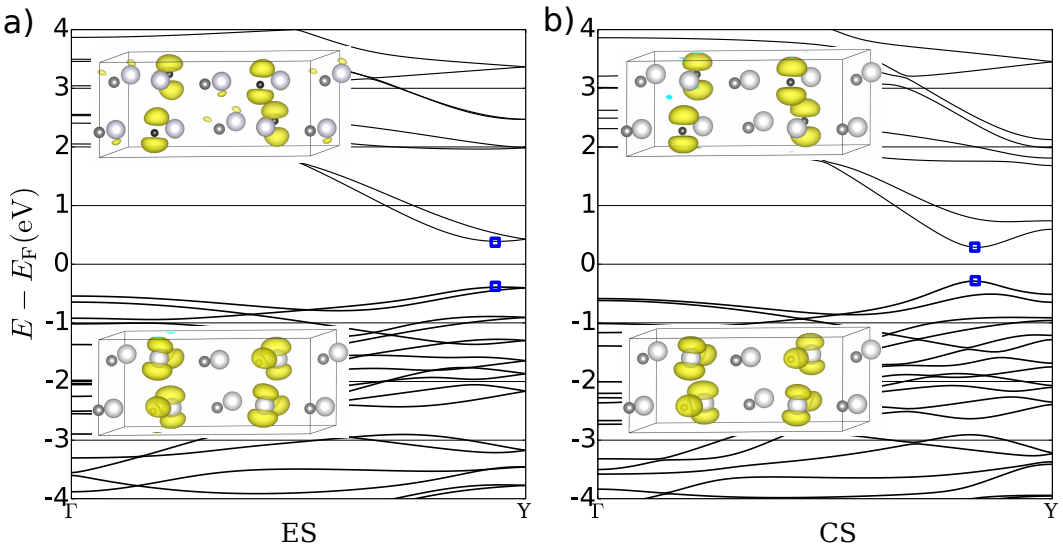

Figure 3.4: The band structure of $LiAsSe_2$ from Γ to Y $(0, \pi/b, 0)$ along $\vec{k}_b$, and the charge density iso-surfaces of the conduction band minimum (CBM) and valence band maximum (VBM) states indicated by the blue squares in the band structures for a) ES and b) CS.

To demonstrate the significant influence of wavefunction phase change on the optical response enhancement, we construct a two-dimensional (2D) tight-binding (TB) model with interacting atomic chains illustrated in Figure 3.5a. The TB model comprises four orbitals (i, j =1, 2, 3, 4) in a square lattice with lattice constant a and periodic boundary conditions along $\vec{b}$ and $\vec{c}$ to model a chain plane in $LiAsSe_2$. Owing to the weak interaction between the chain plane and the Se–Li plane, the inter-planar interaction along the $\vec{a}$ direction is not considered. As shown in the charge density distributions (Fig. 3.3) and the projected density of states (see Fig. 3.6 and Appendix Fig.8), the p orbitals from the As and Se atoms are crucial and they form σ-type covalent bonds along the chain (along the $\vec{b}$ direction). Thus, the TB Hamiltonian can be written as:

$$H(\mathbf{k}) = \sum_i \left(\epsilon_i c^\dagger_{i,\mathbf{k}} c_{i,\mathbf{k}}\right) + \sum_{\langle i,j\rangle} \left(t_{ij} c^\dagger_{i,\mathbf{k}} c_{j,\mathbf{k}} + \text{c.c.}\right) \tag{3.2}$$

where ϵ is the onsite energy and t is the hopping strength between nearest orbitals i and j. In this Hamiltonian, the onsite energies of As and Se orbitals are set to $E_0 + \delta E$ and $E_0 - \delta E$, respectively. The dimerized hopping strength is denoted as $t_1 \pm \delta t_1$ to describe the alternating As–Se bond lengths. By compression, the dimerization is reduced, leading to more even As–Se neighboring bond length along the chain, and the smaller δt_1 magnitude. Across the chains ($\vec{c}$-direction), π-bonding between the p orbitals forms, where the corresponding hopping interaction is denoted as $t_2 \pm \delta t_2$. We find that this inter-chain interaction is of crucial importance in reproducing the correct DFT band structure, although these interactions are weak relative to the intra-chain interaction, thus assuming $|t_2| < |t_1|$. The onsite energies and hopping strengths of the TB Hamiltonian are tuned to reproduce the DFT band structure near the band edges.

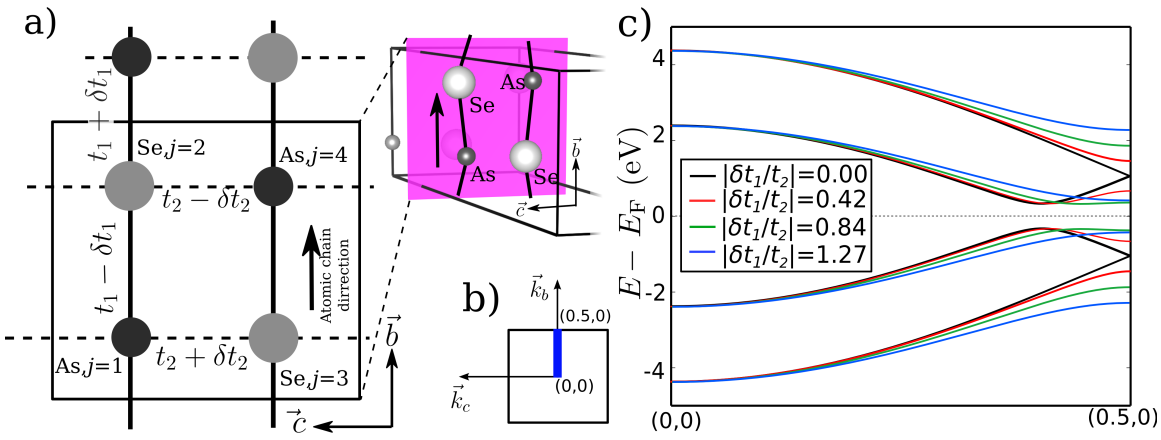

Figure 3.5: a) 2D TB model for weakly interacting As–Se chains (the inset graph shows the chains in $LiAsSe_2$). The dashed lines indicate the chain-chain interaction connecting the As–Se chains (solid lines). $t \pm \delta t$ denotes the hopping strength. b) The Brillouin zone of the 2D model. The band structure (graph c) is plotted along the thick blue line. c) The band structure calculated from the 2D TB model along the chain propagation direction under different dimerization strengths ($\delta t_1/t_2$ with t_2 fixed).

By solving the TB model numerically, we obtain the band structures in Fig. 3.5c plotted along the chain propagation direction indicated by the blue line in Fig. 3.5b. We also calculate the band structures by gradually reducing the dimerization strength (decreasing δt_1) with t_2 fixed, and find that the band gap position shifts away from the BZ boundary. Furthermore, the As p and Se p atomic orbital projections in DFT and the TB model are compared for the valence and conduction band as shown in Fig. 3.6. The TB model calculation shows the same orbital hybridization and the trend of change under compression to DFT, validating the TB model we use. In addition, the maximally-localized Wannier functions are computed for the ES and CS structures [48]. Their onsite energies and hopping strengths also fall into the range of the TB model in this work. From the TB band structure, the dispersion of the band edges are significantly enhanced when decreasing δt_1. This feature becomes clearer by calculating the k-resolved transition intensity using the TB wavefunctions.

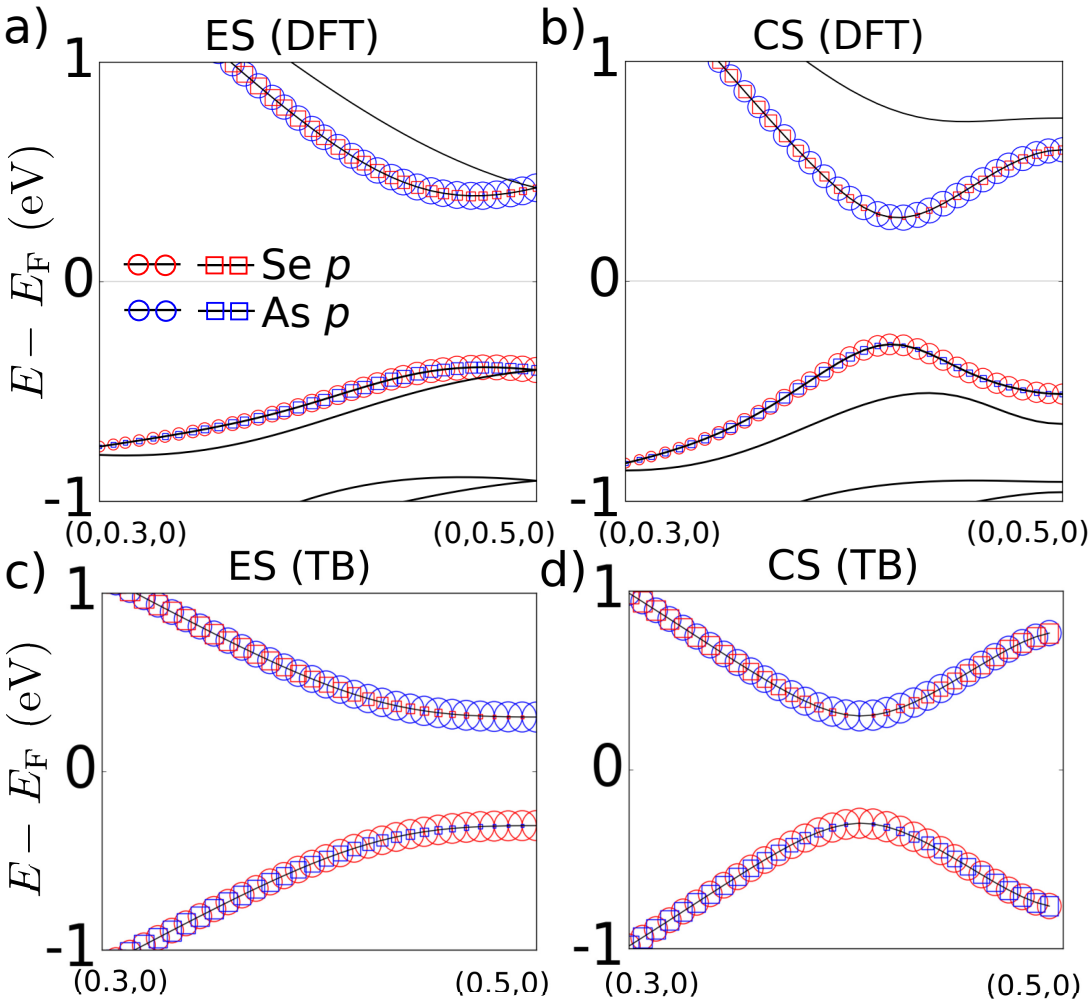

Figure 3.6: The Bloch wavefunction projection onto the Se p and As p orbitals along the bands for a) ES by DFT, b) CS by DFT, c) ES by TB and d) CS by TB. The size of the circle and square represents the atomic orbital contribution weight.

The transition intensity ($\mathcal{I}$) is expressed as $\mathcal{I}(\mathbf{k}) = |W^{v,c}(\mathbf{k})\,\Pi(\mathbf{k})|^2$, with $W^{v,c} = \sum_{j,j'} C^{v*}_{j',\mathbf{k}} C^{c}_{j,\mathbf{k}}$, summing over the contributions of the wavefunction coefficients to the transition intensity. In this case, Π accounts for the contribution generated when constructing the TB basis set from the localized atomic orbitals, with its relative value only determined by the wavevector without solving the Hamiltonian. Shown in Fig. 3.7 is the calculated $\mathcal{I}$ along the same k-path as used in the TB band structure (Fig. 3.5b). By reducing the dimerization strength of the atomic chains (reducing $\delta t_1/t_2$), the transition intensities for the band edge states and nearby increase significantly, which agrees well with the DFT transition intensity trend under compression shown in Fig. 3.7b. Additionally, by plotting W which is contributed only from the wavefunction as we are interested, it is clear that it shows exactly the same trend as $\mathcal{I}$, demonstrating the significant role of wavefunctions in the enhancement of the transition intensity under pressure.

The low-energy $k \cdot p$ effective theory provides simpler and more explicit band structure and wavefunction expression. The Hamiltonian $H(\mathbf{k})$ is further expanded in the vicinity of the BZ boundary as $H(\mathbf{k}) = H(\mathbf{K}) + (\mathbf{k} - \mathbf{K})H'(\mathbf{K})$ with $\mathbf{k} = \mathbf{K} + (q, 0)$, $\mathbf{K} = (\pi/b, 0)$. From the $k \cdot p$ Hamiltonian, the energies for the valence band (E_-) and the conduction band (E_+) near the BZ boundary are obtained as:

$$E_{\pm}(q) = \pm\sqrt{\delta E^2 - 2\sqrt{4t_2^2\Omega(q)} + 4\delta t_2^2 + \Omega(q)} \tag{3.3}$$

$$\Omega(q) = 4\delta t_1^2 + (qat_1)^2 \tag{3.4}$$

When $|\delta t_1| > |t_2|$, the band gap is at the BZ boundary ($q = 0$). By decreasing the dimerization strength such as $|\delta t_1| < |t_2|$, the band gap wavevector ($q(E_\mathrm{g})$) is $2\sqrt{t_2^2 - \delta t_1^2}/(at_1)$. This change of band gap position as a function of the dimerization strength ($\delta t_1/t_2$) agrees with our DFT band structures of $LiAsSe_2$. In the ES, the strong dimerization between the

As and Se atoms moves the band gap close to the BZ boundary. In the CS, the reduced dimerization due to the compression shifts the band gap away from the boundary, giving rise to the strong dispersion for the states near the gap. (The detailed derivation of the effective Hamiltonian is in the Appendix and Calculation Details.)

Within this low energy theory, the phase relationships of the wavefunctions are further explored by evaluating the analytical expression of wavefunctions for the band edge states. When the band gap is not at the BZ boundary ($|\delta t_1| < |t_2|$) , the wavefunctions of the gap states have simple forms:

$$\psi_{\mathrm{VBM}} = 1/\sqrt{2}\left(0, \mathrm{e}^{i\theta}, 1, 0\right), \tag{3.5}$$

$$\psi_{\mathrm{CBM}} = 1/\sqrt{2}\left(1, 0, 0, \mathrm{e}^{i\theta}\right) \tag{3.6}$$

where the wavefunctions are written with the TB basis of the four orbitals: $\chi_{\mathrm{As},j=1}$, $\chi_{\mathrm{Se},j=2}$, $\chi_{\mathrm{Se},j=3}$, and $\chi_{\mathrm{As},j=4}$ (Fig. 3.5a). Due to the simple form of the wavefunctions, we use these two states to show the effect of phases of the chains. Here, $\theta = \arcsin\left(|\delta t_1/t_2|\right)$ indicates the dimerization strength of the atomic chains. From the wavefunction expression, it is clear that the VBM and CBM are always non-bonding states without mixing of the As and Se orbitals, which is also observed in the DFT calculation. More interestingly, θ controls the phase mismatch between the wavefunctions of the two chains in the chain plane. For example, for the CBM wavefunction, when $\theta = 0$, the orbitals on $\chi_{\mathrm{As},j=1}$ and $\chi_{\mathrm{As},j=4}$ are populated in the same phase, while, with nonzero $\theta \neq 0$, $\chi_{\mathrm{As},j=1}$ on one chain and $\chi_{\mathrm{As},j=4}$ on the neighboring chain have the phase difference of $\mathrm{e}^{i\theta}$ between the corresponding wavefunction coefficients. Hence, the application of the hydrostatic stress to $LiAsSe_2$ reduces θ, enabling wavefunction phase matching between the two neighboring

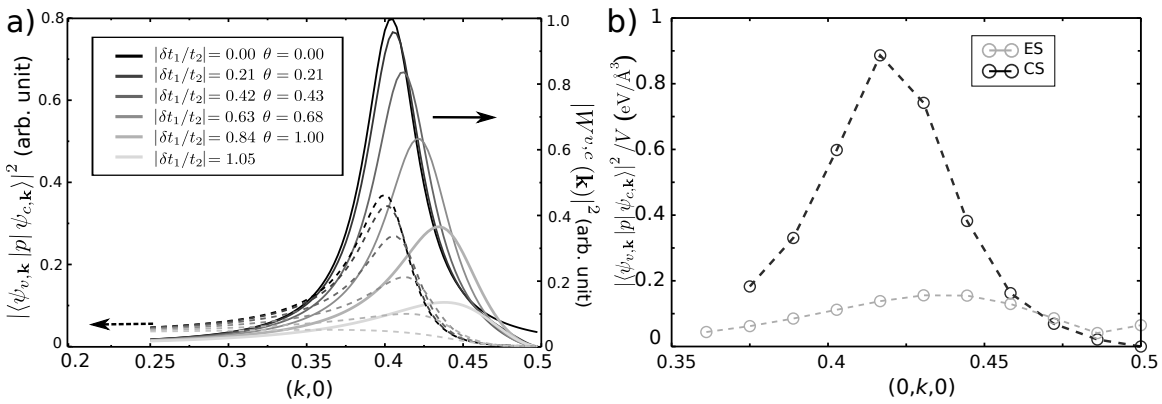

Figure 3.7: a) Calculated transition intensities $\mathcal{I}(\mathbf{k})$ and $|W^{v,c}(\mathbf{k})|^2$ ($W^{v,c}(\mathbf{k}) = \sum_{j,j'} C^{v*}_{j',\mathbf{k}} C^{c}_{j,\mathbf{k}}$) from 2D TB model. The x axis is the wavevector along the chain direction. b) Transition intensities (eV/Å^3) extracted from DFT calculation of transition intensity for the ES and CS. They are plotted along the chain direction as indicated by the short black lines in Fig. 3.3.

atomic chains, which is essential to the enhancement of dielectric responses.

Using this simple form of wavefunctions, the band edge transition intensity is evaluated as $\mathcal{I} \propto \left|e^{i\theta} + e^{-i\theta}\right|^2 = \cos^2(\theta) = 1 - (\delta t_1/t_2)^2$. The first exponential term $e^{i\theta}$ originates from one chain and the other term from the neighboring chain. (More details of transition intensity calculation using the TB model is in the Appendix and Calculation Details.) In this material, the finite dimerization strength of the two neighboring chains have opposite effects to their contributions to the transition intensity. Therefore, without varying the overlaps between the atomic orbitals, the phase change of the wavefunction induced by structural change alters the overall dielectric function significantly.

3.4 Conclusion

In summary, by using a first-principles method, we have shown that volume compression can significantly enhance the optical dielectric function and the dielectric constant by factor of three in $LiAsSe_2$. This material is essentially a network of As–Se 1D atomic chains with the dimerization strength tunable by compression. The enhancement of the transition intensity near band edges is the main reason of the overall dielectric function improvement. A 2D tight-binding model with weakly interacting atomic chains is developed to explore the relation of dimerization strength and transition intensity. When the dimerization is strong, the wavefunctions of the two neighboring chains have significant phase mismatch, providing destructive interference that reduces to the dielectric function. By reducing this wavefunction phase mismatch via compression, the collective contributions from the chains dramatically enhance the overall dielectric response and light absorption. Our results indicate that this material is suitable as the light absorber in the solar cell application. Furthermore, since the transition intensity is related to other optical processes such as second-harmonic generation and the non-linear optical effects, we expect that the volume compression can enhance their responses.

3.5 Appendix and Calculation details

Transition intensity and TB model

The Bloch wavefunction based on the TB orbitals is:

$$\psi_{n,\mathbf{k}} = \sum_j C_j^{n,\mathbf{k}} \chi_j^{\mathbf{k}} \tag{3.7}$$

$\chi_j^{\mathbf{k}}$ (j=1, 2, 3, and 4) is expanded as $\sum_{\mathbf{R}} \mathrm{e}^{i\mathbf{k}\cdot(\mathbf{R}+\mathbf{s}_j)}\phi_{\mathbf{R},j}$, and $\phi_{\mathbf{R},j}$ is the localized atomic orbital centering at the position of $\mathbf{R}+\mathbf{s}_j$.

With the Bloch wavefunctions, the transition intensity is expressed as:

$$\begin{aligned} \mathcal{I}(\mathbf{k}) &= \left|\langle\psi_{v,\mathbf{k}}|\,\mathbf{p}\,|\psi_{c,\mathbf{k}}\rangle\right|^2 \\ &= \left|\sum_{j,j'} C_{j',\mathbf{k}}^{v*} C_{j,\mathbf{k}}^{c} \Pi_{jj',x}\left(\mathbf{k}\right)\right|^2 \end{aligned} \tag{3.8}$$

where $\Pi_{j,j'}\left(\mathbf{k}\right) = \mathrm{e}^{i\mathbf{k}\left(\mathbf{s}_j-\mathbf{s}_{j'}\right)} \sum_{\bar{\mathbf{R}}} \mathrm{e}^{i\mathbf{k}\bar{\mathbf{R}}} \langle\phi_{-\bar{\mathbf{R}},j'}|\,\mathbf{p}\,|\phi_{0,j}\rangle$ with summation over nearest hopping neighbor unit cells denoted by $\bar{\mathbf{R}}$, which is only related to the wavevector, orbital position and the momentum matrix element between two localized atomic orbitals.

The low energy Hamiltonian is written as:

$$H(q) = \begin{bmatrix} E & i2\delta t_1 - qat_1 & 2t_2 & 0 \\ -i2\delta t_1 - qat_1 & -E & 0 & 2t_2 \\ 2t_2 & 0 & -E & i2\delta t_1 - qat_1 \\ 0 & 2t_2 & -i2\delta t_1 - qat_1 & E \end{bmatrix}$$

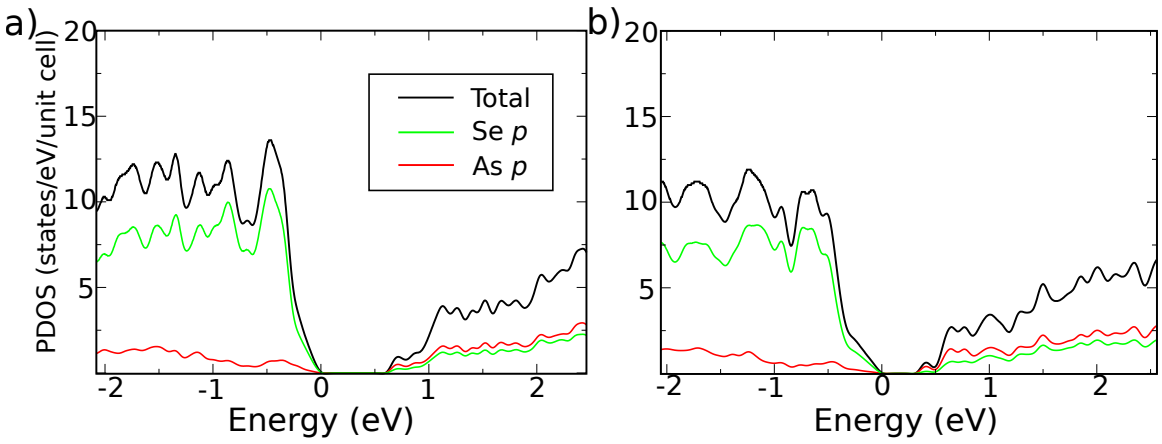

Figure 3.8: The projected density of states (PDOS) of the a) ES and b) CS. The band gap states are mainly Se p and As p orbital characters.

with respect to the four orbitals shown in Figure 3.5. Based on this Hamiltonian, the band edge states can be solved as Equations 4 and 5.

When calculating the transition intensity for band edge transitions, the transition intensity can be further simplified as:

$$\begin{aligned}\mathcal{I}(q) &= \left|C^{v*}_{j'=1,q}C^{c}_{j=0,q}\Pi_{j=0,j'=1} + C^{v*}_{j'=2,q}C^{c}_{j=3,q}\Pi_{j=3,j'=2}\right|^2 \\ &= \left|\mathrm{e}^{i\theta} + \mathrm{e}^{-i\theta}\right|^2 \left|\Pi\left(q\right)\right|^2 \\ &\equiv \left|W^{v,c}\left(q\right)\right|^2 \left|\Pi\left(q\right)\right|^2 \end{aligned} \tag{3.9}$$

In this model, $\Pi_{j=0,j'=1} = \Pi_{j=3,j'=2}$. The transition intensity is only related to the wavefunction coefficient C and the wavefunction phase mismatch between two neighboring chains.

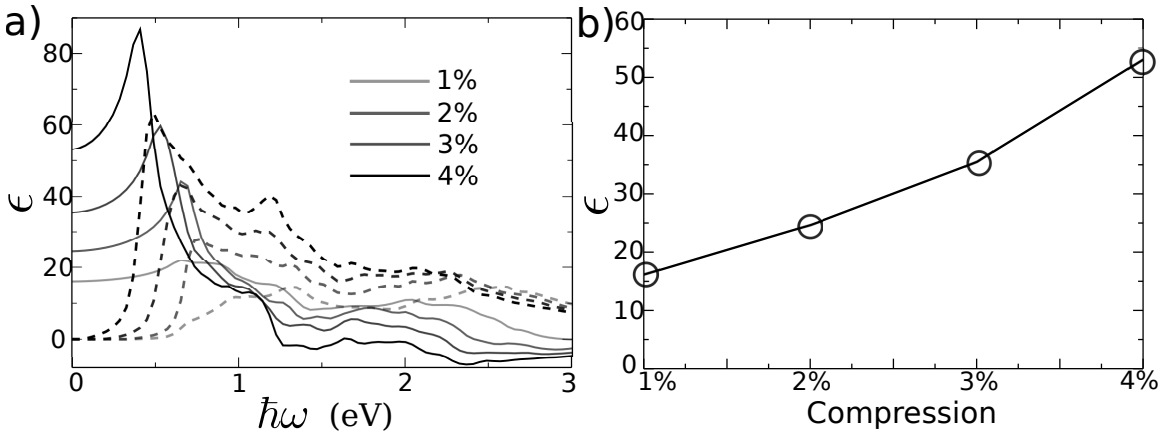

Figure 3.9: a) Optical dielectric functions under different compressions. b) The enhancement of the dielectric constants under different compressions.

Projected density of states

Fig.8 shows the projected density of states (PDOS) for the ES and CS. For the states near the band gap, p orbitals from Se and As are dominant to the valence bands and conduction bands. Hence, these two types of orbitals are crucial and considered in the tight-binding (TB) model.

Continuous Change of Optical Dielectric under Pressure

In the main text, 3% compression is shown illustrating the enhancement of the optical dielectric function. However, this compression induced enhancement is continuous under the pressure. Shown in Fig.9 is the optical dielectric functions under the different compression as 1%, 2%, 3% and 4% (corresponding to the stress 7.1, 14.5, 27.0 and 42.0 kbar, respectively). The dielectric constant is continuously enhanced under the compression as shown in Fig.9 b). Although the smaller band gaps due to the stronger compression contribute to the dielectric constants, the imaginary parts of the optical dielectrics are showing significant increase under the compressions.

XX and ZZ Components of the Optical Dielectric

$LiAsSe_2$ shows strong anisotropy of the optical dielectric function in the three direc-

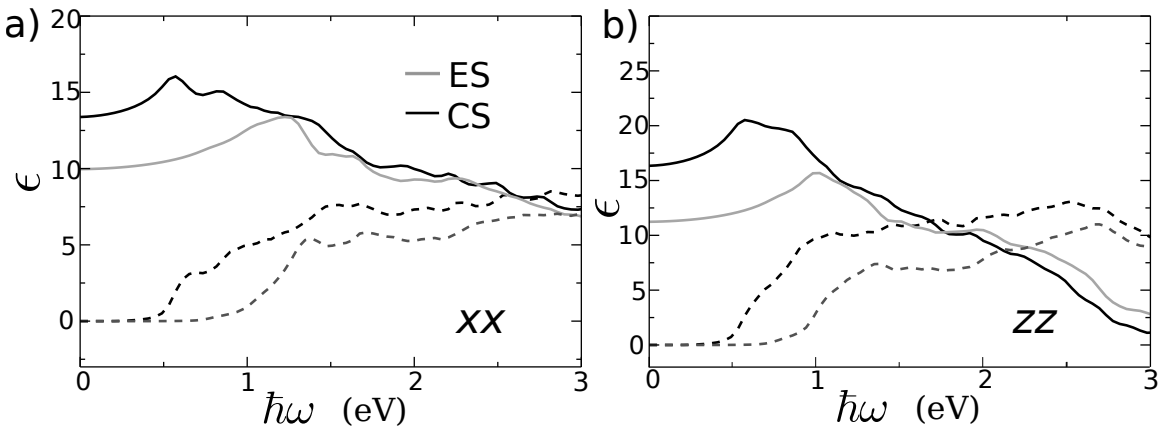

Figure 3.10: a) Optical dielectric functions in xx component of the ES and CS. b) Optical dielectric functions in zz component of the ES and CS.

tions owing to the different bonding properties along the three axis as shown in Fig.10. This anisotropy is significantly enhanced under the compression as yy (same to bb, used in the main text) component shows great increase. This further originates from the special electronic structure in the y direction (same to $\vec{b}$ direction). In particular, the polarization on $a-c$ plane distinguishes the bonding properties along $\vec{a}$ and $\vec{c}$ for the band edges. However, the enhancement of xx and zz are much less significant compared to the yy (same to bb) component shown in Fig.10 for the ES and CS. Here, we want to clarify that x, y and z are along the Cartesian axis. Thus, the x direction is the same to the $\vec{a}$ direction, however, z direction is slightly different from the $\vec{c}$ direction.

Chapter 4

First-principle Studies of Organometal Halide Perovskite

[1]

[1] F. Zheng, L. Z. Tan, S. Liu, and A. M. Rappe, *Nano. Lett.*, **15**, 7794 (2015)
F. Zheng, D. Saldana-Greco, S. Liu, and A. M. Rappe, *J. Phys. Chem. Lett.*, **6**, 4862 (2015)
F. zheng, S. Liu, L. Z. Tan, D. Egger, and A. M. Rappe, *in preparation* (2016)
S. Liu, F. Zheng, I. Grinberg, and A. M. Rappe, *J. Phys. Chem. Lett.*, **7**, 1460 (2016)
S. Liu, F. Zheng, N. Z. Koocher, H. Takenaka, F. Wang, and A. M. Rappe, *J. Phys. Chem. Lett.*, **6**, 693 (2015)

4.1 Introduction

The organometal halide perovskites (OMHPs) have attracted significant attention due to the rapid increase in their photovoltaic power conversion efficiency. In the past 3 years, the reported efficiency of OMHP-based solar cells has almost doubled from 9.7%[49] to over 20% [50, 51, 52], making OHMPs very promising for low-cost and high-efficiency photovoltaics. $CH_3NH_3PbI_3$ ($MAPbI_3$), and other closely-related hybrid perovskites such as Cl-alloyed and Br-alloyed $MAPbI_3$ ($MAPbI_{3-x}Cl_x$ and $MAPbI_{3-x}Br_x$), $(NH_2)_2CHPbI_3$ (formamidinium lead iodide, $FAPbI_3$), and Sn-alloyed $MAPbI_3$ ($MAPb_xSn_{1-x}I_3$), all display band gaps (1.1 to 2.1 eV) in the visible light region. Recently, the Ge-based OMHPs have been synthesized such as $CsGeI_3$, $MAGeI_3$ and $FAGeI_3$, which posses spontaneous polarization owing to the small size of Ge^{+2} [53]. They are all favorable for photovoltaic applications [54, 55, 56, 57, 58, 59, 1, 60, 61]. The class of materials also possesses strong light absorption, comparable to other classic semiconductors such as GaAs, InP, and CdTe[56, 4, 62, 63]. Also, these materials show relatively fast charge generation, high carrier mobility, and long carrier lifetime[64, 65, 66, 67, 68].

However, there are factors that hinder the commercialization of the OMHP solar cells. The stability (material degradation) challenge significantly reduces the robustness of OMHPs as the solar cells. Tremendous work has been done to understand the mechanism of the degradation.[69, 70, 71, 72, 73, 74, 75, 76]. Such degradation is further accelerated due to exposure to moisture light, or heat[77, 78, 79]. Besides the structure stability, the stability of the performance also limits the practical application of the OMHPs. In particular, the I-V hysterisis (PCE depends on operated voltage scanning direction and rate) still remains as a concern before market visibility[80, 81, 82, 83, 84]. Also, the PCE is strongly affected by fabrication method, age of the sample[85, 86, 82, 83, 87, 88], making the determination of the PCE very ambiguous. People have found that large grain of OMHPs

significantly reduces the I-V hysterisis, and gives rise to stable performance under operating conditions[89, 87, 90]. In addition, material design demonstrates to be a promising way to enhance both types of stability for the structure and performance[91]. For example, (MA,FA)Pb(I,Br)$_3$ generates ¿20% PCE with negligible I-V hysterisis effect, and high stability[92].

As a short summary, the advantages and disadvantages of the OMHPs are list below:

Advantages:

- High and fast growing PCE
- Cheap

The reason for its high PCE is mainly because:

- Appropriate band gaps
- Relatively high absorption
- Long carrier lifetime and diffusion length
- Low defect concentration

Disadvantages:

- Structure instability
- Strong I-V hysterisis effect
- Containing Pb (poison)

Beyond photovoltaic. In addition to solar cell applications, various OMHP materials are also proposed to use as thermoelectric devices due to their large Seebeck coefficient and low thermal conductivity[1, 93, 94, 95]. Furthermore, OMHPs recently are introduced as

nanolaser materials owing to the high fluorescence yields and wavelength tunability[96, 97, 98, 99]. Due to their appropriate band gaps, OMHPs can also be used as sensor [100, 101] and water-splitting cells [102].

Structure of OMHPs. OMHPs have the *perovskite-type* structure ABX_3, with Cs^{+1}, MA^{+1}, FA^{+1} ions are at the A site, and Pb^{+2}, Sn^{+2} are at the B site. Halide atoms including Cl, Br and I are at X site. At low temperature, most of the OMHPs favors the orthorhombic structure. Withe increasing the temperature, they transform into more symmetric structure (such as tetragonal). At high temperature, most of the OMHPs will show cubic structure. Taking the most typical $MAPbI_3$ as an example, the space group of this material is $Pbnm$ below 160 K [3, 1]. By increasing the temperature, it becomes $I4/mcm$ with in-plane octahedral rotation. Finally, above 330K [1], it shows cubic structure without any octahedral rotation. Shown in Fig. 4.1 is one typical primitive unit cell of $MAPbI_3$.

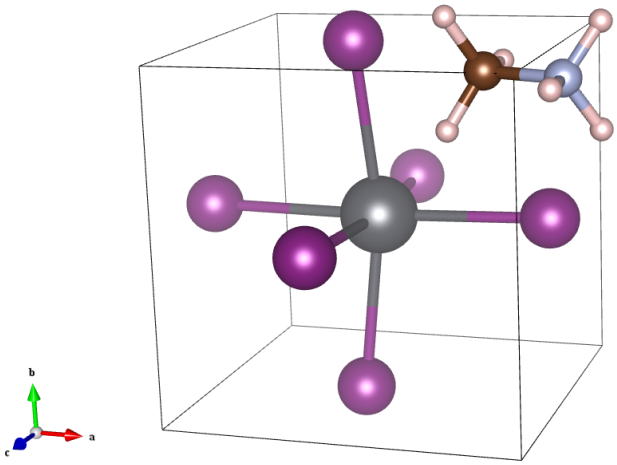

Figure 4.1: The primitive unit cell for $MAPbI_3$. Grey: Pb; Purple: I; Blue: N; Brown: C; Pink: H. The Pb is in the center of the iodine-cage. The molecule is at A site with +1 charge.

SOC effect in OMHPs. Due to the presence of heavy atoms, spin-orbit coupling (SOC) is thought to affect the electronic structure significantly [103, 104, 105]. When SOC is included, an angular momentum dependent term is added to the Hamiltonian. Fig. 4.2 a) shows the band structures without and with spin-orbit coupling. As seen in the figure, SOC reduces the band gap substantially at the Γ point. At this point, the GGA band gap with NSOC is close to the experimental value, as the DFT underestimation of band gap is largely canceled by the exclusion of SOC. This has been seen in GW and hybrid functional calculations [56, 62]. Our calculated electronic structure (NSOC) shows that the conduction band minimum (CBM) has mostly non-bonding Pb p_z orbital character slightly hybridized with I s; whereas the valence band maximum (VBM) is anti-bonding between I p and Pb s orbitals, as shown by the real space wavefunction plots in Fig. 4.2 b). The MA molecular electronic states are not directly involved in the states near the band gap, as confirmed by other first-principles calculations [76, 63].

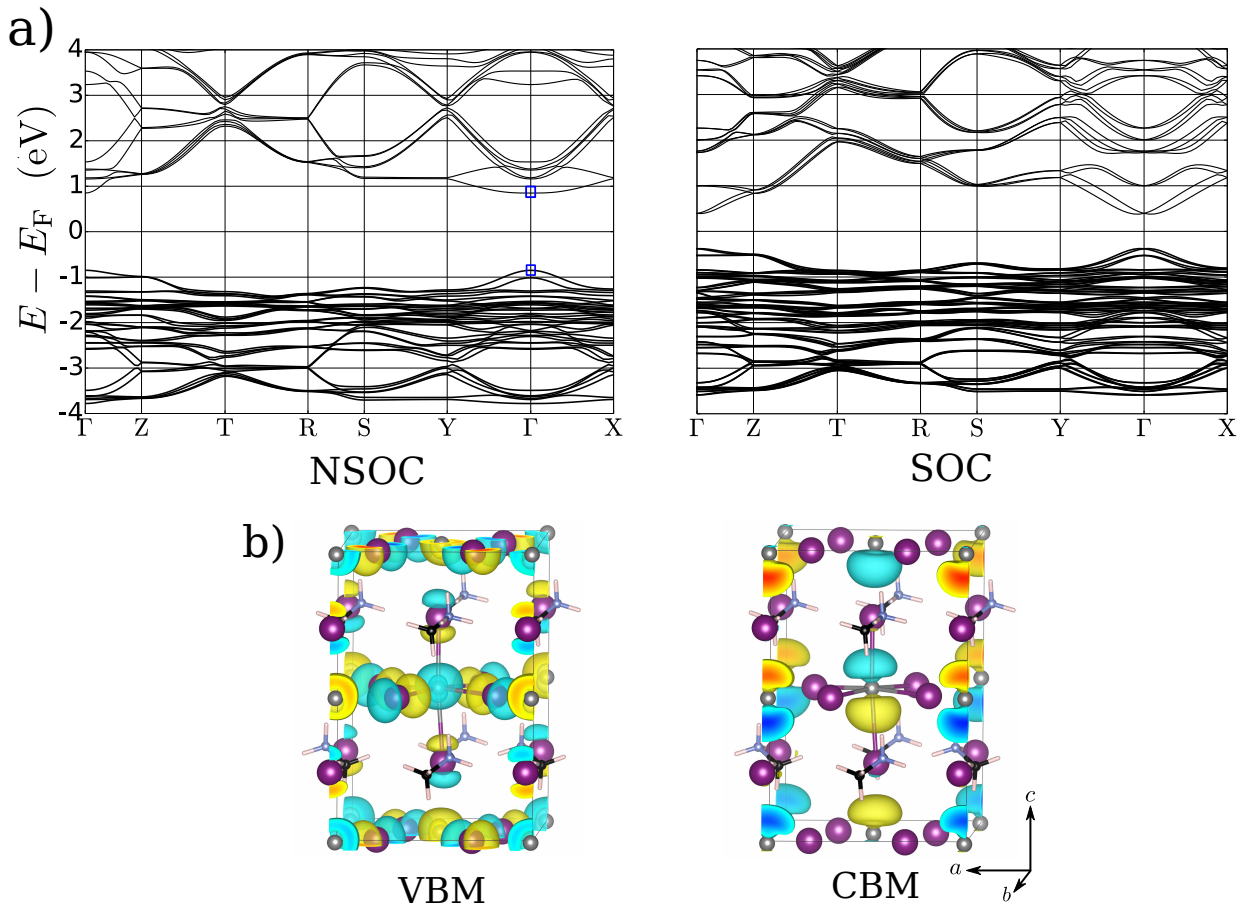

Figure 4.2: a) The band structures of MAPbI (M1) without and with spin-orbit coupling. Since the system lacks inversion symmetry, the SOC splits bands which are originally degenerate without SOC. b) The wavefunctions of the VBM and CBM at the Γ point without SOC (VBM and CBM states are indicated as blue square in the NSOC band structure).

4.2 Carrier Lifetime

4.2.1 Introduction

To understand the outstanding performance of the OMHPs as solar cells, the exceptionally long carrier lifetime and diffusion length have been observed in $MAPbI_3$ and $MAPbI_{3-x}Cl_x$, which makes these materials better solar cell candidates than other semiconductors with similar band gaps and absorption coefficients [66, 67, 68]. Intense research has been directed toward understanding and further enhancing the long carrier lifetime and diffusion length in OMHPs. Previous studies reported a relatively low defect concentration in $MAPbI_3$ [106, 107, 108, 109, 110], which reduces the scattering centers for nonradiative charge carrier recombination. Recently, it has been suggested that the spatial carrier segregation caused by disorder-induced localization[111] or domains acting as internal *p-n* junctions[112, 76, 18] may reduce the recombination rate. The presence of strong spin-orbit coupling (SOC) and bulk ferroelectricity in many of the 3D-Rashba OMHP materials have been studied extensively [113, 104, 114, 103, 115, 116, 117, 118, 119, 56, 120]. However, the direct role of spin and orbital degrees of freedom on photovoltaic applications are largely unexplored. In this work, we focus on an intrinsic mechanism for the enhancement of long carrier lifetime due to the Rashba splitting. Using first-principles calculations and effective models, we find that the Rashba splitting arising from SOC in locally polarized domains can result in spin-allowed and spin-forbidden recombination channels. The spin-forbidden recombination path has a significantly slower transition rate due to the mismatch of spin and momentum. The spin-allowed recombination path, though kinetically favorable, can be suppressed under appropriate spin texture due to the low population of free carriers induced by the fast carrier relaxation to the band edges. (Here, we consider electron-phonon scattering as the main relaxation mechanism.) Taking the electronic structures of $MAPbI_3$ under various distortions as examples, we show that the proposed

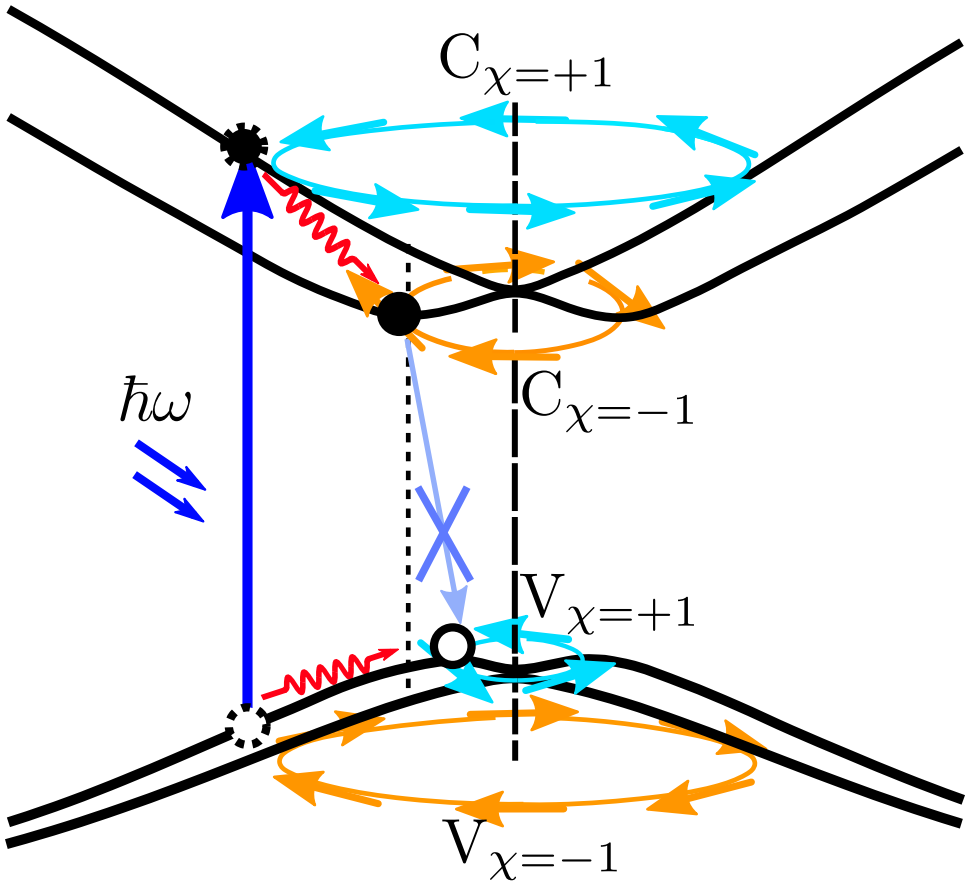

Figure 4.3: Diagram of Rashba bands and the electron transport path. The cyan and orange arrows indicate the directions of the spins. The spin texture χ indicates spin vortex direction, with its signs characterizing spin rotation in "clockwise" ($\chi = -1$) and "counterclockwise" ($\chi = +1$). After absorbing the photons, the excited electrons on conduction bands $C_{\chi=+1}$ and $C_{\chi=-1}$ will quickly relax to $C_{\chi=-1}$ band minimum ue to the inelastic phonon scattering. Similarly, the holes will quickly relax to the $V_{\chi=+1}$ band maximum. However, the radiative recombination of $C_{\chi=-1} \rightarrow V_{\chi=+1}$ is a spin-forbidden process due to the opposite spin states they have. Moreover, the minimum of $C_{\chi=-1}$ band and the maximum of $_{\chi=+1}$ band are located in different positions in the Brillouin Zone. his creates an indirect band gap for recombination, which further slows down the recombination process.

mechanism is possible under room temperature, and is potentially responsible for the long carrier lifetime in OMHPs. This spin-dependent recombination mechanism highlights the possibility of using 3D Rashba materials [121, 122, 123, 124] for efficient photovoltaic applications.

4.2.2 Results and Discussion

Fig. 4.3 illustrates the mechanism for enhancing the carrier lifetime in a generic 3D Rashba material. The strong spin-orbit coupling effect from heavy elements (e.g., Pb, Sn, I and Br) and inversion symmetry breaking owing to the polar distortion (e.g., aligned molecular dipoles in OMHPs) give rise to the Rashba effect, which lifts the two-fold degeneracy of bands near the band gap. This is distinct from the Dresselhaus effect, which happens in systems of different symmetry. Here, C_{4v} symmetry removes Dresselhaus splitting [125, 114]. Indeed, the spin structure of the Dresselhaus model is inconsistent with DFT calculations of $MAPbI_3$. [113] Near the band gap, the spin degeneracies of the conduction and valence bands are lifted, giving rise to "inner" and "outer" bands with opposite spin textures, characterizing spin rotation direction as "clockwise" ($\chi = -1$) and "counterclockwise" ($\chi = +1$) (Fig. 4.3). The photo excitation process creates free electrons and holes, which can quickly relax to band extrema in the presence of inelastic phonon scattering. When the spin textures of conduction band minimum (CBM) and valence band maximum (VBM) are opposite, the radiative recombination of $\mathrm{C}_{\chi=-1} \rightarrow \mathrm{V}_{\chi=+1}$ is a spin-forbidden transition due to the mismatch of spin states. This prevents rapid recombination as the photon-induced spin-flip is a slow process [126]. Moreover, the minimum of the $\mathrm{C}_{\chi=-1}$ band is slightly shifted compared to the maximum of the $\mathrm{V}_{\chi=+1}$ band (momentum mismatch). This creates an indirect band gap for recombination, which further slows down the recombination process due to the requirement of a phonon with the right momentum. This is also highlighted in Ref.[127], where the indirect band gap is created by the dynamic disorder of molecules. In the following, we use the terms favorable and unfavorable relative spin helicity to describe cases when the VBM and CBM have opposite and aligned spins, respectively.

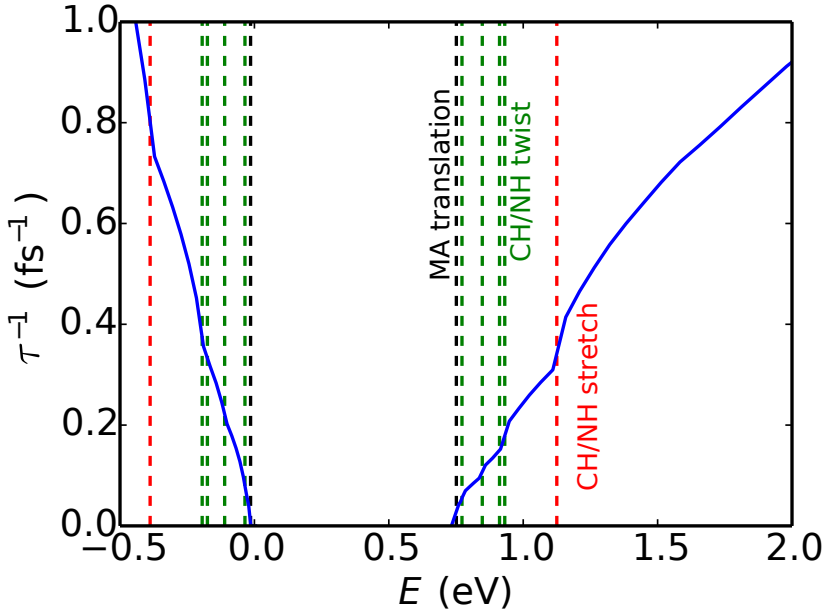

Figure 4.4: Dependence of phonon-induced relaxation rate on carrier energies (blue lines) for electrons (positive energies) and holes (negative energies). The VBM is located at $E = 0$ eV, and the CBM is located at $E = 0.73$ eV. The energies of phonon modes that contribute strongly to carrier relaxation are shown as dotted lines. The phonon modes listed in the graph have frequencies as 141.2 cm^{-1} (MA translation), 315.9 cm^{-1}, 924.3 cm^{-1}, 1441.5 cm^{-1}, 1598.3 cm^{-1} (MA twisting), and 3158.6 cm^{-1} (NH vibration), respectively. (See details in the Appendix)

The spin texture and carrier population of the CBM and VBM play key roles in enhancing carrier lifetime. Our first-principles density functional theory (DFT) calculations support the realization of this mechanism in OMHPs. Taking the pseudocubic phase $MAPbI_3$ as an example, we explore the carrier dynamics after the photoexcitation. The electron-phonon coupling plays a significant role for the relaxation of the excited carriers in OMHPs. [128] Using Fermi's golden rule, we calculate the inelastic phonon scattering rate (see Methods) shown in Fig. 4.4. The relaxation rate ($\approx 10^{15}\mathrm{s}^{-1}$) increases as a function of carrier energy. This is supported by the sharp jumps of the relaxation rate at frequencies corresponding to phonon modes (emission thresholds) derived mainly from the organic molecules, as shown in Fig. 4.4. We find that the organic molecule plays an important role for carrier relaxation. The modes that are responsible for these sharp jumps are identified as MA translation, CH/NH twisting, and CH/NH stretching. [129] In particular, the contribution of these modes are found in both VBs and CBs, indicating their equally important role in electrons and holes. The scattering magnitude differences of CBs and VBs are mainly from their density of states differences (Eq.4). Other modes with both MA and I vibrations also contribute to the carrier relaxations. But these modes have much lower frequencies, and the emission thresholds due to these modes occur much closer to the band edges.

Our calculations reveal that the phonon-induced carrier relaxation rate value is many orders of magnitude faster than the electron-hole recombination rate ($\approx 10^9\ \mathrm{s}^{-1}$)[130, 128]. Therefore, the carriers will rapidly thermalize and from a quasi-static equilibrium distribution near the CBM and VBM. In Rashba SOC bands, the special spin configuration always allows a carrier of a certain spin to relax to a lower energy state of the same spin via the emission of a finite-wavevector phonon. A sequence of such emission events results in the relaxation of carriers to band edges. In the ideal case of low temperatures and large Rashba

splitting, nearly all free carriers are located at the band extrema, and the effects of spin and momentum mismatch on the enhancement of the carrier lifetime will be the greatest. This effect is less strong at finite temperatures and small Rashba splitting because of the thermal occupation of $C_{\chi=1}$ and $V_{\chi=-1}$ bands, which opens spin-allowed recombination paths such as $C_{\chi=-1} \rightarrow V_{\chi=-1}$. In the case of favorable relative spin helicity, we investigate this temperature effect by examining the Rashba splitting using a Rashba Hamiltonian[131]:

$$H_R = \frac{\hbar^2 k^2}{2m} + \hbar v_R \hat{z} \times \vec{k} \cdot \vec{\sigma} \tag{4.1}$$

$$E_{k,s} = \frac{\hbar^2 (k_z^2 + k_\perp^2)}{2m} + s\hbar v_R k_\perp, \quad k_\perp = \sqrt{k_x^2 + k_y^2} \tag{4.2}$$

The parameters m and v_R represent the band mass and Rashba interaction respectively. By fitting m and v_R to DFT band structure of fully relaxed $MAPbI_3$ pseudocubic lattice, the band energies and spin configurations of the model agree with DFT calculated results. Furthermore, the tight-binding model introduced below and in the Supporting Information can be reduced to this Rashba Hamiltonian, demonstrating the role of Rashba SOC in $MAPbI_3$. We find that the conduction band Rashba splitting (0.108 eV) is much larger than the thermal energy scale, while the valence band Rashba splitting (0.016 eV) is comparable to the thermal energy scale. Since electronic correlations are not fully captured in DFT [61], these values are likely lower bounds of the true splitting. These relatively large Rashba splittings are likely to give rise to a significant enhancement in carrier lifetime even at room temperature.

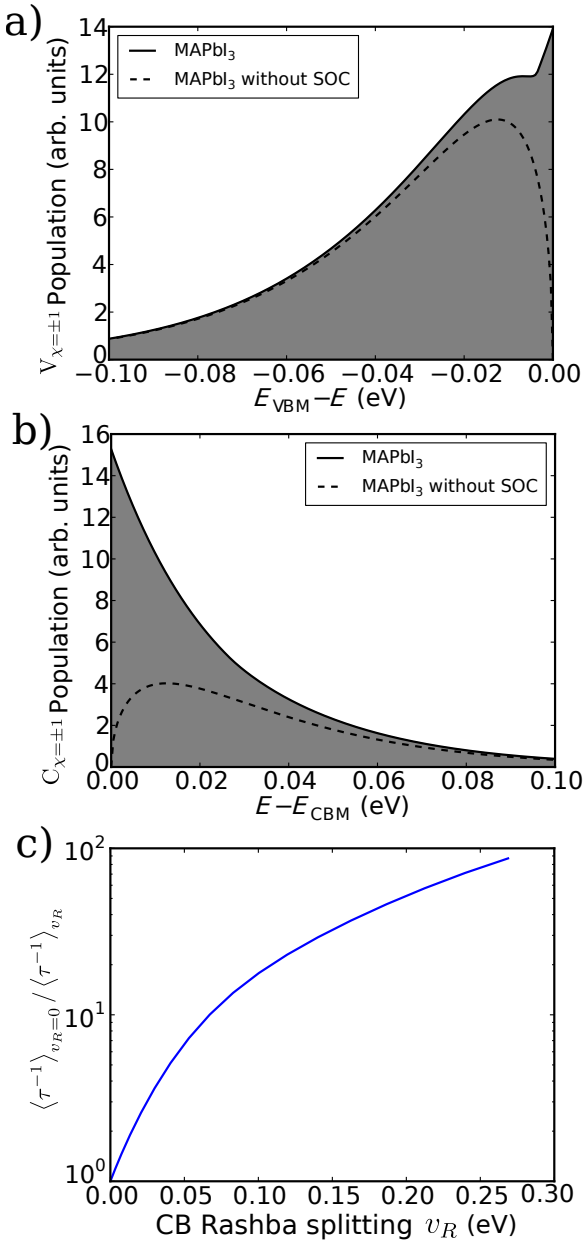

Figure 4.5: a) Population of carriers at T=298 K, calculated from the Fermi-Dirac distribution, for a) the top valence band and b) the bottom conduction band of $MAPbI_3$. Shown in dashed lines are the population of carriers in a model material with the same band masses as $MAPbI_3$, but with vanishing Rashba splitting. c) Unitless lifetime enhancement factor, as defined in the text, as a function of the conduction band Rashba splitting energy.

There is an additional factor, arising from the unique features of Rashba band structure, which promotes occupation of the band extrema. In contrast to the band extrema of ordinary parabolic bands in semiconductors which are points in momentum space, those of Rashba materials are one-dimensional rings (Fig. 4.3). This leads to an increase in the density of states at low energies, resulting in a population of carriers heavily skewed towards the band extrema (Fig. 4.5a and b) and consequently reduces the overall recombination rate due to the reasons of spin and momentum mismatch as discussed above. This increased density of states leads to a predominance of desirable spin carriers, even though the valence band splitting is comparable to the room temperature energy scale, protecting the long carrier lifetimes even at room temperature.

The magnitude of Rashba splitting depends on the amount of polar distortion and the strength of the SOC, both of which can be captured by the Rashba velocity parameter v_R. We calculate the averaged recombination rate

$$\langle \tau^{-1} \rangle = \sum_{\chi,\chi'} \frac{\int d^3k \, \tau^{-1}_{\chi,\chi'}(k) \, n^e_\chi(k) \, n^h_{\chi'}(k)}{\int d^3k \, n^e_\chi(k) \, n^h_{\chi'}(k)} \tag{4.3}$$

where $\tau^{-1}_{\chi,\chi'}(k) = B_{\chi,\chi'} n^e_\chi(k) n^h_{\chi'}(k)$ is the band- and momentum-resolved recombination rate. The spin-mismatch effect is captured by the rate constant $B_{\chi,\chi'}$, which is larger when χ and χ' have parallel spins than otherwise. Enhancement of density of states enters via the temperature dependent electron and hole occupation numbers $n^e(k)$ and $n^h(k)$, which tend to peak at different k points because of momentum mismatch. In order to quantify the effect of Rashba splitting on the recombination rate, we define the unitless lifetime enhancement factor as the ratio $\langle \tau^{-1} \rangle_{v_R=0} / \langle \tau^{-1} \rangle_{v_R}$, where $\langle \tau^{-1} \rangle_{v_R}$ is the average recombination rate when SOC is taken into account, and $\langle \tau^{-1} \rangle_{v_R=0}$ refers to a calculation where SOC is explicitly set to zero in the Rashba model (Fig. 4.5c). Upon tuning the Rashba splitting continuously in our model, we find that the lifetime enhancement factor increases

approximately exponentially with Rashba splitting - a consequence of the exponential behavior of carrier occupation numbers near the tail of the Fermi-Dirac distribution. Our model predicts that a Rashba splitting of 0.1 eV can give rise to an order of magnitude enhancement of carrier lifetime.

As we have seen, the favorable spin helicity of the VBM and the CBM enables the intrinsic enhancement of carrier lifetime, with the amount of enhancement depending on the magnitude of the Rashba splitting. The inversion symmetry-breaking distortions that influence relative spin helicity and splitting magnitude are therefore intimately related to the SOC enhancement of carrier lifetime. To reveal the relation, we start with a tight binding model of the inorganic PbI_3^- lattice (see Methods). The displacements of Pb atoms along the z direction give rise to effective hoppings between Pb s- and p-orbitals along the equatorial direction (Fig. 4.6a), which would vanish by symmetry in the absence of such displacements. Similarly, displacement of the apical I atoms along the z direction changes Pb–I bond lengths and effective hoppings along the apical direction (Fig. 4.6b). These modifications of hopping parameters create the effective inversion symmetry breaking electric fields described by $\hbar v_R$ in our low-energy theory model (Eq. 4.1). In this model, we find that the spin textures of the valence bands and conduction bands depend on the combination of Pb and I displacements. By shifting Pb and I atoms, we can control the spin textures of the valence and conduction bands, creating favorable and unfavorable relative spin helicities. As we now proceed to show, this picture is confirmed with DFT calculations.

We focus on two phases of $MAPbI_3$, pseudocubic phase (α phase) and tetragonal phase (β phase) [1]. The pseudocubic phase of $MAPbI_3$ has space group $P4mm$ with $a = b = 6.31$ Å and $c = 6.32$ Å. It does not have inversion symmetry, because of the permanent dipole moments of MA^+. It is suggested that the aligned molecular orientations in polar domain can drive Pb-I displacement giving rise to ferroelectric distortions [132]. The DFT fully relaxed pseudocubic structure at 0 K is monoclinic, with molecular dipole

pointing to the face center of PbI_3^- sublattice (see Supplementary Information). Since this 0 K structure is of limited use in the discussion of the PbI_3^- sublattice distortions at finite temperature, here we explore all the possible structures with Pb and apical I displacements along c direction while respecting the space group. Without distorting the PbI_3^- sublattice, the electronic effect of molecular permanent dipole moment to Rashba splitting is negligible. Thus, the molecules are aligned along c direction for simplicity. Shown in Fig. 4.6d are the DFT-calculated spin textures and averaged Rashba splittings at VBM and CBM respectively for a given pair of Pb and I displacements (see Methods). The areas outlined by the solid red lines indicate the structures with favorable relative spin helicities, which also have relatively large band splittings. We find that these structures have Pb and apical I displaced along opposite directions. This is consistent with typical ferroelectric distortions in inorganic ferroelectrics such as $BaTiO_3$ and $PbTiO_3$. It is noted that large apical I displacement tends to drive the system away from the region with favorable relative spin helicity to unfavorable spin helicity (Fig. 4.6d).

We further explore the relationship between relative spin helicity and local distortions in tetragonal $MAPbI_3$ [1], which is observed at room temperature. The space group of the tetragonal phase is identified as $I4cm$, allowing both ferroelectric distortion and PbI_6 octahedral rotation (Fig. 4.6e). Fig. 4.6f shows the spin textures and the averaged Rashba splitting for different Pb and I displacements in $I4cm$ space group. The tetragonal phase exhibits similar displacement-helicity relationship to the cubic phase, indicating that the Rashba splitting can also enhance the carrier lifetime in tetragonal phase.

Various experimental studies have demonstrated switchable ferroelectric domains (~100nm) and ferroelectricity at room temperature [133, 134, 89, 135]. Many theoretical studies also suggested the existence of local polar regions at room temperature [111, 76, 136, 137]. The atomic structures of these polar regions are still not clear. Energetically accessible structures at room temperature are highlighted by dashed red lines in Fig. 4.6d and f, which

cover a large region displaying favorable spin textures. Hence, our proposed mechanism can be realized in $MAPbI_3$ at room temperature, and provides a possible explanation of long carrier lifetime. Molecular dynamics and Monte-Carlo simulation [60, 138, 139] suggest that the molecule can rotate in a relatively short time scale, which may result in dynamic disorder although the issue of order and disorder is still an open question. However, our proposed mechanism is expected to be valid as long as the disorder correlation length is large enough to create local regions of finite Rashba splitting (see details in Supporting Information). In these local regions, we expect that our mechanism still contribute to the carrier lifetime enhancement. This is also supported by many studied listed above as they show large polarized domains to validate this mechanism. Moreover, recent studies of carrier dynamics under magnetic field illustrate the significance of spin in carrier recombinations [140, 141, 142].

Rashba SOC enhanced carrier lifetime highlights the potential of 3D Rashba materials [143] for photovoltaic applications. The ability to incorporate different organic molecules in OMHPs provides a robust avenue to design 3D Rashba materials. If changes are made to the dipole magnitude of organic molecules in halide perovskite, the spin helicities and band splittings are likely to be affected via the Pb and I displacements as discussed above. Conventional experimental techniques of controlling bulk polarization (e.g, epitaxial strain) can also be applied to optimize power conversion efficiency.

In summary, we have proposed an intrinsic mechanism for enhancing carrier lifetime in 3D Rashba materials. In the case of OMHPs, such mechanism can be realized by the joint action of molecules (electron-phonon coupling) and PbI_3^- sublattices (giving rise to spin-orbit coupling). The photoexcited carriers quickly relax to band edges due to the electron-phonon coupling. When the spin textures for CBM and VBM are opposite, the Rashba splitting of bands close to the band gap results in spin-allowed and spin-forbidden recombination paths. The spin-forbidden recombination path has slow transition rate due

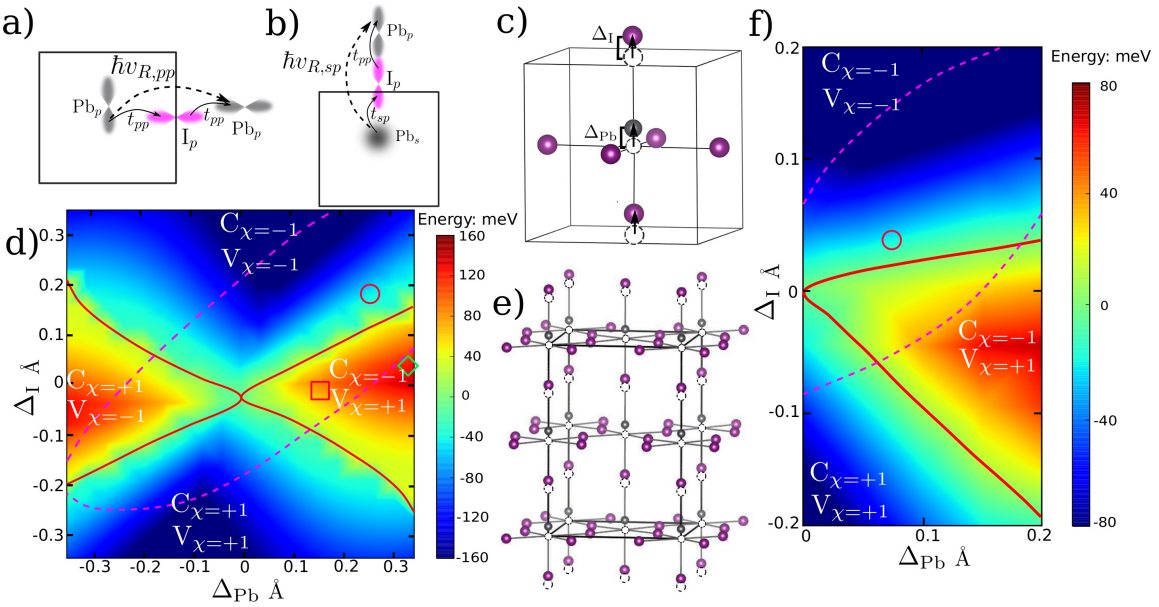

Figure 4.6: a) and b) Hopping schemes illustrate the effective electric field $\hbar v_{R,sp}$ and $\hbar v_{R,pp}$ created by vertical hopping and horizontal hopping respectively for a range of Pb and I displacements. These two factors caused by different Pb and I displacements controls spin textures of CBM and VBM differently, giving rise to different spin helicities. c) Schematic diagram showing Pb and I displacement in pseudocubic $MAPbI_3$. Pb: Silver. I: Indigo. Broken circles are original high-symmetry positions. Molecules are not shown here. The red square/green diamond indicate the displacements of Ti and apical O of $BaTiO_3$/$PbTiO_3$ for comparison [5, 6]. The red circle marks the distortions with the lowest total energy. d) Phase diagram of splitting energy and spin texture for structures with different Pb and apical I displacement in pseudocubic $MAPbI_3$ calculated from DFT. The color is the minimum value between the averaged splitting energy of two Rashba conduction bands and two valence bands (see Methods). The spin texture phase boundaries are indicated by the solid red lines. When the structure transforms from a favorable spin texture region to an unfavorable spin texture region, the two Rashba valence bands or conduction bands exchange, creating negative splitting energy. The dashed lines indicate the areas with energy cost less than 25 meV (under room temperature fluctuation) to distort Pb and I. e) Schematic diagram showing Pb and I displacement in tetragonal $MAPbI_3$. f) Similar to d, phase diagram of splitting energy and spin texture for structures with different Pb and apical I displacement in tetragonal $MAPbI_3$ calculated from DFT. The red circle marks the distortions with the lowest total energy.

to mismatch of spin and momentum. The spin-allowed recombination path, though kinetically favorable, will only influence a smaller amount of carriers. In order to achieve this favorable spin helicity, we explore different Pb and I displacement giving rise to different spin textures. A tight binding model is developed to explain this spin-displacement relation. This mechanism allows OMHPs to behave like direct-gap semiconductors upon photoexcitation, and like indirect-gap semiconductors during radiative recombination, simultaneously harnessing the large carrier densities of the former and the long lifetimes of the latter. The mechanism we propose highlights the importance of the Rashba effect and structural distortion for achieving long carrier lifetime and consequently long diffusion length in organometal halide perovskites.

4.2.3 Appendix

DFT and Electron-phonon coupling The plane-wave DFT package QUANTUM-ESPRESSO [43] with the Perdew-Burke-Ernzerhof [144] functional (PBE) is used to perform electronic structure and electron-phonon coupling calculation. Norm-conserving, designed nonlocal pseudopotentials were generated with the OPIUM package [44, 45]. The following orbitals are pseudized and considered as valence electrons: Pb: $5d$, $6s$, $6p$; I: $4d$, $5s$, $5p$; C: $2s$, $2p$; N: $2s$, $2p$; H: $1s$. The planewave cutoff is 50 Ryd to get converged charge density. The k points are chosen as $8 \times 8 \times 8$ Monkhorst-Pack grid for pseudocubic structure and $6 \times 6 \times 4$ for tetragonal structure [132]. As also shown in other work, the band gap is underestimated with PBE+SOC [104, 103, 116, 117, 118, 119, 56]. We calculate the inelastic phonon scattering rate for electrons and holes using Fermi's golden rule (with SOC included) [145, 128]:

$$\tau^{(ph)\,-1}_{k,n\to n'} = \hbar^{-1}\frac{V}{(2\pi)^3}\sum_{\nu}\int d^3k' |g^{n,n'}_{\nu,k,k'}|^2 \delta(E_{k,n} - E_{k',n'} - \hbar\omega_{\nu}) \tag{4.4}$$

where k and n are the wavevector and band index respectively, ν denotes the phonon mode, $E_{k,n}$ are electronic band energies and V is the volume of the unit cell. The phonon frequencies ω_ν and electron-phonon matrix elements $g^{n,n'}_{\nu,k,k'}$ are obtained from density functional perturbation theory (DFPT)[27]. Further details are included in Supporting Information.

Lifetime enhancement factor The rate constant $B_{\chi,\chi'}$ in Eq. 4.3 of spin-allowed ($\chi = \chi' = \pm 1$) and spin-forbidden ($\chi \neq \chi'$) transitions are obtained from averaged DFT calculated oscillator strength over the k points near band edges. For example, $B_{1,1} \approx 3.7 B_{1,-1}$. Although the calculation with PBE+SOC underestimated the band gap, in this case, only the ratio of spin-allowed and spin-forbidden transitions matters. In this work, the oscillator strength is used to show transition probability. Because spin-allowed and spin-forbidden transitions occur at similar energies (around the magnitude of band gap), the ratio of oscillator strength between these two types of transitions are not affected significantly.

Tight-binding model The tight-binding model is based on PbI_3^- structure. Pb $6s$, Pb $6p$ and the I $5p$ orbitals are included in this model with spin degree of freedom. The tight-binding Hamiltonian is:

$$H_{\mathrm{TB}} = H_{\mathrm{hop}} + H_{\mathrm{SOC}} \tag{4.5}$$

where H_{hop} considers the nearest neighbor hopping between two orbitals, described by t_{sp}, $t_{pp\sigma}$ and $t_{pp\pi}$ for s–p σ hopping, p–p σ hopping and p–p π hopping respectively. H_{SOC} is the on-site SOC term defined as $\lambda_{\mathrm{Rashba}} \mathbf{L} \cdot \mathbf{S}$. Hopping parameters and $\lambda_{\mathrm{Rashba}}$ are fitted to DFT band structures of pseudocubic $MAPbI_3$ with experimental lattice constants. We reduce our tight-binding Hamiltonian into the Rashba effective model (Eq. 4.1) in two steps, following the procedure outlined in [113]. First, the I p orbitals are removed by projecting H_{TB} to the subspace of Pb orbitals:

$$H_{\mathrm{Pb}} = \mathcal{P} H_{\mathrm{TB}} \mathcal{P} + \mathcal{P} H_{\mathrm{TB}} \mathcal{Q} \frac{1}{E - \mathcal{Q} H_{\mathrm{TB}} \mathcal{Q}} \mathcal{Q} H_{\mathrm{TB}} \mathcal{P} \tag{4.6}$$

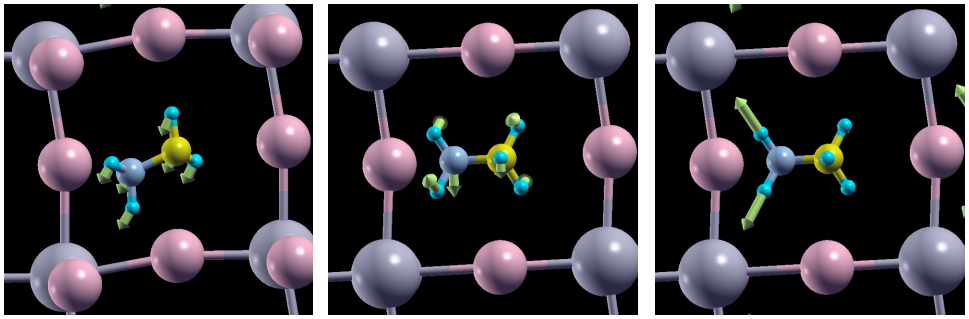

Figure 4.7: Phonon modes corresponding to sharp emission thresholds seen in Fig. 2 of main text. (a) MA translation, (b) CH/NH twisting, (C) NH vibration. There frequencies are 141.2 cm^{-1}, 315.9 cm^{-1} and 3158.6 cm^{-1}, respectively. Pb: grey; I: pink; C: yellow; N: blue; H: cyan.

where $\mathcal{P}$ and $\mathcal{Q}$ are projection operators to the Pb and I subspaces respectively. This results in an effective Hamiltonian H_{Pb} containing inversion symmetry breaking terms which modify the effective hopping between Pb orbitals [113]. Next, H_{Pb} is reduced to H_R using a similar projection to the CBM and VBM. (See details in Ref. [146])

Rashba splitting energy phase diagram For both pseudocubic and tetragonal phases of $MAPbI_3$, the apical I and Pb atoms are displaced while respecting the space group identified from experiments. These displacements generate the 2D map (Fig. 4.6) and each point in this 2D map corresponds to one structure with the specific pair of Pb and I displacements. The Rashba splitting energy is defined as $|\Delta E^R| = \min[\langle E_{\mathrm{C},s=\mathrm{CBM}+1} - E_{\mathrm{C},s=\mathrm{CBM}} \rangle , \langle E_{\mathrm{V},s=\mathrm{VBM}} - E_{\mathrm{V},s=\mathrm{VBM}-1} \rangle]$. Here, the sign of ΔE^R is indicated as $+1$ for favorable spin helicity, and -1 for unfavorable spin helicity. "$\langle\ \rangle$" indicates the average over k points near CBM or VBM.

Phonon modes of $MAPbI_3$. Pseudocubic $MAPbI_3$ structure is used to compute electron-phonon (e-ph) coupling. The structure of $MAPbI_3$ is fully relaxed using the force threshold of 2.5×10^{-5} eV/Å with and without SOC. The relaxed structure is $a = 6.412$ Å, $b = 6.346$ Å, $c = 6.470$ Å, $\alpha = 90.0$ Å, $\beta = 88.8$ Å and $\gamma = 90.0$ Å. The volume is $V = 263.220$ Å^3, consistent with other computational work [147]. The GGA functional is well known to overestimate experimental volumes [1, 2, 3].

As illustrated in other studies, imaginary phonons at Γ point are obtained [128], which may come from the rotational degree of freedom. The contribution of the imaginary mode can only increase the total phonon relaxation rate, which does not affect our assumption that the phonon relaxation rate is orders of magnitude faster than radiative recombination. Because the carriers (electrons and holes) can be relaxed to band edges with fast scattering rate by other phonon modes (indicated in Fig.2 and Fig. S 4.7). SOC is found to have negligible effect to the structural relaxations [132, 56, 103, 147] as well as phonon frequencies. The phonon frequencies ω_ν and electron-phonon matrix element g in this work are obtained from density functional perturbation theory (DFPT) with SOC included.

Since the purpose of e-ph calculation is to show the high phonon scattering rate, it is not necessary to perform the expensive DFPT calculation on massive k and q points sampled in the entire Brillouin Zone to obtain the accurate matrix elements. In this work, three q points are included to demonstrate the fast phonon scattering rate: $\vec{q} = (0.0, 0.0, 0.0)$ (Γ phonon scattering, in cartesian coordinate), $\vec{q} = (0.0, 0.01, 0.0)$ (small wavevector phonon scattering) and $\vec{q} = (0.0, 0.04, 0.0)$ (large wavevector phonon scattering). e-ph coupling of all these q points show similar phonon scattering rate on the order of 1×10^{15} s^{-1}, which is several orders faster than the spontaneous recombination rate ($\lesssim 1 \times 10^{9}$ s^{-1}).

Besides the three types of phonon modes mentioned in Fig.2 and Fig. S1, other phonon modes with relatively small frequencies also contribute to the excited carrier relaxation to the band edges. For completeness, in Fig. S2, the other five modes with large e-ph coupling

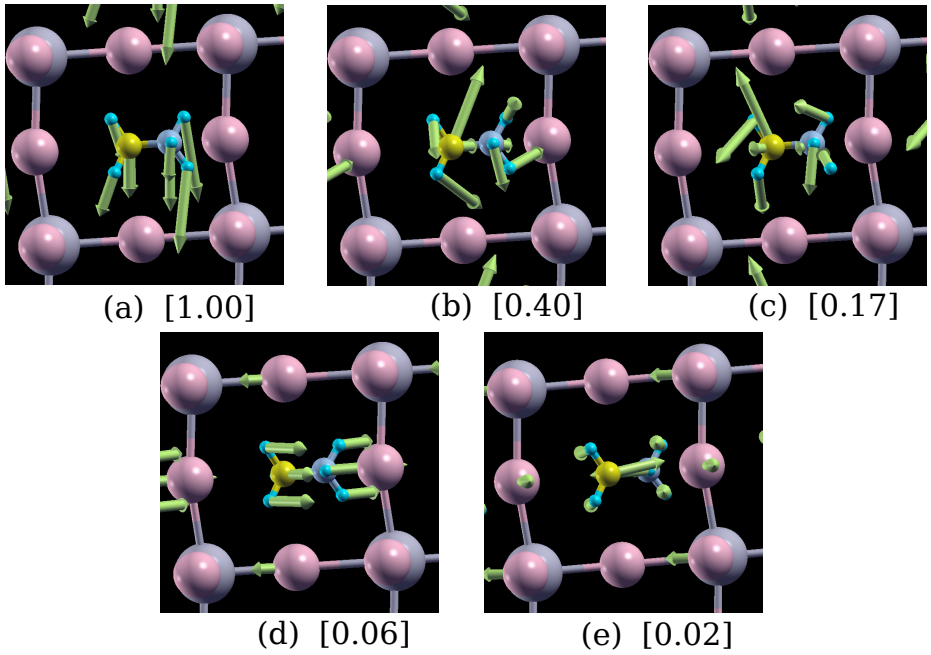

Figure 4.8: Phonon modes with large e-ph coupling strength. The number in the square brackets indicate the e-ph coupling strength ($|g|^2$) compared to the largest mode (a), which is set to 1. Their frequencies are 139.5 cm^{-1}, 121.1 cm^{-1}, 97.3 cm^{-1}, 71.3 cm^{-1} and 40.9 cm^{-1}, respectively. Pb: grey; I: pink; C: yellow; N: blue; H: cyan.

strength are also shown. However, owing to their low frequencies, the sharp jumps induced by these modes occur much closer to the band edges. Due to the low density of states near the band edges, these modes do not show abrupt jumps in the relaxation rate graph. As shown in Fig. S1 and Fig. S2, all the modes contributing large e-ph coupling strength and fast scattering rate mainly belong to the molecules. Fig. S2 d and e show some iodine movements, however, their e-ph coupling strengths are also reduced.

4.3 Large-scale Tight-binding modeling

4.3.1 Introduction

OMHPs are known to exhibit the spatial and temporal structural disorder [2, 148, 149, 60]. Tremendous work has been devoted to understand the way how the structure distorts. In particular, in the most studied $MAPbI_3$, the A site is occupied by a molecule with permanent dipole moment, which drives the PbI_3 sublattice distortions (described in Chapter 3). Intense research, both experimental and theoretical[2, 139, 150, 151, 127, 149], have been directed to study the behavior of the molecules, which is believed to be the origin of the structural distortion due to their dynamically changing orientations. Recently, the experiments with low-frequency Raman show the similar spectrum pattern in $MAPbBr_3$ and $CsPbBr_3$, indicating the intrinsic feature of the structural disorder, independent of A site occupations[152]. While the role of A site to the structure disorder is elusive, the presence of structural distortion is affirmative, and its effect to the electronic properties needs to be considered.

The structural disorder may contribute to the long carrier lifetime. Previous studies indicate that the PbI_3 sublattice driven by the A site molecules may form local polar domains [76, 112, 18]. The domain walls in between can help the carrier separation and diffusion due to the high conductivity. This idea is further shown in Ref. [111], where a large supercell is computed *ab initio* with the CBM and VBM charge densities localized in different regions in real space. Furthermore, as illustrated in the above section, the structural distortion of the A site orientation can lead to the CBM and VBM separation in momentum space [153, 91, 113, 104, 114, 103, 115], i.e. creating the indirect recombination, and enhancing the long carrier lifetime. The above *ab initio* work mostly were done at 0 K, where the temperature effect to the structural disorder is implicit. To directly include the effect of the temperature directly, people have done the *ab initio* molecular dynamics

simulations to study the dynamics of the geometric and electronic structures. In particularly, it is found that the band gap and the band edge states with the fluctuation of 0.1~0.2 eV were observed [154, 155, 60]. In these simulated systems, the size of the system is still a few unit cells owing to the high cost of *ab initio* calculations, and some artifacts may be introduced due to the finite size. Hence, a large enough dynamical system is needed to eliminate this problem. TB method has been proven to be an effective yet accurate way to compute the electronic structure of large systems [156, 157], particularly in the energy range interested. In this work, by combining the simulation of the classical MD of a large system of $MAPbI_3$ at finite temperature, and the electronic structure calculation via solving the TB Hamiltonian, we show the role of the structural disorder to the electronic wavefunctions directly. Our calculation demonstrates the enhancement of carrier lifetime by 20% due to the disorder. We also observe a very small magnitude of the band gap fluctuation, showing the significant finite-size effect to the band gaps.

4.3.2 Results and Discussion

As mentioned in the last section, we developed a tight-binding (TB) model to describe the band edges of $MAPbI_3$. In addition to the TB model in Ref. [113], where only Pb orbitals are considered, here, the Pb s and p, and I p orbitals are included, with the hopping strength describing the nearest Pb-I hopping. Thus, the TB Hamiltonian is written as:

$$\mathcal{H} = \mathcal{H}_{\text{onsite}} + \mathcal{H}_{\text{hop}} + \mathcal{H}_{\text{SOC}} \tag{4.7}$$

$$H(\mathbf{k}) = \sum_{i,\alpha} \left(\epsilon_i c^\dagger_{i\alpha,\mathbf{k}} c_{i\alpha,\mathbf{k}} \right) + \sum_{\alpha} \sum_{\langle i,j \rangle} \left(t_{ij} c^\dagger_{i\alpha,\mathbf{k}} c_{j\alpha,\mathbf{k}} + \text{c.c.} \right) + \sum_{i,\alpha\beta} \left(\lambda_i c^\dagger_{i\alpha,\mathbf{k}} c_{j\beta,\mathbf{k}} + \text{c.c.} \right) \tag{4.8}$$

where i, j are the index for atomic orbitals, α, β are spins, t is the hopping strength between

the orbitals, and ϵ_i is the onsite energy for orbital i. This TB model does not contain the molecular orbitals explicitly owing to their high energies far from the band edges of $MAPbI_3$ [132]. In this model, we consider three types of bonding (and hopping) between Pb and I: s-p σ bond, p-p σ bond, and p-p π bond. Both onsite energy and hopping strength can be fitted from DFT calculated band structures. Moreover, because of the significant role of SOC mentioned before, both spins (spin up and spin down) are included for each orbital. Their interactions are described by the onsite atomic SOC matrix [113] with the λ_i controlling the SOC strength for the orbital i. The structural distortion is essential, and its effect to the TB mode is reflected by the distortion of the hopping strength as:

$$t_{\text{distort}} = t_{\text{undistort}} \mathrm{e}^{\alpha(d_{\text{distort}} - d_{\text{undistort}})} \tag{4.9}$$

$(d_{\text{distort}} - d_{\text{undistort}})$ is the bond length difference before and after distortion. α ($\alpha < 0$) associated with different bond type (σ and π bonds) is also fitted from various DFT structures.

In order to fit the TB parameters, our DFT calculation is performed on a single unit cell $MAPbI_3$ lattice (see the Appendix for details). With the charge density obtained from self-consistent calculation, we perform a non-self-consistent calculation on the denser k-point grid as $10\times10\times10$, and fit the TB model to this band structure with the least-square method. Since the TB mode of one unit cell has 26 bands, we fit to the DFT band structure with 20 valence bands and 6 conduction bands. In this case, all the parameters including onsite energy, hopping strength and SOC coupling strength are varied to fit. Shown in Fig. 4.9 are the DFT and TB calculated band structure comparison for the high symmetric $MAPbI_3$ single unit cell structure and the distorted structure by manually moving the Pb and I atoms away the high symmetric positions. Both structures show good agreement between the DFT and the TB band structures, in particular, the TB calculation can reproduce the

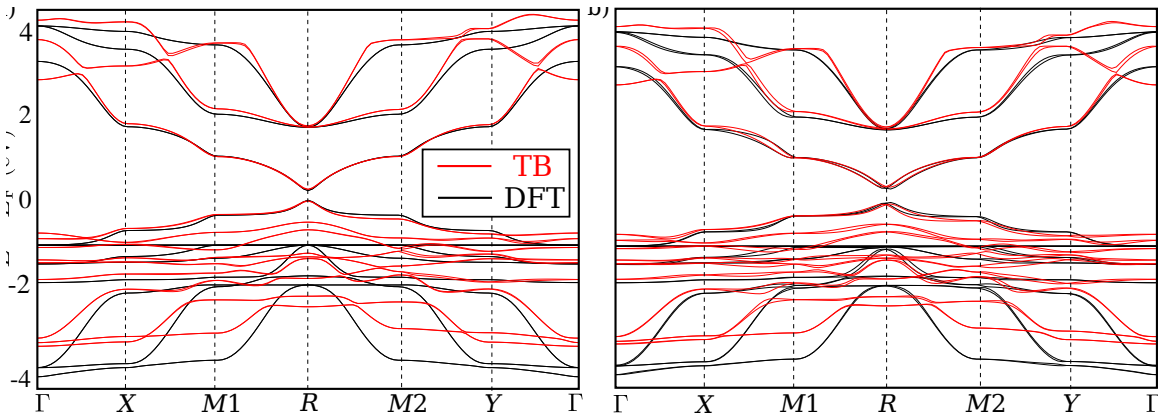

Figure 4.9: a) The DFT and fitted TB band structures for the primitive $MAPbI_3$ high symmetric unit cell (with Pb in the center of cube and I in the center of cubic faces). b) The DFT and the fitted TB band structures for the distorted structure of $MAPbI_3$ (all atoms are randomly displaced from the high symmetric structure with less than 0.12 Angstrom).

band gap, and match the band edge states with the DFT very well. Furthermore, the orbital characters calculated from the TB are the same to the DFT results [132], with CBM mainly Pb p and VBM Here, for the bands near the bottom and the top, relatively large deviations are shown, which is mainly due to the simplicity of the TB model with the nearest hopping considered, and the mixed molecular orbitals in DFT, respectively.

To further validate our TB model, we use the TB model on a set of $\sqrt{2} \times \sqrt{2} \times 2$ supercell structures extracted from an *ab initio* MD simulation to compared with their DFT calculations. Shown in Fig. 4.10 is the band structures calculated by the TB and DFT. The TB gives the very accurate band gap with less than 0.02 eV error. In addition, it can reproduce the band edge states very well, demonstrating the correctness of our TB model. Furthermore, we calculate the band gaps of the TB and DFT as displayed in Fig. 4.10, which shows good agreement and enables the using of TB for the much larger system.

We perform the classical MD simulation of the $20\times20\times20$ supercell of $MAPbI_3$ at room temperature (300K) and generate the trajectories (see the Appendix for details). The TB Hamiltonian can be built with the input of the MD structures. The most challenge step is to solve the eigenvalues and eigenvectors of the large Hamiltonian with the size around 0.2 Million $\times$ 0.2 Million. Here, we use the so called Implicitly Restarted Arnoldi Method to diagonalize the sparse Hermitian matrix. This method is implemented in the MPI enabled parallel version of ARPACK library as PARPACK [158, 159]. Reverse communication interface is one of the most special technique in this library. Using this method, it is not necessary to store the large size of the Hamiltonian in the memory, instead, the only needed action is to design the matrix vector product principle. The PARPACK library is also capable to print out the eigenvectors for the requested eigenvalues. With all these features, we can solve the TB model efficiently yet accurately.

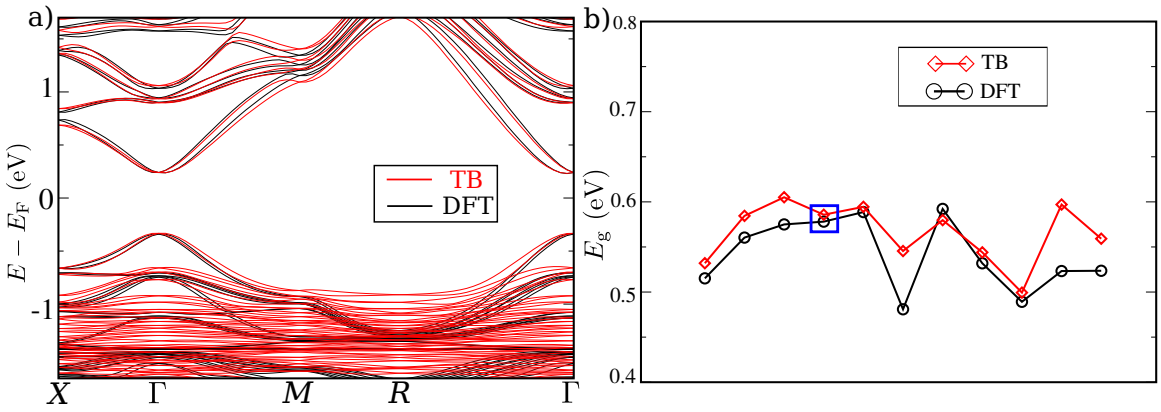

Figure 4.10: a) Band structures calculated from the DFT and TB. b) The band gaps obtained from the DFT and TB for the structures extracted from ab initio MD simulations. The structure with blue square is used for band structure calculation shown in a).

This large supercell has the band gap at Γ point. Shown in Fig. 4.11 a is the band gap of the 21 structures extracted from the MD trajectory. From the Fig. 4.9 where the DFT band structure is shown, the DFT band gap with SOC underestimates the experimental measurement by around 1 eV, which is well known issue for PBE exchange-correlation functional. However, the band gap along this trajectory varies with only around 0.01 eV magnitude, which is much less than the aforementioned 0.1~0.2 eV fluctuation observed in the *ab initio* MD simulations. This shows that the band gap fluctuation depends on the size of the system under the calculation. To further demonstrate this, we slice this large system to small sub-systems (shown in Fig. 4.11 b), and calculate the band gaps for the sub-systems. These values are also plotted in the Fig. 4.11 a. Apparently, as shown from this graph, when the system becomes smaller, it tends to have large band gap variations. In our case, the $4\times4\times4$ system has the band gap fluctuation up to 0.2 eV, while this fluctuation reduces to 0.05 eV when the size of the system increases to $10\times10\times10$. Therefore, we believe that the previous observed large band fluctuation up to 0.2 eV is more likely to be the artifact due to the limited size of the system used in the simulation. In the experiments, people can observe the ferroelectric domain with the size around 100 nm [133, 134, 89, 135]. The domain and the domain wall indeed may affect the band gap as demonstrated in Ref. [18]. By increasing the size of the system to this further, the band gap should be constant without explicit change. This stable band gap also explains the sharp absorption edge and the small Urbach tail. While the overall band gap varies negligibly, this material shows strong local fluctuations. This is associated with the relatively weak Pb-I bonding strength yet sensitive electronic structure change, which is further owing to the intrinsic dynamic disorder of this material [152].

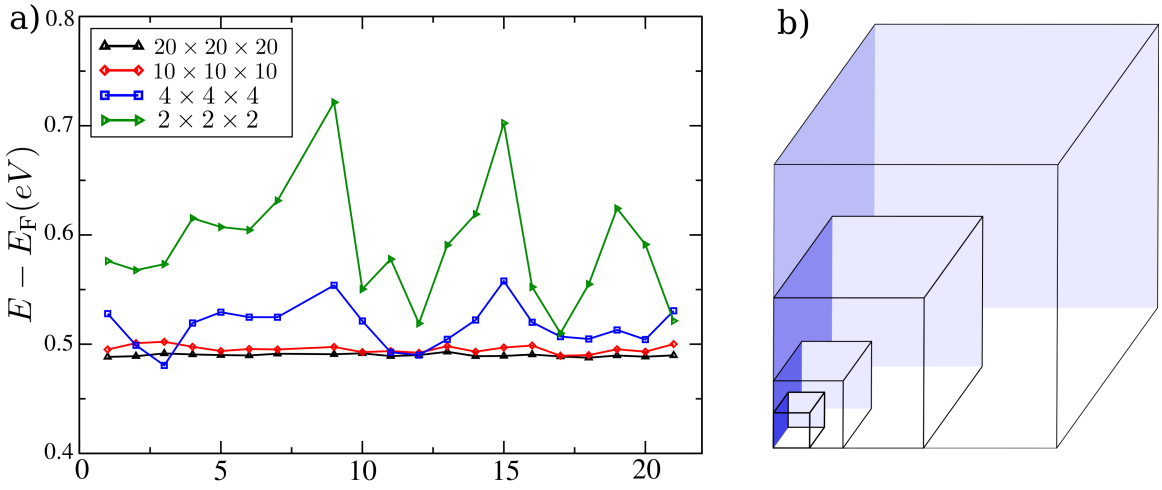

Figure 4.11: a) The band gap evolution of the classical MD trajectory. Here, we calculate the electronic structure of 21 structures of this trajectory. Besides the $20 \times 20 \times 20$ supercell, the band gaps of the sliced $10 \times 10 \times 10$, $4 \times 4 \times 4$, and $2 \times 2 \times 2$ are also shown. b) It shows the diagram of slicing the $20 \times 20 \times 20$ supercell to obtain smaller supercells.

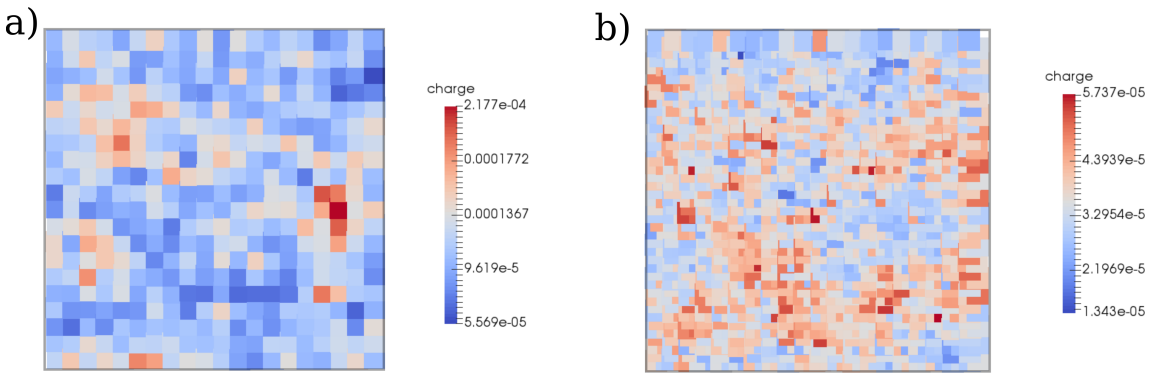

Figure 4.12: a) The CBM charge localization in the real space. Here, only one slice of the supercell is shown for visibility. Each tile represents one Pb atom. b) The VBM charge localization in the real space. Each tile represents one I atom.

The strong local structural distortion can further affect the wavefunction and the charge density. In Ref. [111] where molecular orientations are randomly distributed, both CBM and VBM show charge localization within nanoscale regions, and this effect is highlighted in a larger system. Our TB calculation also shows similar results. But in our calculation, instead of using randomized molecular orientation, the MD trajectory is used, making the picture obtained more realistic. In Fig. 4.12, the charge density of the CBM and VBM at Γ point are displayed, where only one slice of supercells ($20\times20\times1$) is shown for visibility with each tile representing Pb (CBM) or I (VBM) atom. Apparently, both CBM and VBM shows uneven spatial distributions. More importantly, the most localized positions of the CBM and VBM in the real space do not overlap, which could lead to slow recombination rate. The dynamic random orientation of the molecules can create dynamic indirect band gap in the momentum space owing to the strain applied by the molecules [127]. In our simulations, the large system used eliminates such strain and annihilates the k-space indirect band gap, but still creates "spatial" indirect band gap owing to the disordered molecular orientation and the PbI_3 sublattice distortions.

In order to quantify how the spatial localization of the charge density affect the carrier lifetime, we calculate the recombination rate using the TB wavefunctions. Based on the Fermi's golden rule, the recombination rate is expressed as $\tau^{-1} \propto \sum_{c,v} \int_{BZ} d\mathbf{k} \left|\langle c, \mathbf{k}| \, p_i \, |v, \mathbf{k}\rangle\right|^2 \delta(\omega_{c,\mathbf{k}} - \omega_{v,\mathbf{k}} - \omega)$, where τ is the lifetime, c and v indicate the conduction and valence bands with their energy ω_c and ω_v, and ω is the light frequency. Due to the low intensity of the sunlight, the excited carriers will mainly recombine at Γ point where the band gap is present. Therefore, comparing the momentum matrix element (MME $=\left|\langle c_{\mathrm{CBM}}, \mathbf{k}| \, \mathbf{p} \, |v_{\mathrm{VBM}}, \mathbf{k}\rangle\right|^2$) of the high symmetric structure and the distorted structure obtained from MD simulation will illustrate the role of the distortion directly, demonstrating their effects to the lifetime. The momentum matrix element with atomic orbitals can be expressed as [160]:

$$\begin{aligned} \langle c, \mathbf{k}| \, \mathbf{p} \, |v, \mathbf{k}\rangle &= \frac{m_0}{i\hbar} \langle c, \mathbf{k}| \, [\mathbf{r}, \mathbf{H}] \, |v, \mathbf{k}\rangle \\ &= \frac{m_0}{\hbar} \langle c, \mathbf{k}| \, \nabla_{\mathbf{k}} H(\mathbf{k}) \, |v, \mathbf{k}\rangle \end{aligned} \tag{4.10}$$

where $\nabla_{\mathbf{k}} H(\mathbf{k})$ can be solved analytically. With this quantity, the lifetime enhancement ($\tau^{-1}_{\mathrm{MD}} / \tau^{-1}_{\mathrm{highsym}}$) can be calculated and shown in Fig. 4.13. As we have seen, the magnitude of the lifetime enhancement in the MD trajectory is around 1.2 of the high symmetric structure. This enhancement is also very stable along the trajectory. Thus, the disordered feature of the $MAPbI_3$ creates the spatial separation of the VBM and CBM, which indeed contributes to the long excited carrier lifetime constantly.

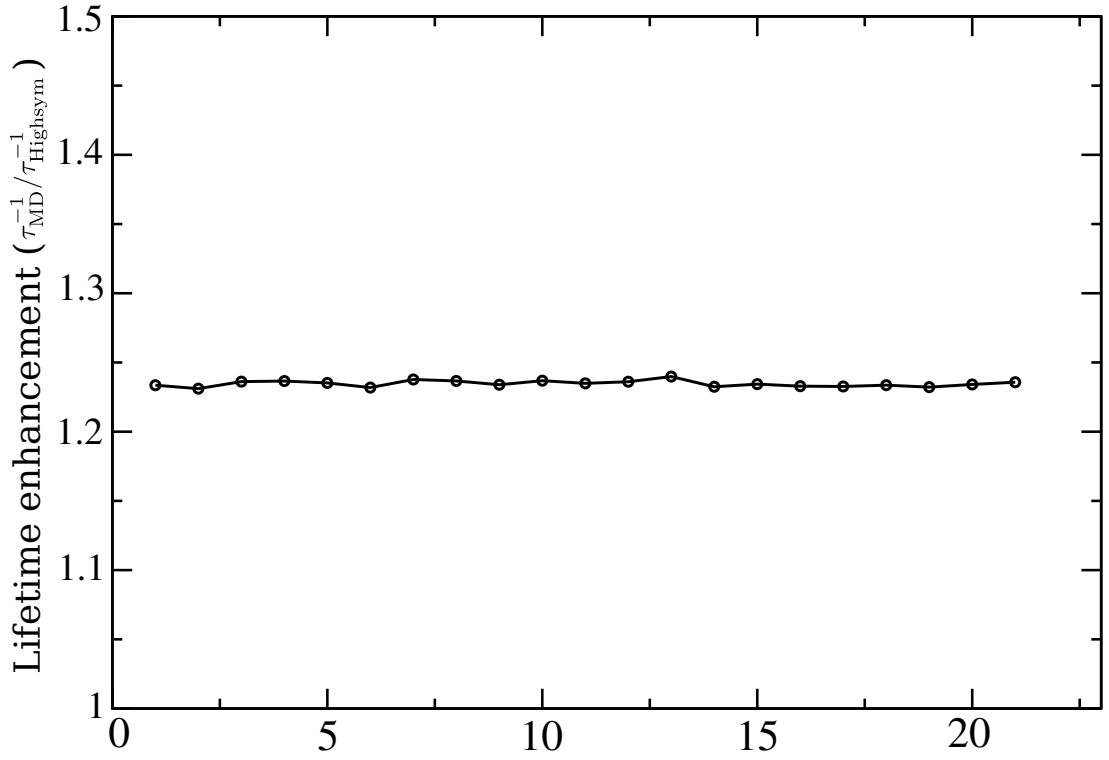

Figure 4.13: The lifetime enhancement factor ($\tau_{\mathrm{MD}}^{-1}/\tau_{\mathrm{highsym}}^{-1}$) computed with the MD trajectory and the high symmetric structure.

In summary, we have developed a TB model to describe the band edge states of the $MAPbI_3$. By fitting to the DFT calculated band structure, the TB model can reproduce the band gap, band structure and the orbital character very well. Combining with the classical MD trajectory, we can solve the electronic structure of the very large system using this TB model. We find that the band gap of the MD trajectory is rather stable. The previously observed large band gap fluctuation from ab initio MD is more likely to be the artifact of the system size. Moreover, it is noticed that the structure disorder can affect the spatial charge density distribution. The separation of the VBM and CBM in the real space causes the slow radiative recombination rate. We believe that this feature will also contribute to the exceptional long carrier lifetime observed in $MAPbI_3$ and other OMHPs.

4.3.3 Appendix

DFT calculation

To obtain the band structure, the plane-wave density functional theory (DFT) package Quantum Espresso is used with Perdew-Burke-Ernzerhof (PBE) generallized gradient approximation functional [144]. Norm-conserving, designed non-local pseudopotentials were generated with the OPIUM package [44, 45]. The plane-wave cutoff with 50 Ryd and k-point grid of $8\times8\times8$ are used to converge the total energy over the number of plane-waves and k-points. SOC is included to be consistent with the TB.

MD simulation

***ab initio* simulation**

Chapter 5

Bulk Photovoltaic Effect in $MAPbI_3$

[1]

[1] F. Zheng, H. Takenaka, F. Wang, N. Z. Koocher, and A. M. Rappe, *J. Phys. Chem. Lett.* **6**, 31 (2015)
S. M. Young, F. Zheng, and A. M. Rappe, *Phys. Rev. Lett.***109**, 236601 (2012)
S. M. Young, F. Zheng, and A. M. Rappe, *Phys. Rev. Lett.***110**, 057201 (2013)
J. A. Brehm, S. M. Young, F. Zheng, and A. M. Rappe, *J. Chem. Phys.***141**, 204704 (2014)

5.1 Introduction

Bulk photovoltaic effect (BPVE) is the phenomena in systems lacking inversion symmetry, where photo-current and giant photo-voltage are generated under light illumination [161].

Review of BPVE experiments. BPVE has been observed in many materials systems, including GaAs [162], quantum wells [163], organic crystals [164], and recently two-dimensional interfaces. [165] In particular, the BPVE in ferroelectric materials has been explored experimentally for more than fifty years. In ferroelectrics, the application of an external electric field is not necessary for the generation of photocurrent, as demonstrated in early work on the prototypical ferroelectric $BaTiO_3$ [166], where the photocurrent was attributed to surface space-charge layers. This was followed by studies [167, 168, 169, 170, 171, 172] showing the presence of photocurrents and photovoltages in many other ferroelectrics. Further developments include the strong dependence of photocurrent on light polarization direction in $BaTiO_3$ [173], and a giant BPVE in $LiNbO_3$ [174, 175] scaling linearly with light intensity. It was found that BPVE is enhanced in nanostructures. [176] For example, (Pb,La)(Zr,Ti)O_3 (PLZT), Pb(Zr,Ti)O_3 and the solid solutions in thin film form can have high photo-current magnitude. [177, 178, 179, 180]. This is further supported by the giant BPVE observed in $BaTiO_3$ thin films. [176]

The shift current theory was proposed as an explanation for the BPVE in $BaTiO_3$ by von Baltz and Kraut [181], and was later derived within the framework of Green's functions [182] and non-linear optics. [183] Young and Rappe reformulated the shift current theory to enable efficient calculation from first principles [184], and provided the first comparison of experimental BPVE data to shift current theory. [184] In subsequent first-principles studies of the shift current in ferroelectric materials, it was shown that the shift current is the main contributor to the BPVE. [185, 186, 187, 188, 189, 190, 191, 192]

In this Chapter, I will use $MAPbI_3$ as an example to systematically illustrate its shift

current response. The results of $BiFeO_3$ and $LiAsSe_2$ are also shown for comparison. At the end, by generalizing the shift current of these materials, general material design principles for high BPVE are raised with three examples illustrated.

5.2 $MAPbI_3$

5.2.1 Introduction

$MAPbI_3$ and related materials share similar perovskite structures with ferroelectric oxides. The tetragonal phase of $MAPbI_3$ was found to have ferroelectric response at room temperature [1]. Various I/V hysteresis measurements suggest that the current is related to the ferroelectric response [84, 80, 193, 88, 194]. In particular, the large measured open-circuit voltage allows for the possibility that the BPVE could make a big contribution to the photo-voltage, as the BPVE can generate a photo-voltage that is above a material's band gap. Therefore, studying the BPVE of $MAPbI_3$-based materials is important in terms of elucidating the underlying mechanism of their high efficiency and continuously optimizing their properties as a solar cell material. Here, we calculate the shift current response of $MAPbI_3$ and $MAPbI_{3-x}Cl_x$, and show that their current responses are approximately three times larger than that of $BiFeO_3$. Our calculations demonstrate that the molecular orientations as well as the Cl substitution position can strongly affect their shift current responses.

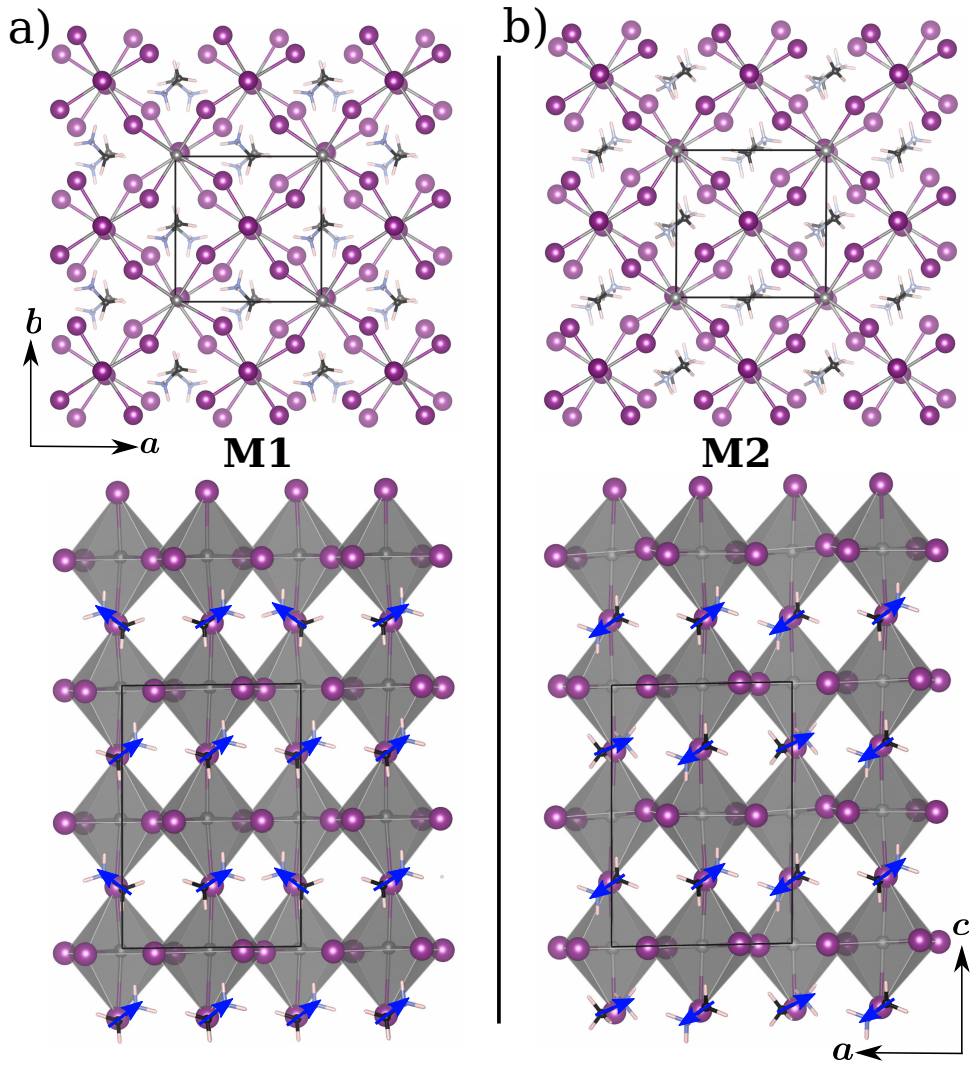

Figure 5.1: The top and side views of the relaxed $MAPbI_3$ structures with a) molecular orientation 1 (M1) and b) molecular orientation 2 (M2). M1 has all the net MA molecular dipoles along the c axis, while M2 has MA molecules with dipoles opposite to that of its neighboring molecules, yielding a net zero dipole. Four $MAPbI_3$ are considered in one unit cell. Pb: dark grey, I: purple, C: black, N: light blue, Cl: green, H: light pink.

5.2.2 Results

The increased symmetry at high temperature is related to the free rotation of the MA molecules, as observed in both experiments and theoretical calculations [2, 129, 76, 195, 60, 196]. In order to explore the effect of molecular orientation on the structure and shift current, structures with two different orientations, M1 and M2, starting from the tetragonal PbI_3 inorganic frame, are computed and shown in Fig. 5.1.

As shown in the table, our calculated lattice constants agree well with the experiments and theoretical works [106, 56, 103, 197, 196, 147]. The computed a and b lattice constants are slightly different depending on the molecular orientations, and because they are different, this confirms that the orthorhombic structure is favored at low temperature. Although the molecular orientations affect the lattice, the total energy difference between the M1 and M2 structures is small.

Table 5.1: The lattice constants and relative total energies, per unit cell, of the optimized MAPbI structures with molecular orientation M1 and molecular orientation M2. The experimental values are from Ref. [1, 2, 3]. Total energy (per 48 atom cell) of the M2 orientation structure is set to zero.

	M1	M2	exp.
a (Å)	8.97	9.00	8.85
b (Å)	8.86	8.77	8.85
c (Å)	12.85	12.95	12.44–12.66
E_{T} (eV)	0.021	0	-

Because the zzZ response tensor component is the dominant component among all the tensor elements, Fig. 5.2 shows the MAPbI thin sample limit shift current response σ_{zzZ} and Glass coefficient response G_{zzZ} for the M1 and M2 structures with and without SOC. Since the direct band gap calculated with SOC is smaller than that without SOC, the onset energy of the shift current response calculated with SOC is lower than that calculated without SOC, as shown in Fig. 5.2. Also, the SOC tends to shift the whole spectrum without substantially changing its magnitude. On average, the M2 structure has a much smaller current response and Glass coefficient than the M1 structure. The magnitude of the Glass coefficient is closely related to material symmetry and state delocalization [29]. We have shown that a strongly distorted structure with delocalized states involved in an optical transition tends to give a large Glass coefficient response. Polarization calculations show that the M1 structure has a polarization of $5\mu\mathrm{C}/\mathrm{cm}^2$, while the M2 structure has nearly zero polarization. Since the bulk polarization contribution from the molecular dipole moment is estimated to be less than $2.5\mu\mathrm{C}/\mathrm{cm}^2$ [198, 199]the PbI_3 inorganic lattice is a significant contributor to the M1 structure's polarization, as much larger Pb displacement ($\approx$ 0.07 Å along z) was observed than in M2 structure ($\approx$ 0.01 Å along z). As a result, the distorted M1 structure provides a larger shift current response than the more symmetric M2 structure. At room temperature, the shift current responses can be the average of the M1 and M2 cases due to the disordered molecular orientations. Limiting the molecular rotation by methods such as doping, lattice shrinkage, or application of electric field can highlight the current contribution from one particular orientation. An understanding of the dependence of the current on molecular and polarization orientations is helpful in understanding the I/V hysteresis under different applied voltage scanning rates.

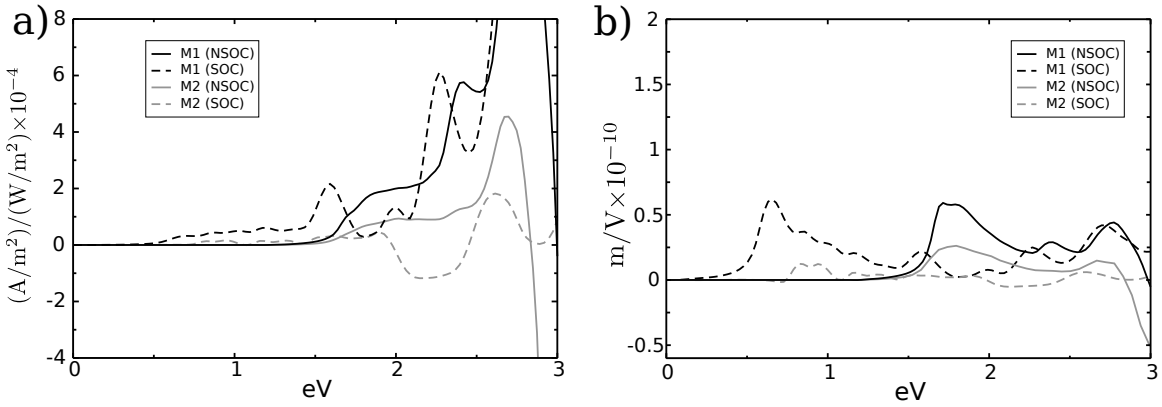

Figure 5.2: a) Shift current response σ_{zzZ} and b) Glass coefficient G_{zzZ} vs. incident photon energy for structures with molecular orientation M1 and orientation M2. The M1 structure provides a larger shift current response and Glass coefficient than the M2 structure. Calculations with and without SOC show the same trend for the two orientations.

Adding Cl has been shown to provide a diffusion length as long as 1 μm without substantially changing the absorption spectrum [63, 67, 4]. Since MAPbICl has been found to have a reduced lattice constant along the c axis compared to MAPbI, it is thought that Cl substitutes I at the apical site of the PbI_6 octahedra, but the actual Cl position is still not clear [200, 201]. In order to understand the effects of Cl position on shift current, we study different Cl substitution configurations at the apical and equatorial sites for both molecular orientations, as shown in Fig. 5.3.

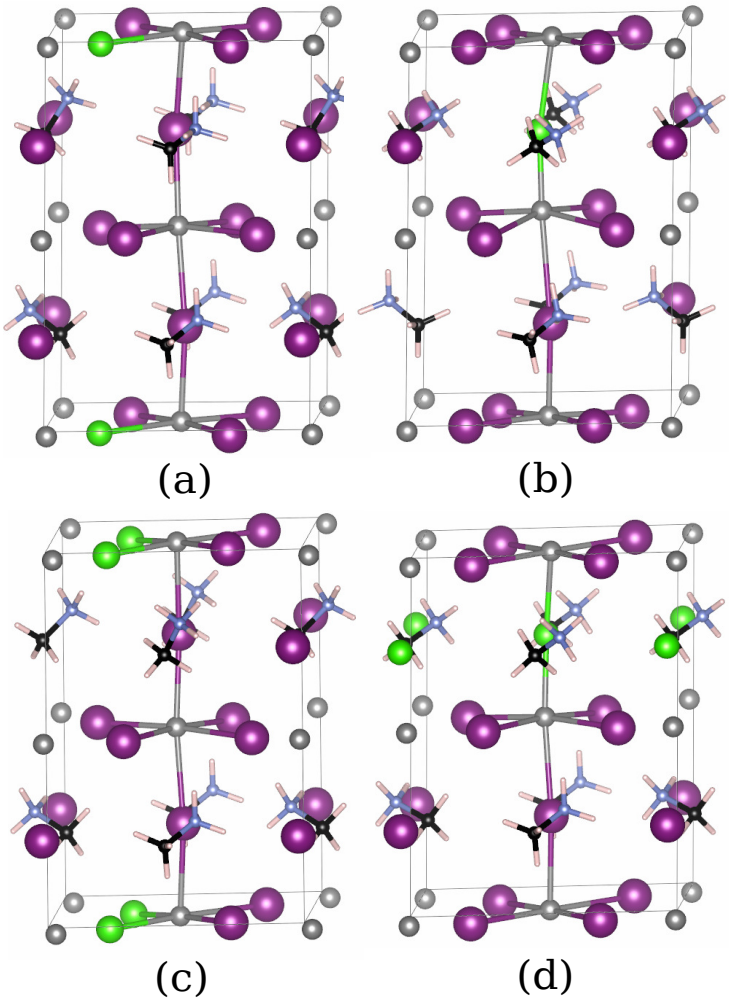

Figure 5.3: Fully relaxed structures of MAPbICl with one (a and b) or two (c and d) Cl atoms per unit cell. The structures shown here have molecular orientation M1. Structures a and c have equatorial site substitution; structures b and d have apical substitution. The corresponding four structures with molecular orientation M2 are also tested, but are not shown here.

The structures with one and two Cl atoms in one unit cell (with 48 atoms) are fully relaxed, and their band gaps and polarization magnitudes are shown in Table 5.2. The structures with Cl at different positions have similar total energies (≈30 meV of the total energy difference), indicating their similar thermal stabilities. We find that although the Cl position has no substantial effect on the polarization, it strongly affects the shift current responses.

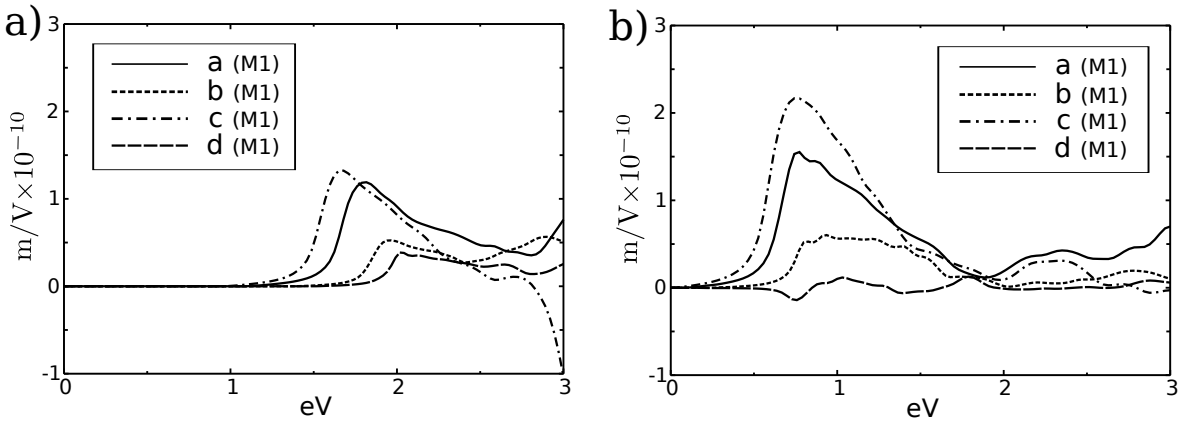

Figure 5.4: Glass coefficient G_{zzZ} calculated with a) NSOC and b) SOC vs. incident photon energy for the four relaxed structures (a, b, c and d) shown in Fig. 5.3.

Fig. 5.4 shows the Glass coefficient G_{zzZ}. Responses with and without SOC show a similar trend for different Cl positions and concentrations. Interestingly, the apical site substitution of I with Cl tends to give relatively small shift current responses, while the equatorial site substitution shows much larger responses. This can be explained from wave-function projections. Our electronic structure calculations show that Pb *p* orbital character

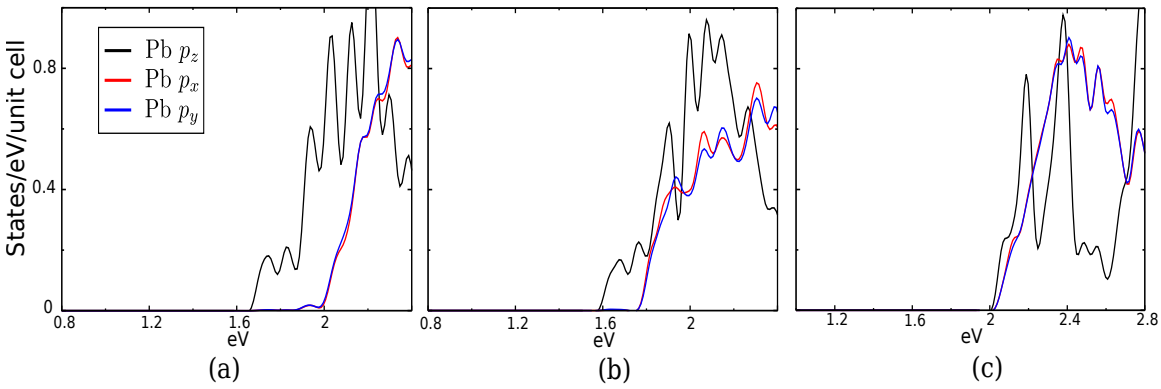

Figure 5.5: The projected density of states (PDOS) for Pb atoms calculated from structure a) M1 orientation without Cl in Fig. 5.1, b) structure c(M1) and c) d(M1) in Fig. 5.3. Energy of the VBM is set to zero.

slightly hybridized with I dominates the conduction bands near the band gap. In the highly symmetric structure without octahedral tilting, Pb p_x, p_y and p_z will be degenerate and hybridized with I s. However, the distortion of Pb-I bonds on the a-b plane will cause the Pb p orbitals to hybridize with I p orbitals in addition to I s orbitals. This will lift the original degeneracy between $p_{x/y}$ and p_z, allowing Pb p_z to become the dominant orbital character of the CBM. This is very clear in the NSOC case. Wave functions calculated with SOC show a similar picture, but it is not as obvious as in the NSOC case since orbitals with different angular momentum are mixed together. We can see from the projected density of states (PDOS) calculated without SOC (Fig. 5.5) that for the structure without Cl, the CBM has mostly Pb p_z orbital character. With increasing Cl concentration at the apical site, the strong electronegativity of Cl increases the energy bands with Pb p_z orbital character while

leaving $p_{x/y}$ unchanged, allowing for a larger band gap. The CBM state, mainly composed of hybridized $p_{x/y}$ orbital character, reduces the current flowing along z direction, since the $p_{x/y}$ orbitals are less delocalized than p_z orbitals along z. However, the Cl concentration only moderately affects the shift current response, as structures containing one Cl atom yield responses similar in magnitude to those of structures containing two Cl atoms.

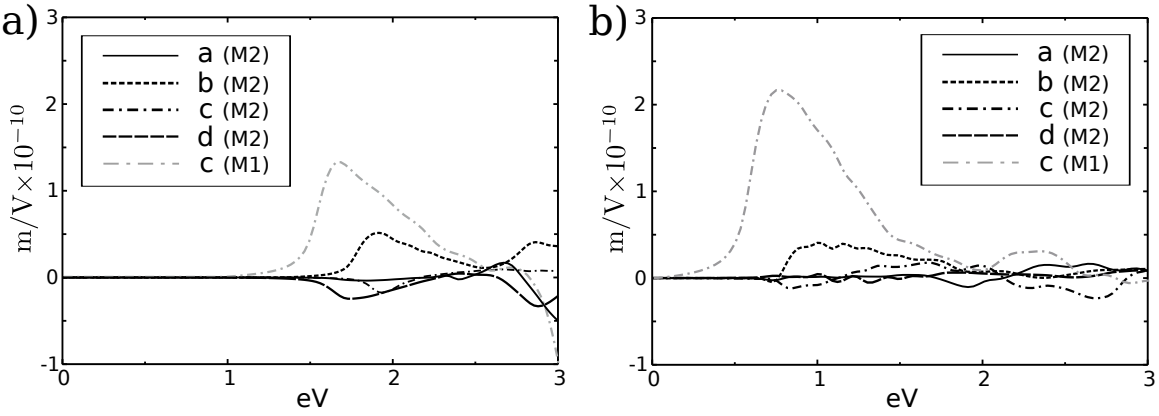

Figure 5.6: Glass coefficient G_{zzZ} a) without and b) with SOC for the four relaxed structures (a, b, c and d) shown in Fig. 5.3, but with molecular orientation M2. For comparison, the largest response from the M1 case (structure c(M1)) is also plotted as a grey line. On average, the M2 orientation gives smaller responses than the M1 orientation for the four structures.

The shift current is also calculated for the molecular orientation M2, which has the same Cl configurations discussed previously. Overall, their responses, shown in Fig. 5.6, are smaller than that corresponding to the M1 orientation, and are similar to the case without Cl. The minor electronic contribution of the organic species at the band edge, evident from the PDOS, suggests that the effect of the molecular orientation on the shift current is likely indirect, occurring through the PbI_3 frame. In this case, because the molecular dipoles for the neighboring molecules are opposite, does anyone notice this weired sentence coming out here, there is no net dipolar effect on the PbI_3 frame, resulting in a nearly symmetric frame. As the distortion decreases, the dependence of current response on different Cl position becomes less significant, as in the M1 case.

Table 5.2: Total polarization magnitude ($|P|$), z component ($|P_z|$), and band gap for MAPbI and MAPbICl structures (a, b, c and d shown in Fig. 5.3) with both molecular orientations (M1 and M2).

Structure	M1				M2			
	$\|P\|$ (μC/cm^2)	$\|P_z\|$ (μC/cm^2)	Band gap (eV) NSOC	SOC	$\|P\|$ (μC/cm^2)	$\|P_z\|$ (μC/cm^2)	Band gap (eV) NSOC	SOC
MAPbI	6.8	5.0	1.72	0.69	0.7	0.5	1.70	0.75
a	8.3	7.2	1.75	0.76	1.8	1.0	1.72	0.80
b	8.0	6.3	1.90	0.83	2.6	2.4	1.84	0.83
c	6.9	6.2	1.93	0.83	2.3	0.3	1.93	0.83
d	6.1	4.4	1.96	0.84	3.3	3.2	1.91	0.83

In summary, we calculate the shift current responses and polarization magnitudes of MAPbI and MAPbICl from first principles with and without SOC. We find that the SOC does not substantially alter the spectrum, though it reduces the band gap. Rather, the MA orientation and Cl substitution position can strongly affect the shift current response. When the MA molecules' net dipole moments are aligned in parallel, the PbI_3 inorganic frame becomes more distorted, resulting in relatively large shift current responses. Conversely, when the molecules have opposite dipole moments, the structure is nearly symmetric, resulting in much smaller shift current responses. The substitution of Cl at the equatorial site can enhance the shift current response, because the orbital character contribution at the CBM is more delocalized along the shift current direction. Thus a higher shift current response can be obtained by introducing a large lattice distortion with MA molecules aligned in parallel, and by substituting Cl at equatorial positions.

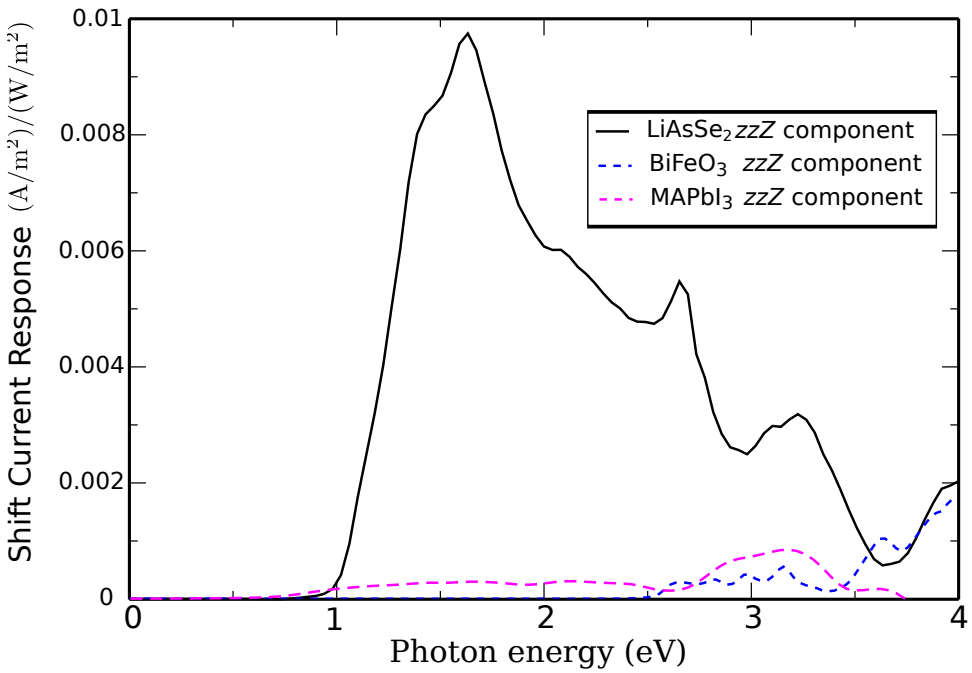

Figure 5.7: The shift current σ calculated for BFO, $LiAsSe_2$ and $MAPbI_3$ for comparison.

5.3 BPVE in $BiFeO_3$, $MAPbI_3$ and $LiAsSe_2$

For comparison, the magnitude of the shift currents of $MAPbI_3$, BFO [202] and $LiAsSe_2$ are plotted in one graph (Fig 5.7). It is found that $LiAsSe_2$ holds record of the highest shift current computed, which is more than 40 times larger than that of BFO [33]. Here, $MAPbI_3$ (with Cl doping) shows around three times larger shift current response compared to BFO, although the polarization of BFO is much higher. (The polarization of BFO is $\approx 90\mu\mathrm{C/cm^2}$ [203]; $MAPbI_3$ is $\approx 6\mu\mathrm{C/cm^2}$.) The polarization is not directly related to the shift current magnitude [29]. The difference of the shift current between BFO and $MAPbI_3$ is mainly due to the delocalized orbital character in the latter where the edge states mainly have s or p orbital characters. While in BFO, the localized d orbital character from iron hamper the shift current response, leading to relatively low magnitude. Based on these ideas, we also designed new materials for potential solar cell applications. The details of the material deisign can be found in Ref. [204].

5.4 Summary

In this Chapter, the shift current responses of $MAPbI_3$ are systematically studied, including the effect of the Cl doping. This material can gives three times as large as BFO although its polarization is much smaller. We think this is owing to the delocalized orbital characters near the band edges. Following that, shift current responses of BFO and $LiAsSe_2$ are summarized and compared. $LiAsSe_2$ has the largest shift current response among all the materials we studied, which is more than 40 time larger than that of BFO. These findings reveal that the delocalized states near the band edge, small band gap and spontaneous polarization are needed for large BPVE response.

Chapter 6

Summary and Future Directions

In this thesis, I have described the main work I have done during my Ph.D. As a summary, the main topic is to use the first-principles method to study the light-matter interactions for the solar cell applications. In particular, I focused on three types of materials: Alkali-metal chalcogenides such as $LiAsSe_2$, organometal-halide perovskite such as $MAPbI_3$ and inorganic oxide perovskite such as $BiFeO_3$. By studying the different kinds of properties of these three types of materials, we generalized the basic rules to design a material for the solar cell:

- high absorption. For example in $LiAsSe_2$, it is found that by compressing the volume, the absorption and optical dielectric can be enhanced more than three times. We think this enhancement originates from the wavefunction change induced by the dimerization variations. This property is due to the special arrangement of the 2D atomic-chains in the plane, which leads to the sensitive wavefunction-structure relation.

- long diffusion length. organometal-halide perovskites (such as $MAPbI_3$) exhibit very long carrier lifetime and the resulting long diffusion length, making this material exceptional for the next generation solar cells. In this work, we use the first-principles method to understand the reason for such long carrier lifetime. We think there are two contributions: a) the strong spin-orbilt coupling and the ferroelectric distortion introduce the Rashba effect for the band edges, which leads to the "spin-indirect" band gap, i.e. the recombination of the excited carriers is spin-forbidden due to the special spin-helicity in the Rashba bands. b) At the finite temperature, the strong spacial and temporal disorder of both A site molecules and Pbi_3 sublattice tend to generate the localized change density of the conduction and valence bands edges at difference regions in the real space. This separation further slows down their recombination rate due to their spacial "non-overlap" feature, which is demonstrated

by our transition rate calculations.

- non-linear optical effect. Non-linear optical effect, such as bulk photovoltaic effect (BPVE) has been studied intensely due to its advantages over the normal optical effect. Here, the example of $MAPbI_3$ is used to illustrate the BPVE calculations and the analysis. Although the polarization of $MAPbI_3$ is only around one tenth of the $BiFeO_3$, its BPVE is almost three times larger than that of $BiFeO_3$, demonstrating its significant role for non-linear optics. In this work, we also studied the effect of spin-orbit coupling, and the Cl-doping to the BPVE responses. In particular, we found that the Cl-doping at the apical site can enhance the BPVE by enlarging the structural distortion. This can contribute to the understanding of the role of Cl in enhancing the performance of this material as the solar cell, although the existence of Cl is still elusive. Furthermore, by comparing to $BiFeO_3$ and $LiAsSe_2$, we designed new materials for the high BPVE, which could be the potential materials for the solar cell applications.

By summarizing the finished work, we have planned the future directions for further investigations.

Long carrier lifetime. Understanding the long carrier lifetime in organometal-halide perovskite is still very important due to the incomplete knowledge for this exceptional property. A full understanding can further benefit the design of the similar properties but more advantaged materials. The electron-lattice coupling, as the most important intrinsic factor, is more emphasized in addition to the extrinsic effects, such as defect. This is because of the strong dynamic disorder observed in these materials. Therefore, we plan to have a complete understanding of the wavefunction evolution under the existence of the coupled phonons. This approach requires the time-dependent picture of the electronic structure as well as the ionic movement. Our developed large-scale tight-binding model

could be useful due to its low cost but ability for large systems.

BPVE in Bi(Fe,Cr)O_3. In the experiment, it is found that the ordered structure of Bi(Fe,Cr)O_3 shows enhanced bulk photovoltaic effect. However, the reason for this structure-performance is still unclear. Therefore, we want to understand its origin using the shift current calculations. In particular, our preliminary results suggest that the ordered structure indeed leads to more enhanced BPVE responses. This enhancement is not because of the loss of the polarization, instead, the ordered feature provides more fundamental reasons which need us to reveal.

BPVE in low-dimensional materials. We have done a lot of work to study the BPVE in 3D bulk materials. However, the low-dimensional materials' responses are largely unknown. But these materials show many exceptional properties. For example, low dimensional materials tend to give higher density of states, which can strongly lift the BPVE performances for the solar cell. Our preliminary calculations of the 1D polymer demonstrate this enhancement. Thus, understanding the physics in these materials will benefit the materials design with higher power conversion efficiency. Furthermore, many exotic physics have been explored in the 2D and 1D materials. Understanding the BPVE of these materials can further bridge the shift current mechanism to these new physics.

Bibliography

[1] Stoumpos, C. C.; Malliakas, C. D.; Kanatzidis, M. G. *Inorg. Chem.* **2013**, *52*, 9019–9038.

[2] Poglitsch, A.; Weber, D. *J. Chem. Phys.* **1987**, *87*, 6373–6378.

[3] Baikie, T.; Fang, Y.; Kadro, J. M.; Schreyer, M.; Wei, F.; Mhaisalkar, S. G.; Graetzel, M.; White, T. J. *J. of Mater. Chem. A* **2013**, *1*, 5628–5641.

[4] Green, M. A.; Ho-Baillie, A.; Snaith, H. J. *Nature Photonics* **2014**, *8*, 506–514.

[5] Wäsche, R.; Denner, W.; Schulz, H. *Materials Research Bulletin* **1981**, *16*, 497–500.

[6] Ivanov, S.; Tellgren, R.; Porcher, F.; Ericsson, T.; Mosunov, A.; Beran, P.; Korchagina, S.; Kumar, P. A.; Mathieu, R.; Nordblad, P. *Materials Research Bulletin* **2012**, *47*, 3253–3268.

[7] *IER Institue For Energy Research*; `http://instituteforenergyresearch.org/topics/encyclopedia/solar/`; Accessed: 7-06-2016.

[8] *Timeline of Solar Cells*; `https://en.wikipedia.org/wiki/Timeline_of_solar_cells`; Accessed: 7-06-2016.

[9] Asahi, R.; Morikawa, T.; Ohwaki, T.; Aoki, K.; Taga, Y. *Science* **2001**, *293*, 269–271.

[10] Gai, Y.; Li, J.; Li, S.-S.; Xia, J.-B.; Wei, S.-H. *Phys. Rev. Lett.* **2009**, *102*.

[11] Serpone, N. *The Journal of Physical Chemistry B* **2006**, *110*, 24287–24293.

[12] Coletti, C.; Riedl, C.; Lee, D. S.; Krauss, B.; Patthey, L.; von Klitzing, K.; Smet, J. H.; Starke, U. *Phys. Rev. B* **2010**, *81*.

[13] Grinberg, I.; West, D. V.; Torres, M.; Gou, G.; Stein, D. M.; Wu, L.; Chen, G.; Gallo, E. M.; Akbashev, A. R.; Davies, P. K.; Spanier, J. E.; Rappe, A. M. *Nature* **2013**, *503*, 509–512.

[14] Jiang, L.; Grinberg, I.; Wang, F.; Young, S. M.; Davies, P. K.; Rappe, A. M. *Phys. Rev. B* **2014**, *90*, 075153.

[15] Wang, F.; Rappe, A. M. *Phys. Rev. B* **2015**, *91*.

[16] Wang, F.; Grinberg, I.; Rappe, A. M. *Phys. Rev. B* **2014**, *89*, 235105.

[17] Wang, F.; Grinberg, I.; Rappe, A. M. *Appl. Phys. Lett.* **2014**, *104*, 152903.

[18] Liu, S.; Zheng, F.; Koocher, N. Z.; Takenaka, H.; Wang, F.; Rappe, A. M. *J. Phys. Chem. Lett.* **2015**, *6*, 693–699.

[19] Chikamatsu, M.; Taima, T.; Yoshida, Y.; Saito, K.; Yase, K. *Applied physics letters* **2004**, *84*, 127–129.

[20] Schaadt, D. M.; Feng, B.; Yub, E. T. *Appl. Phys. Lett.* **2005**, *86*, 063106–1–3.

[21] Beck, F.; Polman, A.; Catchpole, K. *Journal of Applied Physics* **2009**, *105*, 114310–1–114310–7.

[22] Santra, P. K.; Kamat, P. V. *Journal of the American Chemical Society* **2012**, *134*, 2508–2511.

[23] Li, L.; Wang, W.; Liu, H.; Liu, X.; Song, Q.; Ren, S. *The Journal of Physical Chemistry C* **2009**, *113*, 8460–8464.

[24] Grosso, G.; Parravicini, G. P. *Solid State Physics*, 1st ed.; Academic Press, 2000.

[25] Perdew, J. P.; Ruzsinszky, A.; Tao, J.; Staroverov, V. N.; Scuseria, G. E.; Csonka, G. I. *The Journal of Chemical Physics* **2005**, *123*, 062201.

[26] Tao, J.; Perdew, J. P.; Staroverov, V. N.; Scuseria, G. E. *Phys. Rev. Lett.* **2003**, *91*.

[27] Baroni, S.; de Gironcoli, S.; Dal Corso, A. *Rev. Mod. Phys.* **2001**, *73*, 515–562.

[28] Giannozzi, P.; de Gironcoli, S.; Pavone, P.; Baroni, S. *Phys. Rev. B* **1991**, *43*, 7231–42.

[29] Young, S. M.; Rappe, A. M. *Phys. Rev. Lett.* **2012**, *109*, 116601.

[30] Young, S. M. *Ph.D. Dissertation* **2013**, 1–220.

[31] Glass, A. M.; von der Linde, D.; Negran, T. J. *Appl. Phys. Lett.* **1974**, *25*, 233–5.

[32] Bera, T. K.; Jang, J. I.; Song, J.-H.; Malliakas, C. D.; Freeman, A. J.; Ketterson, J. B.; Kanatzidis, M. G. *Journal of the American Chemical Society* **2010**, *132*, 3484–3495.

[33] Brehm, J. A.; Young, S. M.; Zheng, F.; Rappe, A. M. *J. Chem. Phys.* **2014**, *141*, 204704.

[34] Song, J.-H.; Freeman, A. J.; Bera, T. K.; Chung, I.; Kanatzidis, M. G. *Physical Review B* **2009**, *79*, 245203–1–245203–6.

[35] Ni, B.-L.; Zhou, H.-G.; Jiang, J.-Q.; Li, Y.; Zhang, Y.-F. *Acta Physico-Chimica Sinica* **2010**, *26*, 3052.

[36] Gulyamov, K.; VA, L.; NA, T.; Fridkin, V. *Doklady Akademii Nauk SSSR* **1965**, *161*, 1060.

[37] Cretu, O.; Botello-Mendez, A. R.; Janowska, I.; Pham-Huu, C.; Charlier, J.-C.; Banhart, F. *Nano Letters* **2013**, *13*, 3487–3493.

[38] Wang, X. F.; Roncaioli, C.; Eckberg, C.; Kim, H.; Yong, J.; Nakajima, Y.; Saha, S. R.; Zavalij, P. Y.; Paglione, J. *Phys. Rev. B* **2015**, *92*, 020508–1–020508–6.

[39] Torre, A. L.; Botello-Mendez, A.; Baaziz, W.; Charlier, J. C.; Banhart, F. *Nat Comms* **2015**, *6*, 6636.

[40] Farhan, M. A.; Lee, G.; Shim, J. H. *Journal of Physics: Condensed Matter* **2014**, *26*, 042201–1–042201–7.

[41] Steinberg, J. A.; Young, S. M.; Zaheer, S.; Kane, C. L.; Mele, E. J.; Rappe, A. M. *Phys. Rev. Lett.* **2014**, *112*, 036403–036407.

[42] *See Supplemental Material at [] for the lattices and the atomic positions of the experimental and the compressed structures*.

[43] Giannozzi, P.; et al. *J. Phys.: Condens. Matter* **2009**, *21*, 395502–20.

[44] Rappe, A. M.; Rabe, K. M.; Kaxiras, E.; Joannopoulos, J. D. *Phys. Rev. B Rapid Comm.* **1990**, *41*, 1227–30.

[45] Ramer, N. J.; Rappe, A. M. *Phys. Rev. B* **1999**, *59*, 12471–8.

[46] Erhart, P.; Klein, A.; Åberg, D.; Sadigh, B. *Phys. Rev. B* **2014**, *90*, 035204–1–035204–8.

[47] Slipukhina, I.; Mavropoulos, P.; Blügel, S.; Ležaić, M. *Phys. Rev. Lett.* **2011**, *107*, 137203–1–137203–5.

[48] Mostofi, A. A.; Yates, J. R.; Lee, Y.-S.; Souza, I.; Vanderbilt, D.; Marzari, N. *Comput. Phys. Commun.* **2008**, *178*, 685.

[49] Kim, H.-S.; Lee, C.-R.; Im, J.-H.; Lee, K.-B.; Moehl, T.; Marchioro, A.; Moon, S.-J.; Humphry-Baker, R.; Yum, J.-H.; Moser, J. E.; Grätzel, M.; Park, N.-G. *Sci. Rep.* **2012**, *2*, 591–597.

[50] Zhou, H.; Chen, Q.; Li, G.; Luo, S.; Song, T.-b.; Duan, H.-S.; Hong, Z.; You, J.; Liu, Y.; Yang, Y. *Science* **2014**, *345*, 542–546.

[51] Jeon, N. J.; Lee, H. G.; Kim, Y. C.; Seo, J.; Noh, J. H.; Lee, J.; Seok, S. I. *Journal of the American Chemical Society* **2014**, *136*, 7837–7840.

[52] *NREL. Research Cell Efficiency Records.*; `http://www.nrel.gov/ncpv/images/efficiency_chart.jpg`.

[53] Stoumpos, C. C.; Frazer, L.; Clark, D. J.; Kim, Y. S.; Rhim, S. H.; Freeman, A. J.; Ketterson, J. B.; Jang, J. I.; Kanatzidis, M. G. *J. Am. Chem. Soc.* **2015**, *137*, 6804–6819.

[54] Papavassiliou, G. C.; Koutselas, I. *Synth. Met.* **1995**, *71*, 1713–1714.

[55] Noel, N. K.; Stranks, S. D.; Abate, A.; Wehrenfennig, C.; Guarnera, S.; Haghighirad, A.; Sadhanala, A.; Eperon, G. E.; Pathak, S. K.; Johnston, M. B.; Petrozza, A.; Herz, L. M.; Snaith, H. J. *Energy Environ. Sci.* **2014**, *7*, 3061–3068.

[56] Umari, P.; Mosconi, E.; De Angelis, F. *Scientific Reports* **2014**, *4*, 4467.

[57] Chiarella, F.; Zappettini, A.; Licci, F.; Borriello, I.; Cantele, G.; Ninno, D.; Cassinese, A.; Vaglio, R. *Phys. Rev. B* **2008**, *77*, 045129.

[58] Ogomi, Y.; Morita, A.; Tsukamoto, S.; Saitho, T.; Fujikawa, N.; Shen, Q.; Toyoda, T.; Yoshino, K.; Pandey, S. S.; Ma, T.; Hayase, S. *Journal of Physical Chemistry Letters* **2014**, *5*, 1004–1011.

[59] Eperon, G. E.; Stranks, S. D.; Menelaou, C.; Johnston, M. B.; Herz, L. M.; Snaith, H. J. *Energy Environ. Sci.* **2014**, *7*, 982–988.

[60] Mosconi, E.; Quarti, C.; Ivanovska, T.; Ruani, G.; De Angelis, F. *Phys. Chem. Chem. Phys.* **2014**, *16*, 16137–16144.

[61] Filip, M. R.; Giustino, F. *Phys. Rev. B* **2014**, *90*, 245145.

[62] Feng, J.; Xiao, B. *The Journal of Physical Chemistry Letters* **2014**, *5*, 1278–1282.

[63] Filippetti, A.; Mattoni, A. *Physical Review B* **2014**, *89*, 125203.

[64] Ponseca, J., Carlito S.; Savenije, T. J.; Abdellah, M.; Zheng, K.; Yartsev, A.; Pascher, T.; Harlang, T.; Chabera, P.; Pullerits, T.; Stepanov, A.; Wolf, J.-P.; Sundstrom, V. *Journal of the American Chemical Society* **2014**, *136*, 5189–5192.

[65] Edri, E.; Kirmayer, S.; Mukhopadhyay, S.; Gartsman, K.; Hodes, G.; Cahen, D. *Nature Communications* **2014**, *5*, 3461.

[66] Xing, G.; Mathews, N.; Sun, S.; Lim, S. S.; Lam, Y. M.; Graetzel, M.; Mhaisalkar, S.; Sum, T. C. *Science* **2013**, *342*, 344–347.

[67] Stranks, S. D.; Eperon, G. E.; Grancini, G.; Menelaou, C.; Alcocer, M. J.; Leijtens, T.; Herz, L. M.; Petrozza, A.; Snaith, H. J. *Science* **2013**, *342*, 341–344.

[68] Wehrenfennig, C.; Eperon, G. E.; Johnston, M. B.; Snaith, H. J.; Herz, L. M. *Advanced Materials* **2014**, *26*, 1584–1589.

[69] Niu, G.; Li, W.; Meng, F.; Wang, L.; Dong, H.; Qiu, Y. *Journal of Materials Chemistry A* **2014**, *2*, 705–710.

[70] Leguy, A. M. A.; Hu, Y.; Campoy-Quiles, M.; Alonso, M. I.; Weber, O. J.; Azarhoosh, P.; van Schilfgaarde, M.; Weller, M. T.; Bein, T.; Nelson, J.; Docampo, P.; Barnes, P. R. F. *Chem. Mater.* **2015**, *27*, 3397–3407.

[71] Christians, J. A.; Herrera, P. A. M.; Kamat, P. V. *J. Am. Chem. Soc.* **2015**, *137*, 1530–1538.

[72] Yang, J.; Siempelkamp, B. D.; Liu, D.; Kelly, T. L. *ACS Nano* **2015**, *9*, 1955–1963.

[73] Mosconi, E.; Azpiroz, J. M.; Angelis, F. D. *Chemistry of Materials* **2015**, *27*, 4885–4892.

[74] Koocher, N. Z.; Saldana-Greco, D.; Wang, F.; Liu, S.; Rappe, A. M. *J. Phys. Chem. Lett.* **2015**, *6*, 4371–4378.

[75] Delugas, P.; Filippetti, A.; Mattoni, A. *Phys. Rev. B* **2015**, *92*, 045301.

[76] Frost, J. M.; Butler, K. T.; Brivio, F.; Hendon, C. H.; van Schilfgaarde, M.; Walsh, A. *Nano Lett.* **2014**, *14*, 2584–2590.

[77] Bass, K. K.; McAnally, R. E.; Zhou, S.; Djurovich, P. I.; Thompson, M. E.; Melot, B. C. *Chem. Commun.* **2014**, *50*, 15819–15822.

[78] Hailegnaw, B.; Kirmayer, S.; Edri, E.; Hodes, G.; Cahen, D. *J. Phys. Chem. Lett.* **2015**, *6*, 1543–1547.

[79] Niu, G.; Guo, X.; Wang, L. *J. Mater. Chem. A* **2015**, *3*, 8970–8980.

[80] Sanchez, R. S.; Gonzalez-Pedro, V.; Lee, J.-W.; Park, N.-G.; Kang, Y. S.; Mora-Sero, I.; Bisquert, J. *The Journal of Physical Chemistry Letters* **2014**, *5*, 2357–2363.

[81] Egger, D. A.; Edri, E.; Cahen, D.; Hodes, G. *J. Phys. Chem. Lett.* **2015**, *6*, 279–282.

[82] Kim, H.-S.; Park, N.-G. *J. Phys. Chem. Lett.* **2014**, *5*, 2927–2934.

[83] Chen, H.-W.; Sakai, N.; Ikegami, M.; Miyasaka, T. *J. Phys. Chem. Lett.* **2015**, *6*, 164–169.

[84] Snaith, H. J.; Abate, A.; Ball, J. M.; Eperon, G. E.; Leijtens, T.; Noel, N. K.; Stranks, S. D.; Wang, J. T.-W.; Wojciechowski, K.; Zhang, W. *J. Phys. Chem. Lett.* **2014**, *5*, 1511–1515.

[85] Unger, E. L.; Hoke, E. T.; Bailie, C. D.; Nguyen, W. H.; Bowring, A. R.; Heumüller, T.; Christoforo, M. G.; McGehee, M. D. *Energy Environ. Sci.* **2014**, *7*, 3690–3698.

[86] Tress, W.; Marinova, N.; Moehl, T.; Zakeeruddin, S.; Nazeeruddin, M. K.; Grätzel, M. *Energy & Environmental Science* **2015**, *8*, 995–1004.

[87] Liu, C.; Fan, J.; Zhang, X.; Shen, Y.; Yang, L.; Mai, Y. *ACS applied materials & interfaces* **2015**, *7*, 9066–9071.

[88] Docampo, P.; Hanusch, F. C.; Giesbrecht, N.; Angloher, P.; Ivanova, A.; Bein, T. *APL Materials* **2014**, *2*, 081508–081513.

[89] Kim, H.-S.; Kim, S. K.; Kim, B. J.; Shin, K.-S.; Gupta, M. K.; Jung, H. S.; Kim, S.-W.; Park, N.-G. *J. Phys. Chem. Lett.* **2015**, *6*, 1729–1735.

[90] Nie, W.; Tsai, H.; Asadpour, R.; Blancon, J.-C.; Neukirch, A. J.; Gupta, G.; Crochet, J. J.; Chhowalla, M.; Tretiak, S.; Alam, M. A.; et al. *Science* **2015**, *347*, 522–525.

[91] Zheng, F.; Saldana-Greco, D.; Liu, S.; Rappe, A. M. *J. Phys. Chem. Lett.* **2015**, *6*, 4862–4872.

[92] Yang, W. S.; Noh, J. H.; Jeon, N. J.; Kim, Y. C.; Ryu, S.; Seo, J.; Seok, S. I. *Science* **2015**, *348*, 1234–1237.

[93] Takahashi, Y.; Obara, R.; Lin, Z.-Z.; Takahashi, Y.; Naito, T.; Inabe, T.; Ishibashi, S.; Terakura, K. *Dalton Transactions* **2011**, *40*, 5563–5568.

[94] Takahashi, Y.; Hasegawa, H.; Takahashi, Y.; Inabe, T. *Journal of Solid State Chemistry* **2013**, *205*, 39–43.

[95] Pisoni, A.; Jaćimović, J.; Barišić, O. S.; Spina, M.; Gaál, R.; Forró, L.; Horváth, E. *J. Phys. Chem. Lett.* **2014**, *5*, 2488–2492.

[96] Deschler, F.; Price, M.; Pathak, S.; Klintberg, L. E.; Jarausch, D.-D.; Higler, R.; Huettner, S.; Leijtens, T.; Stranks, S. D.; Snaith, H. J.; Atatuere, M.; Phillips, R. T.; Friend, R. H. *Journal of Physical Chemistry Letters* **2014**, *5*, 1421–1426.

[97] Tan, Z.-K.; Moghaddam, R. S.; Lai, M. L.; Docampo, P.; Higler, R.; Deschler, F.; Price, M.; Sadhanala, A.; Pazos, L. M.; Credgington, D.; Hanusch, F.; Bein, T.; Snaith, H. J.; Friend, R. H. *Nature Nanotechnology* **2014**, *9*, 687–692.

[98] Xing, G.; Mathews, N.; Lim, S. S.; Yantara, N.; Liu, X.; Sabba, D.; Grätzel, M.; Mhaisalkar, S.; Sum, T. C. *Nat. Mater.* **2014**, *13*, 476–480.

[99] Sutherland, B. R.; Hoogland, S.; Adachi, M. M.; Wong, C. T. O.; Sargent, E. H. *ACS Nano* **2014**, *8*, 10947–10952.

[100] Muthu, C.; Nagamma, S. R.; Nair, V. C. *RSC Adv.* **2014**, *4*, 55908–55911.

[101] Dou, L.; Yang, Y. M.; You, J.; Hong, Z.; Chang, W.-H.; Li, G.; Yang, Y. *Nature Communications* **2014**, *5*, 5404.

[102] Luo, J.; Im, J.-H.; Mayer, M. T.; Schreier, M.; Nazeeruddin, M. K.; Park, N.-G.; Tilley, S. D.; Fan, H. J.; Gratzel, M. *Science* **2014**, *345*, 1593–1596.

[103] Amat, A.; Mosconi, E.; Ronca, E.; Quarti, C.; Umari, P.; Nazeeruddin, M. K.; Graetzel, M.; De Angelis, F. *Nano Letters* **2014**, *14*, 3608–3616.

[104] Even, J.; Pedesseau, L.; Jancu, J.-M.; Katan, C. *J. Phys. Chem. Lett.* **2013**, *4*, 2999–3005.

[105] Stroppa, A.; Barone, P.; Jain, P.; Perez-Mato, J.; Picozzi, S. *Advanced Materials* **2013**, *25*, 2284–2290.

[106] Kim, J.; Lee, S.-H.; Lee, J. H.; Hong, K.-H. *Journal of Physical Chemistry Letters* **2014**, *5*, 1312–1317.

[107] Yin, W.-J.; Shi, T.; Yan, Y. *Applied Physics Letters* **2014**, *104*, 063903.

[108] Du, M. H. *Journal of Materials Chemistry A* **2014**, *2*, 9091–9098.

[109] Yamada, Y.; Endo, M.; Wakamiya, A.; Kanemitsu, Y. *J. Phys. Chem. Lett.* **2015**, *6*, 482–486.

[110] Buin, A.; Pietsch, P.; Xu, J.; Voznyy, O.; Ip, A. H.; Comin, R.; Sargent, E. H. *Nano Lett.* **2014**, *14*, 6281–6286.

[111] Ma, J.; Wang, L.-W. *Nano Lett.* **2015**, *15*, 248–253.

[112] Frost, J. M.; Butler, K. T.; Walsh, A. *APL Mater.* **2014**, *2*, 081506.

[113] Kim, M.; Im, J.; Freeman, A. J.; Ihm, J.; Jin, H. *Proc. Natl. Acad. Sci.* **2014**, *111*, 6900–6904.

[114] Stroppa, A.; Di Sante, D.; Barone, P.; Bokdam, M.; Kresse, G.; Franchini, C.; Whangbo, M.-H.; Picozzi, S. *Nat. Commun.* **2014**, *5*, 5900.

[115] Even, J.; Pedesseau, L.; Jancu, J.-M.; Katan, C. *physica status solidi (RRL)-Rapid Research Letters* **2014**, *8*, 31–35.

[116] Menéndez-Proupin, E.; Palacios, P.; Wahnón, P.; Conesa, J. *Physical Review B* **2014**, *90*, 045207–045213.

[117] Brivio, F.; Butler, K. T.; Walsh, A.; van Schilfgaarde, M. *Physical Review B* **2014**, *89*, 155204.

[118] Zhu, X.; Su, H.; Marcus, R. A.; Michel-Beyerle, M. E. *The Journal of Physical Chemistry Letters* **2014**, *5*, 3061–3065.

[119] Kim, J.; Lee, S.-C.; Lee, S.-H.; Hong, K.-H. *The Journal of Physical Chemistry C* **2015**, *119*, 4627–4634.

[120] Kepenekian, M.; Robles, R.; Katan, C.; Sapori, D.; Pedesseau, L.; Even, J. *ACS Nano* **2015**.

[121] Krempaský, J.; Volfová, H.; Muff, S.; Pilet, N.; Landolt, G.; Radović, M.; Shi, M.; Kriegner, D.; Holý, V.; Braun, J. *et al*. *arXiv:1503.05004* **2015**.

[122] Zhong, Z.; Si, L.; Zhang, Q.; Yin, W.-G.; Yunoki, S.; Held, K. *Adv. Mater. Interfaces* **2015**, *2*, 1400445–1–1400445–5.

[123] Picozzi, S. *Front. Physics* **2014**, *2*, 1–5.

[124] Yuan, H.; Wang, X.; Lian, B.; Zhang, H.; Fang, X.; Shen, B.; Xu, G.; Xu, Y.; Zhang, S.-C.; Hwang, H. Y.; Cui, Y. *Nature Nanotech* **2014**, *9*, 851–857.

[125] Winkler, R. *Spin-orbit Coupling Effects in Two-Dimensional Electron and Hole Systems (Springer Tracts in Modern Physics)*, 2003rd ed.; Springer, 2003.

[126] Liu, S.; Srinivasan, S.; Tao, J.; Grady, M. C.; Soroush, M.; Rappe, A. M. *J. Phys. Chem. A* **2014**, *118*, 9310–9318.

[127] Motta, C.; Mellouhi, F. E.; Kais, S.; Tabet, N.; Alharbi, F.; Sanvito, S. *Nat. Commun.* **2015**, *6*, 7026.

[128] Kawai, H.; Giorgi, G.; Marini, A.; Yamashita, K. *Nano Lett.* **2015**, *15*, 3103–3108.

[129] Quarti, C.; Grancini, G.; Mosconi, E.; Bruno, P.; Ball, J. M.; Lee, M. M.; Snaith, H. J.; Petrozza, A.; Angelis, F. D. *The Journal of Physical Chemistry Letters* **2013**, *5*, 279–284.

[130] Filippetti, A.; Delugas, P.; Mattoni, A. *J. Phys. Chem. C* **2014**, *118*, 24843–24853.

[131] Bychkov, Y. A.; Rashba, E. *JETP Lett.* **1984**, *39*, 78–81.

[132] Zheng, F.; Takenaka, H.; Wang, F.; Koocher, N. Z.; Rappe, A. M. *J. Phys. Chem. Lett.* **2015**, *6*, 31–37.

[133] Kutes, Y.; Ye, L.; Zhou, Y.; Pang, S.; Huey, B. D.; Padture, N. P. *J. Phys. Chem. Lett.* **2014**, *5*, 3335–3339.

[134] Chen, B.; Shi, J.; Zheng, X.; Zhou, Y.; Zhu, K.; Priya, S. *Journal of Materials Chemistry A* **2015**, *3*, 7699–7705.

[135] Coll, M.; Gomez, A.; Mas-Marza, E.; Almora, O.; Garcia-Belmonte, G.; Campoy-Quiles, M.; Bisquert, J. *J. Phys. Chem. Lett.* **2015**, *6*, 1408–1413.

[136] Quarti, C.; Mosconi, E.; Angelis, F. D. *Chemistry of Materials* **2014**, *26*, 6557–6569.

[137] Goehry, C.; Nemnes, G. A.; Manolescu, A. *J. Phys. Chem. C* **2015**, *119*, 19674–19680.

[138] Quarti, C.; Mosconi, E.; Angelis, F. D. *Phys. Chem. Chem. Phys.* **2015**, *17*, 9394–9409.

[139] Leguy, A. M.; Frost, J. M.; McMahon, A. P.; Sakai, V. G.; Kochelmann, W.; Law, C.; Li, X.; Foglia, F.; Walsh, A.; Regan, B. C.; et al. *Nat. Commun.* **2015**, *6*, 7124.

[140] Giovanni, D.; Ma, H.; Chua, J.; Grätzel, M.; Ramesh, R.; Mhaisalkar, S.; Mathews, N.; Sum, T. C. *Nano Lett.* **2015**, *15*, 1553–1558.

[141] Hsiao, Y.-C.; Wu, T.; Li, M.; Hu, B. *Adv. Mater.* **2015**, *27*, 2899–2906.

[142] Zhang, C.; Sun, D.; Sheng, C.-X.; Zhai, Y. X.; Mielczarek, K.; Zakhidov, A.; Vardeny, Z. V. *Nature Physics* **2015**, *11*, 427–434.

[143] Das, T.; Balatsky, A. V. *Nature Communications* **2013**, *4*, 1972–1978.

[144] Perdew, J. P.; Burke, K.; Ernzerhof, M. *Phys. Rev. Lett.* **1996**, *77*, 3865–8.

[145] Bernardi, M.; Vigil-Fowler, D.; Lischner, J.; Neaton, J. B.; Louie, S. G. *Phys. Rev. Lett.* **2014**, *112*, 257402–257406.

[146] Zheng, F.; Tan, L. Z.; Liu, S.; Rappe, A. M. *Nano Letters* **2015**, *15*, 7794–7800.

[147] Egger, D. A.; Kronik, L. *The Journal of Physical Chemistry Letters* **2014**, *5*, 2728–2733.

[148] Baikie, T.; Barrow, N. S.; Fang, Y.; Keenan, P. J.; Slater, P. R.; Piltz, R. O.; Gutmann, M.; Mhaisalkar, S. G.; White, T. J. *J. Mater. Chem. A* **2015**, *3*, 9298–9307.

[149] Mattoni, A.; Filippetti, A.; Saba, M. I.; Delugas, P. *J. Phys. Chem. C* **2015**, *119*, 17421–17428.

[150] Weller, M. T.; Weber, O. J.; Henry, P. F.; Di Pumpo, A. M.; Hansen, T. C. *Chem. Commun.* **2015**, *51*, 4180–4183.

[151] Motta, C.; El-Mellouhi, F.; Sanvito, S. *Phys. Rev. B* **2016**, *93*, 235412.

[152] Yaffe, O.; et al. *arXiv:1604.08107 [cond-mat]* **2016**; arXiv: 1604.08107.

[153] Etienne, T.; Mosconi, E.; Angelis, F. D. *J. Phys. Chem. Lett.* **2016**, *7*, 1638–1645.

[154] Montero-Alejo, A. L.; Menéndez-Proupin, E.; Hidalgo-Rojas, D.; Palacios, P.; Wahnón, P.; Conesa, J. C. *J. Phys. Chem. C* **2016**, *120*, 7976–7986.

[155] Carignano, M. A.; Kachmar, A.; Hutter, J. *J. Phys. Chem. C* **2015**, *119*, 8991–8997.

[156] Uppstu, A.; Saloriutta, K.; Harju, A.; Puska, M.; Jauho, A.-P. *Phys. Rev. B* **2012**, *85*, 041401.

[157] Yuan, S.; Rösner, M.; Schulz, A.; Wehling, T. O.; Katsnelson, M. I. *Phys. Rev. Lett.* **2015**, *114*, 047403.

[158] Lehoucq, R. B.; Sorensen, D. C.; Yang, C. *ARPACK users' guide: solution of large-scale eigenvalue problems with implicitly restarted Arnoldi methods*; Siam, 1998; Vol. 6.

[159] Maschho, K. J.; Sorensen, D. C. *Applied Parallel Computing in Industrial Problems and Optimization, Lecture Notes in Computer Science* **1996**, *1184*.

[160] Voon, L. C. L. Y.; Ram-Mohan, L. R. *Phys. Rev. B* **1993**, *47*, 15500–15508.

[161] Fridkin, V. M. *Crystallog. Rep.* **2001**, *46*, 654–8.

[162] Zhang, X.-C.; Jin, Y.; Yang, K.; Schowalter, L. J. *Physical Review Letters* **1992**, *69*, 2303–2306.

[163] Bieler, M.; Pierz, K.; Siegner, U. *Phys. Rev. B* **2007**, *76*, 161304–1–4.

[164] Ogden, T. R.; Gookin, D. M. *Applied Physics Letters* **1984**, *45*, 995–997.

[165] Nakamura, M.; Kagawa, F.; Tanigaki, T.; Park, H.; Matsuda, T.; Shindo, D.; Tokura, Y.; Kawasaki, M. *Physical Review Letters* **2016**, *116*, 156801.

[166] Chynoweth, A. G. *Physical Review* **1956**, *102*, 705–714.

[167] Chen, F. S. *J. Appl. Phys.* **1969**, *40*, 3389–96.

[168] Grekov, A. A.; Malitskaya, M. A.; Spitsnya, V. D.; Fridkin, V. M. *Soviet Physics - Crystallography* **1970**, *15*, 500.

[169] Fridkin, V.; Grekov, A.; Ionov, P.; Rodin, A.; Savchenko, E.; Mikhailina, K. *Ferroelectrics* **1974**, *8*, 433–435.

[170] Glass, A. M.; von der Linde, D.; Negran, T. J. *Appl. Phys. Lett.* **1974**, *25*, 233–5.

[171] Glass, A. M.; Linde, D. v. d.; Auston, D. H.; Negran, T. J. *Journal of Electronic Materials* **1975**, *4*, 915–943.

[172] Auston, D. H.; Glass, A. M.; Ballman, A. A. *Physical Review Letters* **1972**, *28*, 897–900.

[173] Koch, W. T. H.; Munser, R.; Ruppel, W.; Wurfel, P. *Ferroelectrics* **1976**, *13*, 305–307.

[174] Dalba, G.; Soldo, Y.; Rocca, F.; Fridkin, V. M.; Sainctavit, P. *Phys. Rev. Lett.* **1995**, *74*, 988–91.

[175] Somma, C.; Reimann, K.; Flytzanis, C.; Elsaesser, T.; Woerner, M. *Physical Review Letters* **2014**, *112*, 146602.

[176] Zenkevich, A.; Matveyev, Y.; Maksimova, K.; Gaynutdinov, R.; Tolstikhina, A.; Fridkin, V. *Physical Review B* **2014**, *90*, 161409.

[177] Ichiki, M.; Furue, H.; Kobayashi, T.; Maeda, R.; Morikawa, Y.; Nakada, T.; Nonaka, K. *Appl. Phys. Lett.* **2005**, *87*, 222903–1–3.

[178] Qin, M.; Yao, K.; Liang, Y. C. *Appl. Phys. Lett.* **2008**, *93*, 122904–1–3.

[179] Pintilie, L.; Vrejoiu, I.; Le Rhun, G.; Alexe, M. *J. Appl. Phys.* **2007**, *101*, 064109–1–8.

[180] Pintilie, L.; Stancu, V.; Vasile, E.; Pintilie, I. *Journal of Applied Physics* **2010**, *107*, 114111.

[181] von Baltz, R.; Kraut, W. *Physical Review B* **1981**, *23*, 5590–5596.

[182] Král, P. *Journal of Physics: Condensed Matter* **2000**, *12*, 4851.

[183] Sipe, J. E.; Shkrebtii, A. I. *Phys. Rev. B* **2000**, *61*, 5337–52.

[184] Young, S. M.; Rappe, A. M. *Physical Review Letters* **2012**, *109*, 116601.

[185] Nastos, F.; Sipe, J. E. *Physical Review B* **2010**, *82*, 235204.

[186] Young, S. M.; Zheng, F.; Rappe, A. M. *Physical Review Letters* **2012**, *109*, 236601.

[187] Young, S. M.; Zheng, F.; Rappe, A. M. *Phys. Rev. Lett.* **2013**, *110*, 057201–057201.

[188] Brehm, J. A.; Young, S. M.; Zheng, F.; Rappe, A. M. *The Journal of Chemical Physics* **2014**, *141*, 204704.

[189] Zheng, F.; Takenaka, H.; Wang, F.; Koocher, N. Z.; Rappe, A. M. *The Journal of Physical Chemistry Letters* **2015**, *6*, 31–37.

[190] Wang, F.; Rappe, A. M. *Physical Review B* **2015**, *91*, 165124.

[191] Tan, L. Z.; Rappe, A. M. *Physical Review Letters* **2016**, *116*, 237402.

[192] Wang, F.; Young, S. M.; Zheng, F.; Grinberg, I.; Rappe, A. M. *Nature Communications* **2016**, *in press*.

[193] Dualeh, A.; Moehl, T.; Tétreault, N.; Teuscher, J.; Gao, P.; Nazeeruddin, M. K.; Grätzel, M. *ACS nano* **2013**, *8*, 362–373.

[194] Jeon, N. J.; Noh, J. H.; Kim, Y. C.; Yang, W. S.; Ryu, S.; Seok, S. I. *Nature materials* **2014**.

[195] Brivio, F.; Walker, A. B.; Walsh, A. *APL Materials* **2013**, *1*, 042111.

[196] Wang, Y.; Gould, T.; Dobson, J. F.; Zhang, H.; Yang, H.; Yao, X.; Zhao, H. *Physical chemistry chemical physics : PCCP* **2014**, *16*, 1424–9.

[197] Mosconi, E.; Amat, A.; Nazeeruddin, M. K.; Graetzel, M.; De Angelis, F. *Journal of Physical Chemistry C* **2013**, *117*, 13902–13913.

[198] The dipole moment of molecule CH3NH3$^+$ is calculated as 2.2 Debye with HF/6-311G(p,d) using GAMESS.

[199] Dykstra, C.; Frenking, G.; Kim, K.; Scuseria, G. *Theory and applications of computational chemistry: the first forty years*; Elsevier, 2011.

[200] Lee, M. M.; Teuscher, J.; Miyasaka, T.; Murakami, T. N.; Snaith, H. J. *Science* **2012**, *338*, 643–647.

[201] Colella, S.; Mosconi, E.; Pellegrino, G.; Alberti, A.; Guerra, V. L.; Masi, S.; Listorti, A.; Rizzo, A.; Condorelli, G. G.; De Angelis, F.; Gigli, G. *The Journal of Physical Chemistry Letters* **0**, *0*, null.

[202] Young, S. M.; Zheng, F.; Rappe, A. M. *Phys. Rev. Lett.* **2012**, *109*, 236601.

[203] Neaton, J. B.; Ederer, C.; Waghmare, U. V.; Spaldin, N. A.; Rabe, K. M. *Physical Review B* **2005**, *71*, 014113.

[204] Young, S. M.; Rappe, A. M. *In preparation* **2015**.